EPFL

How are cells instructed to form somite boundaries by the zebrafish segmentation clock?

Olivier François VENZIN

2023

Acknowledgements

Abstract

In vertebrate embryos, the elongating body axis is patterned via the sequential and rhythmic production of segments from a posterior unsegmented tissue called the presomitic mesoderm (PSM). This process is controlled by a population of cellular oscillators termed the segmentation clock.

Cellular oscillators are locally coupled by Notch signaling and they generate spatiotemporal waves of gene expression that sweep the tissue from posterior to anterior, reiterating during the formation of each segment. These anteriorly-moving waves are thought to interact with a wavefront, regressing posteriorly through the PSM, that records the cellular oscillations as it passes. This interaction transforms a temporally periodic signal into a permanent spatially periodic pattern, which prefigures the location of future somite boundaries. The molecular details of how this interaction occurs remain elusive.

In this work, using the zebrafish as a model, I first studied how the clock's wave pattern and the wavefront interact during the formation of the anterior-most somite boundaries. Using lightsheet microscopy, I imaged the first onset of the segmentation clock using a transgene reporting *her1* expression, and another transgene reporting on the dynamics of the wavefront gene *tbx6*.

I found that Tbx6, oscillates in individual cells and travels as waves of gene expression in the PSM during early somitogenesis. Our results suggest that the *her1* wave pattern is required for the generation of Tbx6 waves. Two waves of Tbx6 expression were found to arrest at positions that prefigure the locations of the anterior boundaries of the first and the second somite of the embryo, respectively.

I then addressed the question of what level of synchrony in the wave pattern is required for the formation of correct somite boundaries. In zebrafish Notch pathway mutants, a small number of segments are properly formed in the anterior, followed by defective segments in the posterior. This phenotype can be explained by the fact that, in absence of Notch signaling, neighboring noisy oscillators slowly drift out of phase, ultimately resulting in the disruption of the wave pattern and consequently the formation of defective segments. Defects in somite boundaries are thought to result in malformations of the spine, a condition termed congenital scoliosis in the clinic. Drugs blocking Notch signaling can desynchronize the segmentation clock, mimicking Notch mutants. Upon drug washout, the segmentation clock can gradually resynchronize and, once the wave pattern is restored, normal segments form again.

We imaged the resynchronization of the segmentation clock in live embryos. We observed that defects in somite boundaries were often spatially restricted to a specific part of the

boundary, e.g. dorsal versus ventral. By back-tracking cells from defective boundaries and looking at their Her1 oscillatory traces, we found that the level of synchrony between a cell and its neighbors was spatially heterogeneous in the PSM: cells forming the correct part of a defective somite boundary had a higher level of synchrony with their neighbors than cells forming the defective part of the boundary. This result provides a qualitative explanation for the formation of local defects in somite boundaries. Taken together, these results helped to gain a better understanding of how cells are instructed to become part of a somite boundary by the zebrafish segmentation clock.

Keywords: "developmental biology", "segmentation clock", "zebrafish", "biological oscillaots", "synchronization", "pattern formation", "Notch signaling"

Résumé

Chez les embryons de vertébrés, l'axe du corps qui s'allonge est modelé par la production séquentielle et rythmique de segments à partir d'un tissu postérieur non segmenté appelé mésoderme présomitique (PSM). Ce processus est contrôlé par une population d'oscillateurs cellulaires appelée l'horloge de segmentation.

Les oscillateurs cellulaires sont couplés localement par la voie de signalisation Notch et ils génèrent des vagues d'expression de gènes qui balaient le tissu de postérieur en antérieur, se répétant pendant la formation de chaque segment. On pense que ces vagues se déplaçant interagissent avec un front d'onde, régressant en direction du PSM postérieur, qui enregistre les oscillations cellulaires à son passage. Cette interaction transforme un signal périodique temporel en un motif permanent spatialement périodique, qui préfigure l'emplacement des futures frontières des somites. Les détails moléculaires de la façon dont cette interaction se produit restent peu clairs.

Dans ce travail, en utilisant le poisson zèbre comme modèle, j'ai d'abord étudié comment le vagues d'expression de gènes et le front interagissent pendant la formation des frontières des somites antérieures. J'ai imagé l'initiation de l'horloge de segmentation en utilisant un transgène rapportant l'expression de *her1*, et un autre transgène rapportant la dynamique du gène *tbx6*, impliqué dans le front d'onde.

J'ai constaté que Tbx6 oscillait dans des cellules individuelles et se déplaçait sous forme de vagues d'expression de gènes dans le PSM au début de la somitogenèse. Nos résultats suggèrent que les gènes de l'horloge de la segmentation *her1* et *her7* sont nécessaires pour la génération des vagues de Tbx6. On a constaté que deux vagues d'expression de Tbx6 s'arrêtaient à des positions qui préfigurent les emplacements des frontières antérieures du premier et du deuxième somite de l'embryon, respectivement.

J'ai ensuite cherché à savoir quel niveau de synchronisation au sein des oscillateurs cellulaires est nécessaire pour la bonne formation des frontières des somites. Chez les mutants de la voie Notch, un petit nombre de segments sont correctement formés dans la partie antérieure, suivis de segments défectueux dans la partie postérieure. Ce phénotype peut être expliqué par le fait qu'en l'absence de la signalisation Notch, les oscillateurs voisins se déphasent lentement, ce qui entraîne finalement la perturbation des vagues d'expression de gènes et par conséquent la formation de segments défectueux. On pense que les défauts dans les frontières des somites entraînent des malformations de la colonne vertébrale, une condition appelée scoliose congénitale en clinique. Des composés chimiques bloquant la signalisation Notch peuvent désynchroniser l'horloge de la segmentation, imitant les mutants Notch. Après l'élimination desdits composés chimiques, l'horloge de segmentation peut progressivement se resynchroniser et, une fois le les vagues d'expression revenue, des segments normaux se forment à nouveau.

Nous avons imagé la resynchronisation de l'horloge de segmentation dans des embryons vivants. Nous avons observé que les défauts des frontières des somites étaient souvent limités spatialement à une partie spécifique de la frontière, par exemple uniquement dorsale ou ventrale. En suivant à rebours les cellules formant les frontières défectueuses et en examinant leurs oscillations d'Her1, nous avons constaté que le niveau de synchronisation entre une cellule et ses voisines était spatialement hétérogène dans le PSM : les cellules formant la partie correcte d'une frontière de somite défectueuse avaient un niveau de synchronisation avec leurs voisines plus élevé que les cellules formant la partie défectueuse de la frontière. Ce résultat fournit une explication qualitative de la formation de défauts locaux dans les limites des somites. Dans l'ensemble, ces résultats ont permis de mieux comprendre comment les cellules sont instruites pour devenir une partie de la frontières d'un somite par l'horloge de la segmentation du poisson zèbre.

Mots-clés "biologie du développement", "somitogénèse", "horloge de la segmentation", "poisson-zèbre", "oscillateurs biologiques", "synchronization", "Voie de signalization Notch"

Contents

Table of Contents

x

Chapter 1   Introduction[1]

One of the major events of vertebrate development is the segmentation of the body axis into somites, during a morphological patterning process called somitogenesis. The resulting somites are transient blocks of epithelial cells that ultimately give rise to the segmented vertebrae, ribs, skeletal muscle and skin of the adult body. The number and relative size of vertebrae in an organism are defined during somitogenesis. Malfunction of this patterning process results in malformations of these structures, a condition termed congenital scoliosis in the clinic (Bulman et al., 2000; Sparrow et al., 2010, 2008, 2006).

Somitogenesis takes place in an unsegmented tissue, called presomitic mesoderm (PSM), located in the posterior end of the embryo (Fig. 1). Bilateral pairs of somites bud off sequentially and rhythmically from the PSM (labelled S0 in Fig. 1) by the formation of new somite boundaries separating them from the PSM (labelled B0 in Fig. 1). The formation of a new somite boundary is thought to consist of three steps (Dahmann et al., 2011; Yabe and Takada, 2016). First, the boundary of the new prospective somite is established at the determination front. Secondly, cells located at the interface of this stripe undergo a mesenchymal-to-epithelial transition (MET) resulting in the epithelialization of cells on both sides of the boundary. Simultaneously, a rostro-caudal polarity of the presumptive somite, important for subsequent myotome and sclerotome development, is established. Finally, extracellular matrix is deposited between somite boundaries, forming the somitic furrow. The present work focuses on the first of these steps, the positioning of the presumptive somite boundary. More precisely, I address the general question of how cells are instructed to form a somite boundary by the segmentation clock.

Somite formation takes place every 30 minutes in zebrafish (at 28°C), 2 hours in mice and 5-6 hours in humans (Gomez 2008). The rhythmicity of somitogenesis hints at the presence of a clock at work in this process. To explain the high degree of consistency for the number of somites in individuals of different sizes in a given species, Cooke and Zeeman proposed a "Clock and Wavefront" model in 1976 (Figure 2A). This model consists of two components: an oscillatory mechanism, i.e. the Clock, that interacts with a Wavefront of sudden cellular change (Cooke and Zeeman, 1976). The wavefront slowly regresses posteriorly through the PSM and records or registers the cellular oscillations as it passes, thereby transforming a temporally periodic signal into a permanent spatially periodic pattern. As this spatial pattern prefigures the position of a future segment boundary, it is termed a pre-pattern. According to the model, the size of somites is defined as the product of the velocity of the wavefront and the period of the clock. The total number of somites is determined by the duration of somitogenesis divided by the period of the clock. Over the years, the "Clock

---

[1] The material in this chapter has been adapted from (Venzin and Oates, 2020) according to the publisher's policy on authors' rights and from a manuscript co-written with Cristina Loureiro Casalderey and Andrew Oates.

and Wavefront" model has obtained extensive experimental support, making it a favorite conceptual model for somitogenesis.
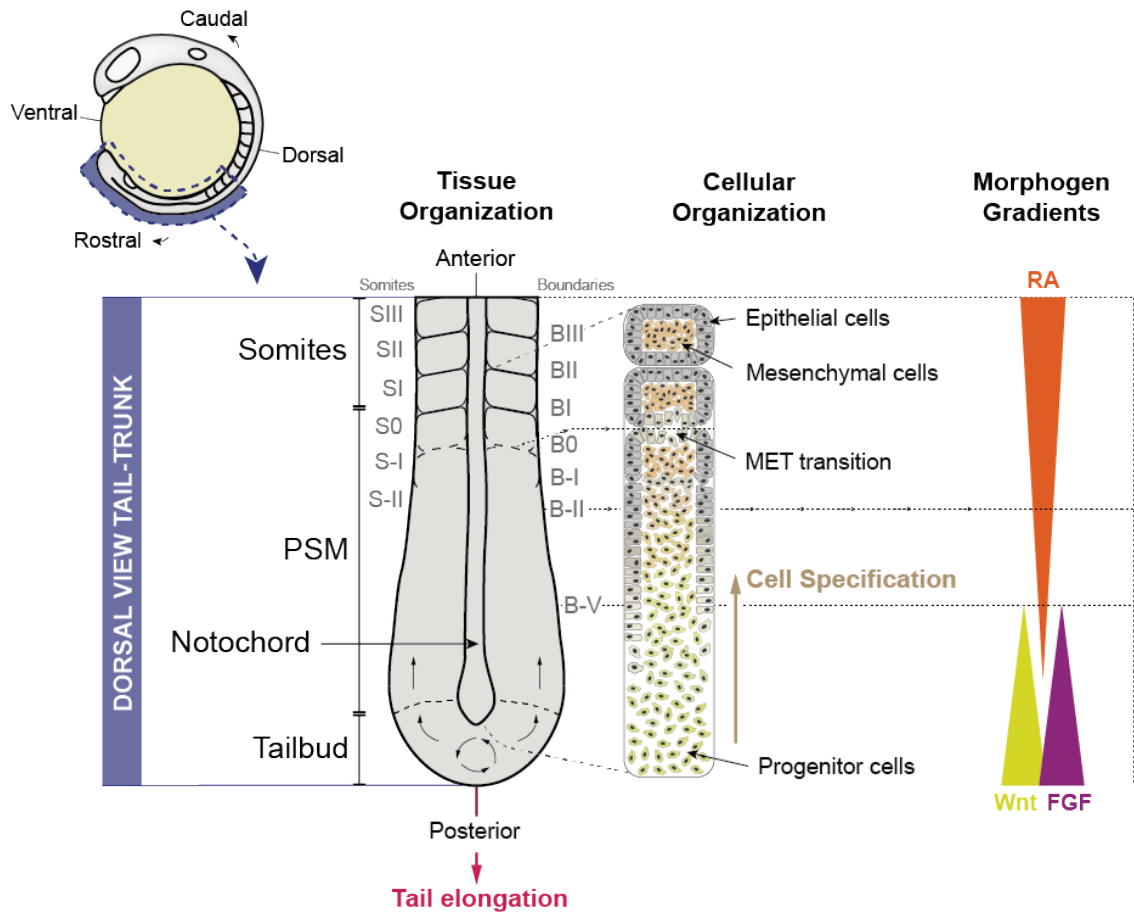
Figure 1: **Schematic representation of the somitogenesis.** Dorsal view of a zebrafish embryo with formed somites (SI, SII and SIII), a currently forming somite (S0) and the prospective somites (S-I and S-II) that are yet to epithelialize via a mesenchymal-to-epithelial transition (MET). As they undergo epithelialization, somites bud from an unsegmented tissue called the presomitic mesoderm (PSM). This is a rhythmic and sequential process that repeats for the formation of every new somite pair. As the embryo elongates, cells are advected through the reference frame of the tissue from the tailbud to the anterior end of the PSM. Cells gradually mature during the advection. The boundary of the new prospective somite is established at the determination front. The exact location of the determination front in the PSM is still debated. This position is thought to be influenced by a set of morphogen gradients.
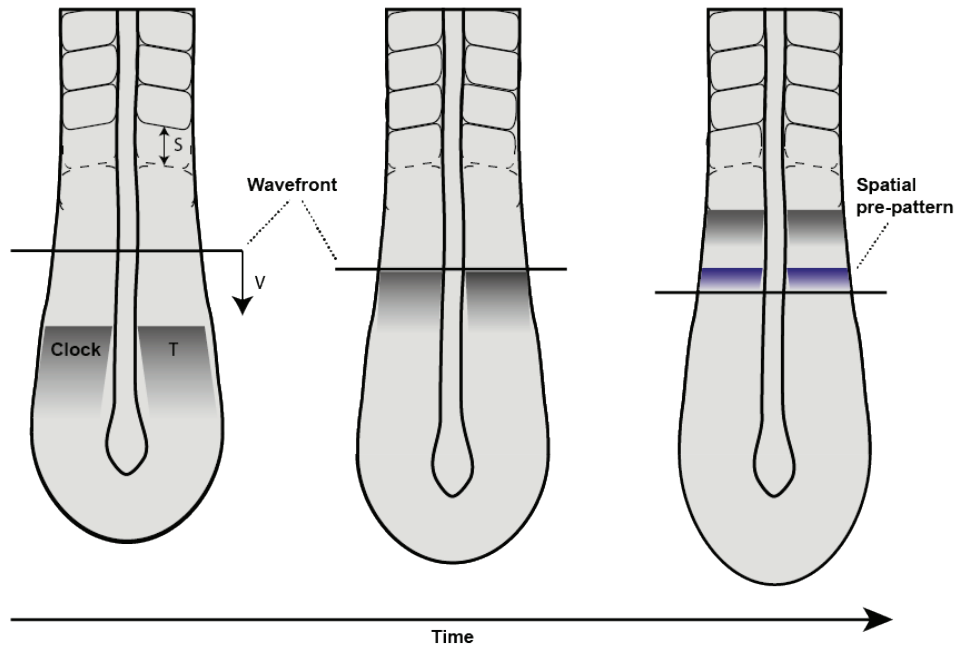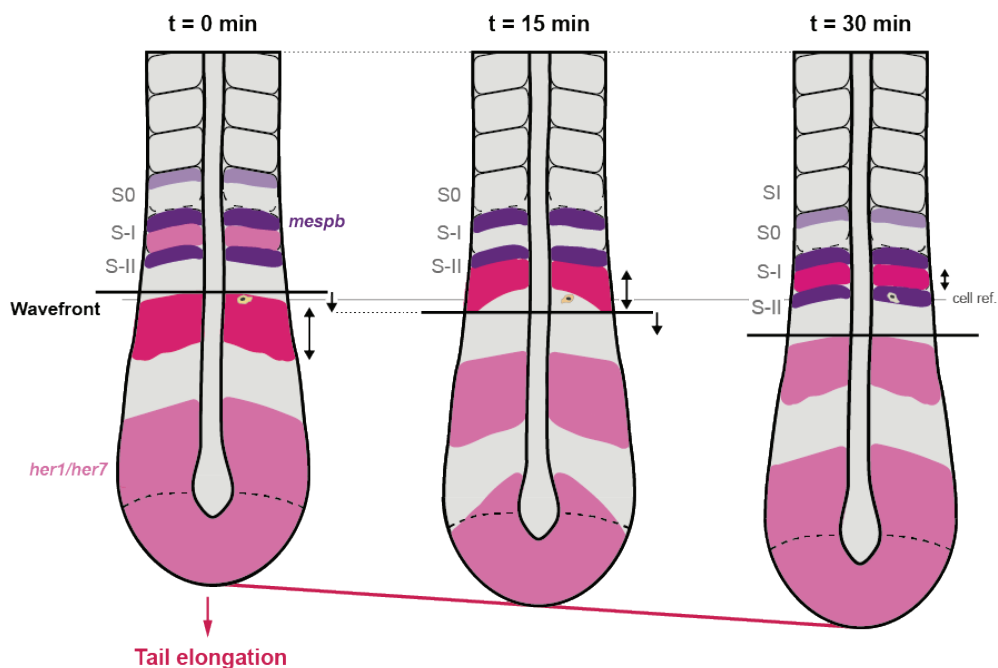
Figure 2: Schematic representation of the clock and wavefront model and the molecular segmentation clock. A) In the Clock and Wavefront model, an oscillatory mechanism, i.e. the Clock, interacts with a regressing Wavefront of cellular change. Here the clock is illustrated as a periodic wave that sweeps through the PSM with period *T.* The Wavefront regresses posteriorly through the PSM in the lab reference frame with velocity *v* and records or otherwise responds to oscillations in cells, which then undergo rapid changes of properties according to the phase of their oscillations. For simplicity the wavefront is represented as a line, i.e. it acts instantaneously. This mechanism translates a temporally periodic signal into a spatially periodic pattern of cell states (blue). As this spatial pattern prefigures the position of a future segment boundary, it is termed a pre-pattern. Regardless of the details, a clock and wavefront mechanism results in segments of length S determined by the period of the clock T and the velocity of the wavefront v as S = vT. B) A molecular segmentation clock underlies the rhythmicity of somitogenesis. The segmentation clock is a network of coupled genetic oscillators. It manifests as kinematic waves of gene expression traveling anteriorly along the PSM (*her1/her7* expression in pink). Concomitantly, a determination wavefront regresses posteriorly from the anterior PSM, recording the cellular oscillations. This process translates a spatiotemporal signal, the her1/her7 molecular clock, into a permanent spatially periodic pattern (*mesp-b* pattern in purple). This spatial prepattern prefigures the position of the new somite boundaries, thereby permanently fixing the periodic spatial pattern.

A genetic oscillator involved in somitogenesis was first discovered in the chick PSM 25 years ago (Palmeirim et al., 1997). Since then, molecular clocks have been observed in mice, frogs, zebrafish, and more recently in human iPS cells (Masamizu et al., 2006; Delaune et al., 2012; Krol et al., 2011; Matsuda et al., 2019; Diaz-Cuadrados et al., 2018). This genetic oscillator manifests itself at the tissue level as waves of gene expression traveling from the posterior to the anterior PSM, and arresting at a location that prefigures the boundary of a new somite (Figure 2B) (Palmeirim et al., 1997). At the cellular level, a transcription-translation negative feedback loop involving genes of the Hes/Her family is proposed to generate cell-autonomous oscillations in gene expression (Figure 3A) (Rohde et al., 2021; Webb et al., 2016; Masamizu et al., 2006). These cellular oscillations are locally synchronized via cell-to-cell communication mediated by Notch signaling (Figure 3B) (Horikawa et al., 2006; Jiang et al., 2000; Riedel-Kruse et al., 2007; Tsiairis and Aulehla, 2016). The oscillations also gradually slow as the cells move along the PSM, giving rise to kinematic waves that travel anteriorly along the PSM (Jiang et al., 2000; Oates and Ho, 2002; Soroldoni et al., 2014; Tsiairis and Aulehla, 2016, Falk 2022). The wave pattern provides timing information in the system and represents the molecular counterpart of the "Clock".

Classically, the "Wavefront" is thought to consist of a set of morphogen gradients providing positional information to the cells in the PSM and a set of genes turning the spatial signal from the "Clock" into a spatial pattern. The morphogen gradients spanning the PSM, including FGF (Dubrulle 2001, Akiyama et al., 2014; Sawada, 2001), Wnt (Aulehla 2008, Dunty 2008, Bajard et al., 2014) and Retinoic acid (Moreno et al., 2008; Vermot and Pourquié, 2005) (Figure 1). *Tbx6*, *Ripply* and, depending on the species, *Mesp* are thought to interact with the "Clock" to define the position of presumptive boundaries (Kawamura et al., 2008, 2005; Nikaido et al., 2002; Oginuma et al., 2008; Saga et al., 1997; Sawada et al., 2000; Takahashi et al., 2010, 2000). In addition to its role in determining the position of presumptive boundaries, the "Wavefront" is also thought to arrest the oscillations in the anterior PSM (Kawamura et al., 2005).

The basic processes of the Segmentation Clock appear to be conserved among vertebrates, however, genetic and molecular details vary between species (Krol et al., 2011). For example, some components of the Fgf and Wnt signaling pathways oscillate in mice and chick, but not in zebrafish. Another example is the interaction between the Clock and the Wavefront that seems to be mediated by *Mesp2* in mice but independent of *mesp* in zebrafish. In an attempt to be as exhaustive as possible in one system, this introduction will focus on the zebrafish segmentation clock. When deemed relevant, I include results from the mouse segmentation clock. For a comparison of the molecular mechanisms of the segmentation clock between zebrafish and mice, see the excellent review from Yabe and Takada (Yabe and Takada, 2016).

In zebrafish, the genetic and molecular basis of the Clock and the Wavefront are relatively well-understood in isolation. However, it is unknown where or how the Clock and the Wavefront molecularly interact to establish the spatial pre-pattern. This knowledge gap prevents a mechanistic understanding of the zebrafish segmentation clock as a patterning process. In this introduction, I first describe the molecular and genetic basis of the Clock and the Wavefront before turning to some lines of evidence hinting at their potential interactions for establishing the position of presumptive somite boundaries.

1.1   The « Clock »
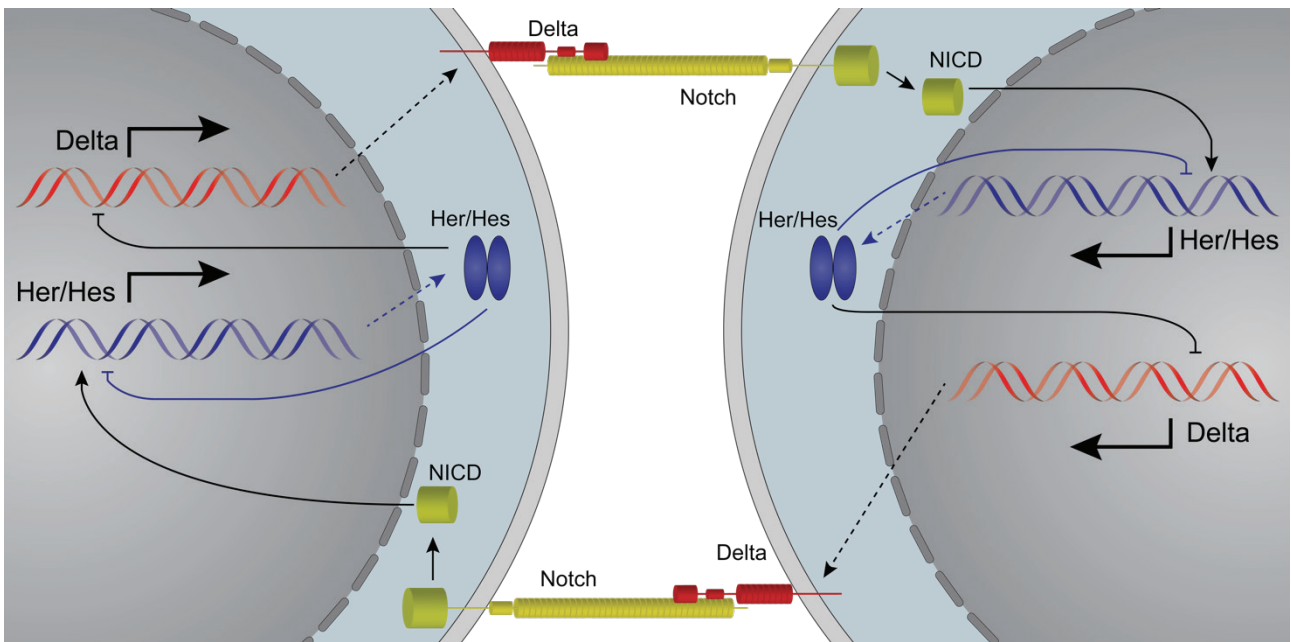
Figure 3: **Schematic of Notch-mediated coupling between two adjacent PSM cells.** Oscillations in clock gene expression are synchronized between neighboring cells via Notch signalling. The negative feedback loop of Her/Hes genes, depicted in blue, is theoretically sufficient to generate oscillations in Her/Hes gene expression. In addition to repressing their own expression, Her/Hes proteins also inhibit the expression of Delta ligands. DeltaC in zebrafish and Dll1 in mouse are cyclically expressed in PSM cells. Delta ligands are thought to provide information about the phase of a given PSM cell to its neighbors by binding Notch receptors in adjacent cells. The binding of a Delta ligands, located at the signal-sending cell membrane, with a Notch receptor results in the release and the translocation of the NICD into the nucleus of the signal-receiving where the NICD induces the expression of Her/Hes genes. In this way, the oscillation of Her/Hes gene in the signal-receiving cell is influenced by the phase of its neighbors.

The cell-autonomous core oscillator is composed of two negative feedback loops involving bHLH transcription factors from the Hes/Her gene family (Figure 3A). Her1 homodimers and Her7:Hes6 heterodimers bind to the shared *her1-her7* promoter region and repress their own expression (Gajewski, 2003; Henry, 2002; Oates and Ho, 2002; Schröter et al., 2012; Lewis 2003, Trofka 2012). The auto-inhibitory feedback loop, with delays in transcription and translation, has been mathematically shown to be sufficient to generate oscillations in gene expression (Lewis, 2003; Monk, 2003), and in culture, isolated zebrafish PSM cells show noisy, persistent oscillations (Webb et al., 2016). In the embryo, cell-autonomous oscillations are coupled by cell-cell interactions via Notch signaling (Horikawa et al., 2006; Jiang et al., 2000; Oates and Ho, 2002; Riedel-Kruse et al., 2007; Delaune et al., 2012).

Synchronization between adjacent PSM cells is thought to rely on the transcriptional activation of Notch target genes, including the clock genes *her1* and *her7* (Figure 3B)(Brend and Holley, 2009; Lewis, 2003; Oates and Ho, 2002; Takke and Campos-Ortega, 1999, Sieger 2003). Her1 and Her7 are also thought to repress, in addition to their own expression, the transcription of *deltaC*, which results in its cyclic expression (Takke and Campos-Ortega 1999, Oates and Ho, 2002, Lewis, 2003). Excellent reviews have covered the mechanisms of Notch signaling (Bray 2016, Kovall 2017). Briefly, when a Delta ligand binds to a Notch receptor, it triggers a cascade of cleavages (Bray, 2016). The last cleavage, performed by the γ-secretase complex, releases the Notch Intracellular Domain (NICD) in the signal-receiving cell. The NICD translocates to the nucleus where it interacts with the co-

activator Mastermind (MAM) and the DNA-binding protein Suppressor of Hairless (SuH, also called CSL or RBP-κj in mammals) to activate target genes (Echeverri and Oates, 2007; Sieger et al., 2003). The her1/her7 promoter region contains SuH binding sites, suggesting that the NICD stimulates Hes/Her gene expression (Brend and Holley, 2009; Lewis, 2003; Oates and Ho, 2002; Takke and Campos-Ortega, 1999, Sieger 2003). The activity of the NICD has not been recorded in zebrafish, but it was reported to show a characteristic wave pattern in the mouse PSM (Huppert et al., 2005). This mechanism would allow a PSM cell to send information about its phase in the Hes/Her oscillation cycle to its neighbors, where modulation of Notch activity can potentially speed up or slow down the transcription of Hes/Her genes to gradually bring neighboring cells into synchronous cycles of gene expression (Lewis, 2003).

Two Delta ligands, *deltaC* and *deltaD*, are expressed in the PSM (Holley et al., 2000; Jülich et al., 2005). They are both required for synchronizing the molecular clocks, but appear to behave quite differently in the PSM (Van Eeden et al., 1996; Jiang et al., 2000; Wright et al., 2011; Keskin et al., 2018; Delaune et al., 2012; Mara et al., 2007). First, their respective mutants show different morphological phenotypes (Van Eeden et al., 1996, Jiang et al., 2000). Second, *deltaC* is expressed as traveling waves in the PSM, similarly to *her1* and *her7* (Jiang et al., 2000; Jülich et al., 2005), while the expression of *deltaD* does not oscillate (Holley, 2002). Two Notch receptors, *notch1a* and *notch2* (previously *notch6*), are expressed in the zebrafish PSM, but only *notch1a* mutants show a segmentation phenotype (van Eeden et al., 1996). In summary, the zebrafish 'Clock' consists molecularly in cell-autonomous Her1/Her7 oscillations that are locally coupled by two delta ligands, DeltaC and DeltaD, and the Notch1a receptor.

In principle, a wave pattern in the tissue must result from a phase difference in the population of oscillators along the PSM. To explain the arrest of the wave pattern and the shortening of its wavelength in the anterior PSM, it has been suggested that the phase shift arises from cellular oscillators slowing down as they move anteriorly, before they arrest in the anterior PSM (Giudicelli et al., 2007; Gomez et al., 2008; Morelli et al., 2009; Oates et al., 2012; Palmeirim et al., 1997). The slowing and arrest of cellular oscillations has more recently been observed directly by time-lapse imaging (Shih et al., 2015; Rohde et a., 2021). This frequency profile is proposed to be regulated by morphogen gradients of Fgf, Wnt and Retinoic Acid (Oates et al., 2012), but direct evidence of how such a gradient would cause slowing of the oscillators is lacking.

The dynamics of oscillators that are both slowing down and attempting to locally synchronize as they move in space presents challenges to intuition. A theoretical framework named the "delayed coupling theory" modeled the combined effect of a frequency profile along the PSM and coupling between neighboring oscillators with a time delay in the information transfer (Morelli et al., 2009). In this picture, cells are abstracted as phase oscillators and their oscillations arrest when they meet a wavefront moving posteriorly in the PSM. The collective frequency of oscillations defines the rate of somite formation. In the absence of coupling delay, the collective frequency is equal to the intrinsic frequency in the posterior

PSM. Surprisingly, the authors found that a short coupling delay would slow down the collective frequency compared to the intrinsic frequency, while a long coupling delay would speed it up with respect to the intrinsic frequency. The authors predicted that the collective frequency is a function, not only of the intrinsic frequency in the posterior PSM but also of the coupling strength and the coupling delay. The impact of the coupling strength on the collective frequency was experimentally confirmed by the observation that the clock's period was increased by reduced coupling in several Delta-Notch mutants or in embryos treated with the Notch signaling inhibitor DAPT (Herrgen et al., 2010). These embryos developed somites that were longer along the AP axis than normal. In contrast, in transgenic embryos with increased *deltaD* copy number, segmentation happens faster, producing more but shorter somites (Liao et al., 2016). This experimentally confirms one of the key predictions from the "Clock and Wavefront" model, namely that somite size is controlled by the clock's period (Cooke and Zeeman, 1976). Despite the success of this phase description, the slowing and arrest of oscillators are described in phenomenological terms and does not give any insight into the mechanism or molecular nature of the wavefront.

1.2   The wavefront

Here, I review separately two characteristics classically attributed to the Wavefront : the rapid cellular changes triggered by a set of genes that I define as the core of the Wavefront and the positioning of the Wavefront by the morphogen gradients. I start by providing an overview of the former and I briefly discuss the later in section 1.3.

During the genetic screen for mutations affecting embryogenesis in zebrafish, a mutant was found to develop with a complete absence of somite boundaries, and was hence named fused somites (fss) (van Eeden et al., 1996). Soon after, the gene associated with the mutation was identified as the T-box transcription factor *tbx6* (formerly *tbx24*) (Nikaido et al., 2002). A few years later, it was shown that knocking down the Groucho-associated transcription factor *ripply1*, also resulted in the complete loss of somite boundaries (Kawamura et al., 2005). Despite these dramatic phenotypes, characteristic wave patterns of the cyclic genes are still present in the PSM of embryos. The fact that these two genes are not part of the "Clock", but are still required for somite boundary formation, implies their involvement in converting the oscillations into a permanent periodic pattern and suggests that their activities are at the core of the molecular wavefront (Fig. 4A). In contrast, transient inhibition of Fgf (Sawada, 2001; Wanglar et al., 2014) or Wnt (Bajard et al., 2014) signaling result in longer somites but somite formation is not impaired, suggesting that, at least in zebrafish, the morphogen gradients are likely to be involved in positioning the wavefront rather than being part of the wavefront themselves. I discuss the evidence for such a role in section 1.3.

Tbx6 and Ripply1 appear to behave quite differently in the PSM. The expression of *tbx6* spans the entire PSM (Nikaido et al., 2002; Wanglar et al., 2014), while *ripply1* is expressed as several stripes in the rostral part of already formed somites, in S0 and in S-I (Figure 4B)

(Kawamura et al., 2005). In contrast to cyclic genes of the segmentation clock, neither gene is thought to oscillate. In *fss*, the anterior stripe of *her1* expression is lost (Sawada et al., 2000). In fact, a specific region of the *her1* promoter, required for the *her1* anterior stripe expression, was found to contain a T-box binding site for Tbx6 proteins (Brend and Holley, 2009). This suggests that Tbx6 activates *her1* expression, at least in the anterior PSM. In contrast, the expression of *her1* and many other genes expressed in the PSM is not properly terminated, and therefore rostrally extended, in embryos injected with *ripply1* morpholinos (MO) (Kawamura et al., 2005). Together, these results indicate that, molecularly, the wavefront is not only reading the phase of the clock but is also involved in its regulation.

Several genes mark the stable period pattern in the anterior PSM, downstream of the clock and wavefront. In zebrafish, four genes of the Mesp family of bHLH transcription factors are expressed in the PSM, i.e. *mesp-aa, mesp-ab, mesp-ba* and *mesp-bb* (Durbin et al., 1998, Lindsey et al., 2000; Sawada et al., 2000; Cutty et al., 2012). The latest discovered *mesp-ab* and *mesp-bb* genes were found to display almost identical expression patterns to *mesp-aa* and *mesp-ba*, respectively (Cutty et al., 2012). Therefore, and for the sake of simplicity, we refer to *mesp-aa* and *mesp-ab* as « *mesp-a* paralogs » and to *mesp-ba* and *mesp-bb* as « *mesp-b* paralogs ». All four *mesp* genes display a stripe pattern in the anterior PSM (Durbin, Lindsey et al., 2000; Sawada et al., 2000; Cutty et al., 2012). The *mesp-a* paralogs are expressed in two stripes located in the rostral part of the presumptive somites S-I and S-II (Figure 4B). The *mesp-b* paralogs display a similar expression pattern but also show a faint stripe in the rostral part of S0. The *protocadherin8* (*papc*) gene exhibits a similar expression pattern to *mesp-b* paralogs, with an additional stripe in the rostral part of SI (Sawada et al., 2000). The posterior-most stripe of *papc* and the four *mesp* genes mark the presumptive boundary between S-I and S-II. This spatial pre-pattern can be thought of as the readout of the interaction of the clock and the wavefront.
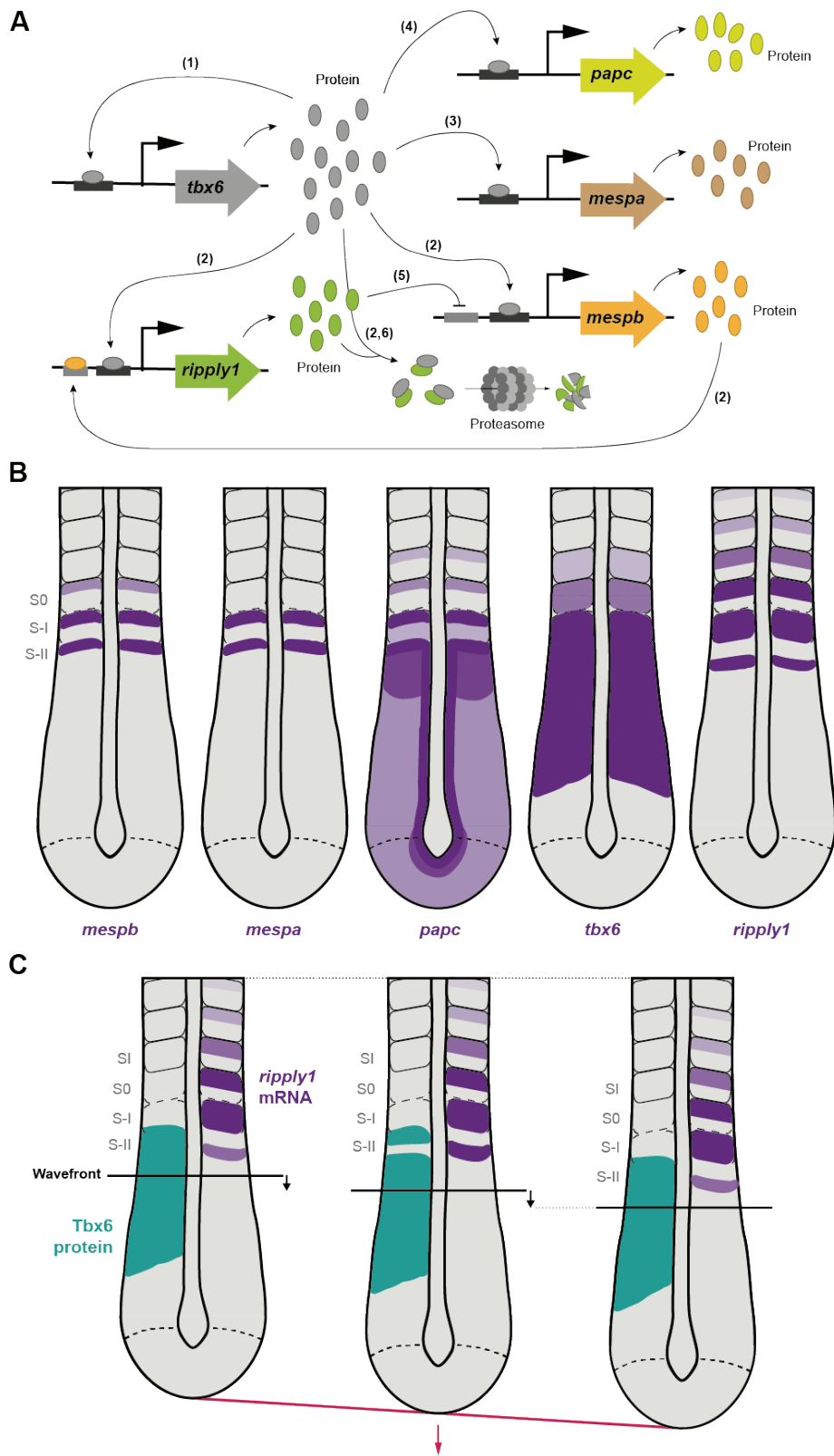
Figure 4: **Gene regulatory network model of the molecular clock in zebrafish**. A) Autoinhibitory feedback loop of *her1/her7 transcription and translation*. Her1 homodimers and Her7:Hes6 heterodimers bind to the *her1/her7* shared promoter region and rhythmically repress the expression of *her1* and *her7*. The other dimers form, but are weak DNA-binders and remain in a "cloud". The hes6 gene is not rhythmically transcribed, but hes6 mRNA and Hes6 protein form a gradient across the PSM, highest in the posterior. B) Delta-Notch signaling couples the cell-autonomous oscillations between adjacent cells. When a Delta ligand binds to a Notch receptor, it triggers a cascade of cleavages that induces the release of the Notch Intracellular Domain (NICD) in the signal-receiving cell. The NICD translocates to the nucleus where it interacts with Suppressor of Hairless (SuH) to activate target genes, including *her1* and *her7*. As Her1 and Her7 cyclically repress *deltaC* expression, the subsequent activation of Notch by DeltaC is also thought to be cyclic and to be in phase with the sending cell's oscillations. Therefore, this mechanism allows the sending cell to communicate information about its phase to the receiver cell, leading to the local synchronization of the cells. Note that in this model, the communication is bi-directional and a cell can be both sending and receiving the Notch signal.

In quadruple *mesp* homozygous mutants (m4), although boundaries of the first few anterior somites appear to be absent, somite boundary formation still occurs for most of the somites (Yabe et al., 2016). This is in contrast with the phenotypes of *fss* and *ripply1*-MO-injected embryos where no somites form, indicating that the four *mesp* genes are not strictly required for somite formation. However, in posterior somites, the morphology of boundaries appeared partially disrupted in quadruple *mesp* mutants (Yabe et al., 2016). This suggests that the epithelialization of somite boundaries does not occur properly. The striped expression pattern of *eph4a*, a component of Eph-ephrin signaling reported to be required for proper segmentation (Durbin et al., 1998), is abolished in m4. However, the striped expression of *papc*, shown to be involved in the epithelialization of somite boundaries in mice (Rhee 2003), is not affected in m4. This suggests that two partially redundant pathways might be involved in somite epithelialization: One Mesp-dependent pathway through Eph-ephrin signaling and one Mesp-independent pathway, potentially through Papc and cadherins.

In addition, Mesp also appears to play a role in rostrocaudal (RC) compartmentalization (Windner et al., 2015; Yabe et al., 2016). Indeed, RC compartmentalization was impaired in embryos injected with morpholinos against both *mesp-b* paralogs (Windner et al., 2015). Thereafter, *mesp* genes were found to be necessary and sufficient for induction of the rostral polarity in somites (Yabe et al., 2016). Taken together, these results indicate that *mesp* cannot be thought of as a key component of the wavefront as it is not strictly required for the positioning of presumptive boundaries. Mesp rather seems to play a role in downstream processes such as epithelialization of somite boundaries and rostrocaudal compartmentalization of somites. *Mesp* genes act as a readout of the spatial pre-pattern in the zebrafish segmentation clock, which contrasts with the mouse segmentation clock where *Mesp2* is thought to be actively involved in positioning presumptive somite boundaries (Saga 2012a).

In *fss*, the expression of the four *mesp* genes and *papc* in the PSM is either undetectable or greatly reduced without any noticeable stripe (Cutty et al., 2012; Oates et al., 2005; Sawada et al., 2000). T-box binding sites, along with *SuH* binding sites, were found in all *mesp* promoters, suggesting a direct activation of *mesp* by Tbx6 (Figure 4A) (Cutty et al., 2012). As in *mesp* quadruple mutants, *eph4a* is expressed in *fss* but its stripe pattern is lost (Durbin et al., 2000). Ectopic expression of *eph4a* in *fss* rescued the formation of somite boundaries, although it is not clear whether their morphology was impaired (Durbin et al., 2000). Combined with results from the quadruple *mesp* mutant, this suggests that *tbx6* is required to establish the spatial pre-pattern composed of *mesp* genes and *papc*, which are themselves necessary for somite boundary epithelialization. In *ripply1*-MO-injected embryos, the expression patterns of *papc* and *mesp-b* still appeared striped in the PSM, but extended ectopically, without stripes, in what would normally be the region of the paraxial mesoderm containing the somites. Interestingly, the expression pattern of *mesp-a* is unchanged in these embryos (Kawamura et al., 2005). Thus, unlike *tbx6*, *ripply1* does not seem, at first glance, to be involved in establishing the spatial pre-pattern, but rather in ensuring that the pre-pattern is converted into somite boundaries.

Another *ripply* gene, *ripply2*, was found to be expressed as two stripes in the rostral part of S-1 and S-2 but injections of *ripply2*-MOs did not cause any segmentation defect, suggesting that *ripply2* alone is not required for somite formation (Kawamura et al., 2005). However, *mesp-b* striped expression is lost in *ripply1/ripply2* double morphants but not in *ripply1* or *ripply2* single morphants, suggesting some functional redundancy between the two *ripply* genes (Moreno et al., 2008). Together, these results indicate that *tbx6* and both *ripply* genes are required to establish the spatial pre-pattern that will position the presumptive somite boundaries. For this reason, I define their molecular role as the core of the wavefront (Figure 3A).

The expression of *ripply1* is greatly reduced in *fused somites*, suggesting that Tbx6 activates *ripply1* expression (Figure 4A) (Kawamura et al., 2005). Tbx6 was shown to bind near the *ripply1* promoter by ChIP-seq experiments (Windner et al., 2015). In turn, Ripply1 can antagonize Tbx6 as a transcriptional activator in cell culture by associating with Tbx6 and converting it into a repressor via the recruitment of the transcriptional co-repressor Groucho (Kawamura et al., 2008). The expression domain of *tbx6* is located far anterior to its protein domain, suggesting some post-transcriptional regulation of Tbx6 in the anterior PSM (Wanglar et al., 2014). Interestingly, *ripply1*, which is expressed in the anterior PSM, was found to negatively regulate Tbx6 at the protein level (Figure 4A) (Windner et al., 2015). In mice, this negative regulation is mediated by ubiquitin-dependent protein degradation (Oginuma et al., 2008). While the Tbx6 protein domain is slightly expanded anteriorly in *ripply1* morphants, it expands further in *ripply1/ripply2* double morphants, suggesting again some redundancy between Ripply1 and Ripply2 in the degradation of Tbx6 proteins (Wanglar et al., 2014). Thus, Ripply function appears to act on two aspects of Tbx6 in the anterior PSM, converting Tbx6 transcriptional activation into repression and causing degradation of Tbx6. The relative importance of these mechanisms in vivo remains unclear.

Immunostaining with anti-Tbx6 antibody revealed a dynamic pattern of Tbx6 proteins, repeating for every new somite (Figure 4C) (Wanglar et al., 2014). First, the core domain of Tbx6 proteins spans most of the PSM. The anterior border of this core domain was found to coincide with the posterior-most stripe of *mesp-a* and *mesp-b* expression. This is followed later by the elimination of Tbx6 in the anterior part of the core domain, except in an anterior band coinciding with *mesp* expression. This anterior band is then degraded, resulting in a new, sharp boundary of the Tbx6 core domain located about one segment length more posterior than the previous boundary. This boundary coincides with the onset of *mesp-ab* expression at B-II, suggesting that this sharp Tbx6 boundary is involved in setting up the spatial pre-pattern.

Since Ripply1 and Ripply2 negatively regulate Tbx6 proteins, they are thought to position the anterior edge of the Tbx6 core domain (Wanglar et al., 2014). Furthermore, the Tbx6 core domain is expanded anteriorly and its anterior edge is no longer sharp in *ripply1/ripply2* double morphants. The phenotype of the *ripply1* mutant, e.g. the lack of somite boundaries, is rescued in $tbx6^{+/-};ripply1^{-/-}$ embryos, suggesting that the gene dosage between

tbx6 and *ripply* genes matters for somite boundary formation (Kinoshita et al., 2018). It should be noted that *tbx6+/-;ripply1-/-;ripply2-/-* does not segment, confirming that ripply genes are required for boundary formation.

Interestingly, the sharpness of the anterior border of Tbx6 is also affected in DAPT-treated embryos and in *her1/her7* double morphants (Wanglar et al., 2014). This indicates that the segmentation clock is also involved in establishing the anterior border of Tbx6, but the mechanism by which this is achieved remains elusive. I discuss the interactions between the clock and the wavefront in section 1.4.

1.3   The morphogen gradients

As the role of morphogen gradients in the segmentation clock is not directly related to the present work, I only briefly review it here. The position of the wavefront is adjusted by the mutual interplay of three morphogen gradients, Wnt, Fgf and Retinoic Acid spanning the PSM. This concept is grounded on transient perturbation experiments from multiple species, in which up- or down-regulation of the morphogens signaling lead to changes in the position of the somite boundaries, and thereby the length of somites (Sawada et al., 2001; Dubrulle et al., 2001; Bajard et al. 2014; Kawakami et al., 2005). Importantly, the change in segment length always occurs with a substantial delay after the time of perturbation. Combined with the advection of cells through the PSM, this delay suggests that the signaling gradients act on segmentation at a location in the PSM that is more posterior than the arrest of the clock and the emergence of mesp gene expression. This location is thought to be at or around S-V (Akiyama et al., 2014; Bajard et al., 2014; Dubrulle et al., 2001; Sari et al., 2018; Sawada, 2001).

The three morphogens span the PSM in an opposing and graded manner. Wnt and Fgf ligands are expressed in the tailbud cells and build an anteriorly-decreasing gradient, likely involving diffusion as well as the gradual decay of their protein and/or mRNA in the cellular advection (Dubrulle et al., 2004; Aulehla et al., 2003; Bajard et al. 2014). In contrast, Retinoic Acid ligand is synthesized in the somites and diffuses posteriorly, against the cell flow, across the PSM (Moreno et al. 2008) (Figure 1A). Throughout somitogenesis, the tail elongates from the posterior end whilst new somites are being formed anteriorly. As a result, the positional information of the morphogen gradients is progressively moving down the anterior-posterior axis as the embryo grows (Dubrulle 2001; Oates et al., 2012; Ishimatsu et al., 2018). At the same time, in the co-moving reference frame of the PSM, these gradients could mark a specific position *within* the PSM.

1.4   Interactions between the Clock and the Wavefront

In mice, *Mesp2* expression was found to coincide with the anterior end of the Tbx6 domain (Oginuma et al., 2008), suggesting that, as in zebrafish, the anterior boundary of the Tbx6

domain spatially controls the pre-pattern prefiguring somite boundaries. In contrast with the role of *mesp* genes in zebrafish, *Mesp2* is required for the formation of morphological boundaries (Saga et al., 1997) and seems to be actively involved in setting up the location of presumptive somite boundaries (Oginuma et al., 2008). The expression of *Mesp2* is controlled by both Tbx6 and Notch signaling (Yasuhiko et al., 2006), suggesting that in mice the Clock (via Notch signaling) and the Wavefront (Tbx6) interact through *Mesp2.*

In zebrafish, *mesp* genes are not strictly required for the formation of somite boundaries (Yabe et al., 2016) and the anterior somites form normally in Delta-Notch mutants (Jiang et al., 2000; van Eeden et al., 1996). It is therefore unlikely that the Clock and the Wavefront interact through *mesp* and Notch signaling. While the Clock (section 1.3) and the Wavefront (section 1.4) are relatively well-understood in isolation, how they interact to establish the spatial pre-pattern, i.e. the main output of the segmentation clock, remains surprisingly elusive in zebrafish. How the signalling gradients described in section 1.3 adjust the location of the wavefront is also unclear, and is beyond the scope of the thesis.

1.5   Aims of the thesis

In this work, I investigate how the wave pattern instructs cells to become part of somite boundaries. In Chapter 2, I investigate how the wave pattern interacts with the wavefront to establish the spatial pre-pattern during early somitogenesis. It has been reported that a number of oscillations and waves of gene expression precede the formation of the first boundary in chick, zebrafish, and more recently in mice (Falk et al., 2022; Ishimatsu et al., 2010; Jouve et al., 2002; Riedel-Kruse et al., 2007). This raises the question of why some waves of gene expression prefigure somite boundaries while some do not. Can we observe differences, for examples in terms of wavelength, amplitude or synchronization, between waves that prefigure or that do not prefigure somite boundaries? Answering this question may help us understand what features of the wave pattern (the Clock) are read by the Wavefront to produce a sharp striped pattern prefiguring somite boundaries.

In Chapter 3, I address the question of what level of synchrony in the wave pattern is required for the correct formation of somite boundaries. I also investigate how a coherent tissue-level pattern emerges de novo from a population of noisy oscillators. In this chapter, I hope to understand the robustness of the segmentation clock as a patterning system.

Chapter 2   Interactions between the clock and the wavefront during early somitogenesis[2]

2.1   Background

An important step of zebrafish development is epiboly, defined by Kimmel and colleagues as "the thinning and spreading of both the yolk syncytial layer and the blastodisc over the yolk cell, as you might model by pulling a knitted ski cap over your head." (Kimmel et al., 1995). For a thorough description of epiboly and of the development of the zebrafish embryo in general, see the excellent paper (Kimmel et al., 1995). In zebrafish, the segmentation clock is thought to start at around 40% epiboly (~5hpf), with the onset of *her1*, *her7* and *deltaC* expression, hours before the formation of the first morphological somite boundary at bud stage (10hpf) (Ishimatsu et al., 2010; Riedel-Kruse et al., 2007). Using time-course *in situ* hybridization, these studies reported that several oscillations of the segmentation clock preceded the formation of the first boundary (Ishimatsu et al., 2010; Riedel-Kruse et al., 2007). The first three to four cycles are reported to be restricted to the blastoderm margin. One study reported that these oscillations formed travelling waves around the margin (Riedel-Kruse et al., 2007), but this was not observed in the other study (Ishimatsu et al., 2010). The fourth, respectively the fifth, cycle was reported to form a wave of gene expression travelling from the margin towards the animal pole, starting at 7.8 hpf (Ishimatsu et al., 2010), respectively 8.2 hpf (Riedel-Kruse et al., 2007). The sixth cycle of the clock, starting at 8.7 hpf was thought to prefigure the first somite boundary (Riedel-Kruse et al., 2007). Due to the low temporal resolution of time-course *in situ* hybridization, there are some temporal disparities in the two aforementioned studies. However, they both suggest that a few waves of gene expression precede the formation of the first boundary. Similarly, two oscillations were found to precede the formation of the first somite in chick and mice (Jouve et al., 2002; Falk et al., 2022). Recently, the onset of the mouse segmentation clock has been time lapsed with lightsheet microscopy, providing a deeper insight into the dynamics of this process and confirming that some oscillations take place before somites actually form (Falk et al., 2022).

Because it allows the comparison between travelling waves that prefigure or do not prefigure the formation of somite boundaries, the onset of the segmentation clock provides a unique context to study the interaction between the Clock and the Wavefront without perturbing these processes. In addition, we also aim at investigating, using live imaging, which travelling wave prefigures which somite boundary. A mapping between a given kinematic wave and a given somite boundary currently does not exist. Such a mapping would help understanding how the wave pattern instructs cells to become part of a somite boundary. This mapping would notably allow to assign a specific travelling wave to the formation of a defective somite boundary, for example in the context of the desynchronization of the segmentation clock. This would greatly help to understand what features of the wave pattern distinguish normal from defective somite boundaries. Furthermore, it may also give insight

---

[2] The work in this chapter was done with the assistance of Chloé Jollivet for injections, imaging and cell tracking. Virginie Braman genotyped *tbx6-mneongreen;her1$^{+/-}$;her7$^{+/-}$* and *tbx6-mNeonGreen;her1$^{-/-}$;her7$^{-/-}$*embryos.

into the control of the transition between the head mesoderm and trunk mesoderm along the body axis.

In a broader perspective, the formation of the first, anterior-most somites present an evo-devo interest. In zebrafish, the formation of anterior and posterior somites appears to be different, both in terms of genetics and morphogenesis. The synchronous onset of the segmentation and the emergence of travelling waves are Notch-independent in zebrafish and mice (Falk et al., 2022; Ishimatsu et al., 2010; Riedel-Kruse et al., 2007). As a result, the first five to ten somites form normally in Notch pathway mutants and in embryos treated with DAPT (Riedel-Kruse et al., 2007; van Eeden et al., 1996). In contrast, anterior somite boundaries are missing in the homozygous *mesp* quadruple mutant, while posterior somite boundaries still form (Yabe et al., 2016). Therefore, Notch signaling is not required for the correct formation of the anterior somites in zebrafish, but *mesp* function is necessary. As a side note, the first seven somite boundaries are defective in the integrin-α5 mutant *bfe*, suggesting that morphological somite boundary formation also differs between anterior and posterior somites.

The elongation of the body axis drastically changes over the course of somitogenesis. Anterior somites form while extensive convergence-extension movements drive the axis elongation. As a consequence, cells contributing to somites 1 to 12 are already in the PSM at the end of epiboly, and, in contrast to cells contributing to more posterior somites, do not pass through the tailbud (Kanki and Ho, 1997; Steventon et al., 2016). Can these differences between the formation of anterior and posterior somites be understood in the light of evo-devo?

The developmental hourglass model depicts the evolution of the phylogeny between vertebrate embryos from different species over their developmental time (Duboule, 1994). Embryos from different species exhibit a great amount of variability in the very beginning of their development, which is represented by the wide part of the hourglass. However, this variability then decreases due to developmental constraints as embryos progress through gastrulation. This stage, which also corresponds to the beginning of the Hox timer and the segmentation clock, represents the neck of the hourglass. Goodrich observed that "a constant relation often becomes established between certain segments and certain organs or differentiated parts" (Goodrich, 1913). He also noted that vertebrae were "generally speaking (…) more definite and invariable in the anterior than in the posterior region" (Goodrich, 1913). It has hence been proposed that anterior segments are subjected to more developmental constraints than posterior segments, which, in return, have higher adaptability and evolvability (Duboule, 2022; Goodrich, 1913). The formation of posterior somites corresponds to the part of the hourglass where the neck gradually opens up. Whether the segmentation clock is involved in tuning the adaptability of somite formation over the course of somitogenesis is unclear.

Evo-devo considerations suggest that developmental constraints are stronger for anterior somites than for posterior somites. Several lines of evidence show that the formation of anterior and posterior somites differ in some aspects. At the same time, somitogenesis lasts over 15 hours, during which the embryo undergoes massive shape changes. Therefore, some changes in somite formation over time are to be expected. Does the segmentation clock change over the course of somitogenesis by tuning some parameters of the Clock and/or the Wavefront? Or do the Clock and the Wavefront interact in different ways to establish the pre-pattern that prefigures the boundaries of anterior versus posterior

somites? To address these questions, we imaged, using lightsheet microscopy, zebrafish transgenics with novel Her1, Mespb and Tbx6 reporters at the onset of the segmentation clock and during early somitogenesis.

2.2   Results

2.2.1   Characterization of the wave pattern during epiboly

Traditionally, zebrafish embryos are mounted laterally, with the yolk sitting in a conical depression patterned in low-melting agarose (Soroldoni et al., 2014; Rohde et al., 2021). This method works well to image somite formation in the posterior trunk and outgrowing tail. However, from 30% epiboly until the formation of anterior trunk somites, zebrafish embryos undergo massive morphological changes, making the imaging of the segmentation clock very challenging since the margin, and later the PSM, need to be in the field of view for the whole timelapse. This could certainly be done with multiview lightsheet imaging, for example using the Zeiss Z1 lightsheet microscope. However, multiview imaging of multiple embryos is unlikely to achieve the high temporal resolution required to enable cell tracking. Therefore, we designed, in collaboration with Viventis Microscopy, a new way of patterning agarose for mounting zebrafish embryos on LS1 Live, Viventis dual-illumination lightsheet microscope.

In this work, the agarose is patterned with conical depressions, similar to those used for lateral imaging, but a trough is patterned underneath them so that the tail of the embryo can elongate freely when the embryo is imaged dorsally (Fig. Mounting). By mounting the embryo in the conical depressions with the animal pole up, the margin can be imaged throughout epiboly. Convergence-extension gradually brings the cells to the dorsal side of the embryo. By bud stage, the embryo finds itself out of equilibrium and rotates to a new stable position, where the PSM either faces the imaging lens or faces 180 degrees away. When the PSM faces the imaging lens, the segmentation clock can be imaging from its very beginning until around 12ss (10 hours of imaging at 28.5°C). A limitation of this mounting technique is that, when the PSM does not face the imaging lens, the embryo cannot be properly imaged and the timelapse for this specific embryo has to be discarded. From our experience, the embryo rotates to one position or the other with equal probability. To sum up, we designed a new mold for patterning the agarose which allows multiple embryos to be imaged, while freely growing, at high temporal resolution from mid-epiboly to mid-somitogenesis.
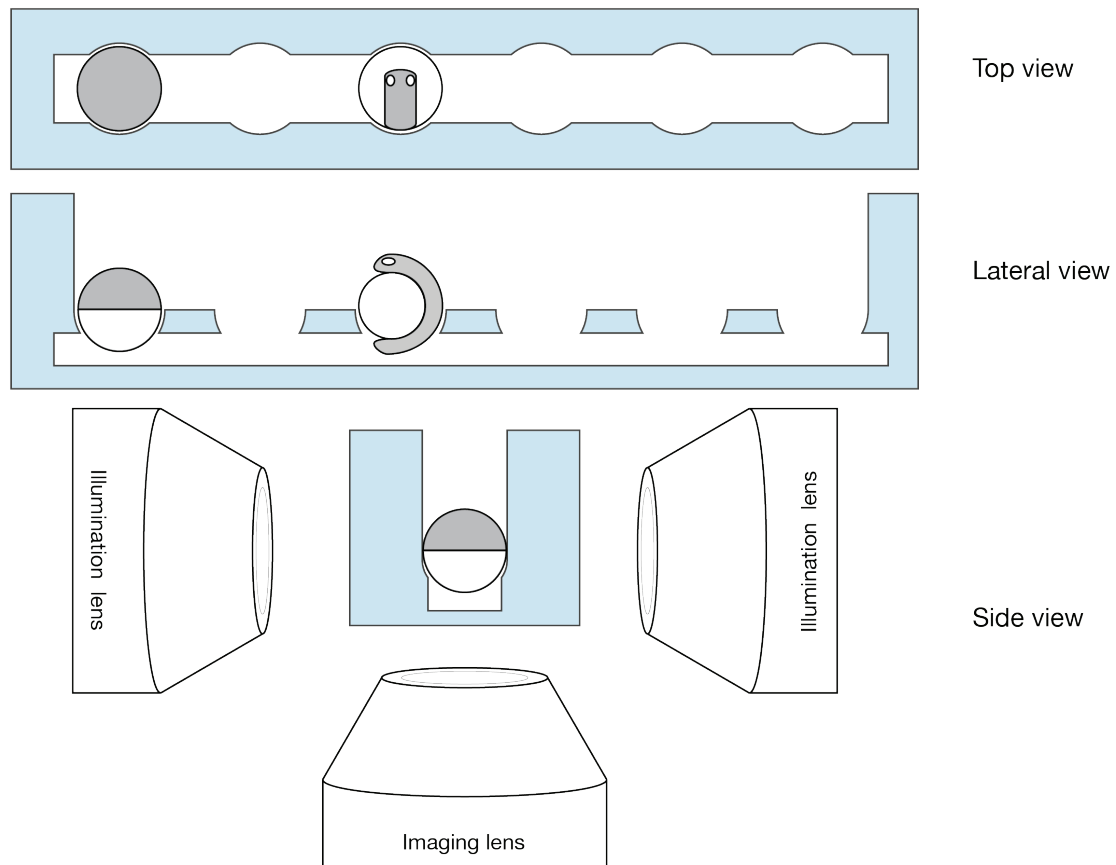
Figure 5: **Schematic of the lightsheet imaging setup.** Zebrafish embryos are mounted in low-melting agarose patterned to support the yolk while not constraining the growth of the embryos. Embryos are mounted with the animal pole up around 30% epiboly. As epiboly proceeds, the margin gets closer to the imaging lens. Once the tail is formed, it can extend freely with the PSM facing the imaging lens.

Using this new mounting system, we imaged zebrafish embryos containing both the Looping (Her1-YFP) transgene (Soroldoni et al., 2014) and a novel BAC transgene named Heidi that expresses a fluorescently-tagged Mespb fusion protein from the genomic regulatory region (Mesp-ba-mKate2) (Rodhe et al., 2022). Embryos were injected with H2B-mCerulean mRNA at 1-cell stage so that nuclei can be visualized, and further used as a marker for cell tracking. As *her1* expression was reported to start at 5 hpf (Ishimatsu et al., 2010), we started the timelapse around 30% epiboly to capture the onset of the segmentation clock. Movie 1[3] shows the maximum-intensity projection of a representative embryo. To better visualize the dynamics of the segmentation clock during epiboly, the timelapse was transformed using a method called elliptic transformation that that is similar to how the Earth is projected on a map. Briefly, an ellipsoid was fitted to the embryo and the dataset was transformed to be represented in spherical coordinates. Movie 2 shows the maximum-intensity projection of the transformed dataset. As for a Mercator projection, the poles are distorted but the equator is preserved. Therefore, the equator of the ellipsoid was set as an anteroposterior line located at an equidistance between the two sides of the PSM. During epiboly, this line is perpendicular to the margin, passing through the shield. During

---

[3] Movies can be found here : https://drive.google.com/drive/folders/1NCG-R2nhvzzv5qoCWdMK-beyQSN98Fs29?usp=share_link

somitogenesis, the line aligns with the notochord. We then projected the transformed dataset using a maximum-intensity projection to generate kymographs (Fig. 6A).

The Her1-YFP signal appeared about 20 minutes before the involution of cells at the blastoderm margin (data not shown), which marks the beginning of gastrulation at 50% epiboly (5.25 hpf), indicating that the onset of the segmentation clock occurs shortly before the start of gastrulation. The Her1-YFP signal quickly spread around the margin before travelling towards the animal pole in cells located in the epiblast (Fig. 6B). This travelling wave can be appreciated from the kymograph in Fig. 6A and from the Movie 2. Note that in Fig. 6A, the margin is located at the posterior part of the kymograph (left) while the animal pole is at the anterior part (right). The timing of the first clock oscillation is coherent with what was previously reported from *in situ* hybridization staining (Ishimatsu et al., 2010; Riedel-Kruse et al., 2007), but the fact that the signal travels from the margin to the animal pole was not apparent in the *in situ* hybridization staining. The duration of this first cycle was approximately 45 minutes.

A second wave of Her1-YFP signal traveled from the margin towards the animal pole when the embryo is at shield stage (6hpf). This wave took place all around the margin, both in the epi- and hypoblast (Fig 6B). Interestingly, cells in the hypoblast are advected towards the animal pole, in the same direction as the wave, while cells in the epiblast are advected in the opposite direction. This indicates that, at least this wave is kinematic and does not rely on cell advection.

When the third wave started, the shield was now formed and devoid of Her1-YFP signal. Except for the shield, Her1-YFP was still expressed all around the margin but its expression was stronger on both sides of the shield (Fig 6B). This wave took place exclusively in the hypoblast.

At around 75% epiboly, a fourth wave, seemingly restricted to the PSM, traveled a much longer distance than previous waves (Fig. 6A and B). This is in agreement with results from *in situ* hybridization staining reporting a wave of *her1* expression travelling anteriorly at 70% epiboly (Ishimatsu et al., 2010). As the fourth Her1-YFP wave arrived in the anterior PSM, a fifth wave started travelling from the posterior PSM (Fig. 6B).

This description of the onset of the segmentation clock was obtained by analyzing kymographs and timelapses of 3 different embryos. This suggests that the dynamics of the segmentation clock is, to some large extent, in register with the progression of epiboly.

Using lightsheet timelapse microscopy, we obtained a better understanding of the dynamics of the segmentation clock during epiboly and early somitogenesis. We found that the first cycles of the segmentation clock manifests as waves travelling anteriorly, which contrasts with previous results from *in situ* hybridization reporting that *her1* oscillations were restricted to the blastoderm margin (Ishimatsu et al., 2010; Riedel-Kruse et al., 2007). The

difference in temporal resolution between timelapse microscopy and snapshots from time-course *in situ* hybridization is likely to account for the observed disparity.

As a next step, we wanted to re-address the question of what travelling waves prefigure the formation of the first few somite boundaries using lightsheet timelapse imaging and cell tracking. Simultaneously, we also hoped to understand how the segmentation clock pre-figures the first somite boundary by comparing the oscillatory traces of cells forming the anterior boundary of somite 1 with cells located just anterior to this boundary in the head mesoderm.

2.2.2 The 4th kinematic wave of Her1 expression prefigures the first somite boundary

Using the H2B-mCerulean signal, we back-tracked cells from four categories: cells forming the anterior boundary of somites 1, 2 and 3, and cells located just anteriorly to the first somite boundary, hereafter called « S1 - Anterior », « S2 - Anterior », « S3 - Anterior » and « Anterior to S1 » (Fig. 7A and B). Fig. 7C shows the mean intensity and standard deviation of Her1-YFP (filled line) and Mesp-ba-mKate2 (dashed line) signals in the aforementioned categories in a representative embryo. The numbers 1 to 5 relate to the wave numbers in Fig. 6.

Most cells in « S1 - Anterior » made 4 oscillations (10/12 cells), with only 2 daughter cells making 5 oscillations (Fig. 7A). The Mesp-ba-mKate2 signal rose after most cells have com-pleted their fourth cycle and while the two cells displaying five oscillations finish their fifth cycle (Fig. 7C). In cells from « S2 - Anterior », respectively « S3 - Anterior », the Mesp-ba-mKate2 signal rose after 5, respectively 6, Her1-YFP oscillations. The relationship between the number of cycles and the somite number can be explained by the time duration that cells spent in the PSM after the onset of the segmentation clock.

To confirm that the results are not specific to a single embryo, we pooled single cell traces from 3 embryos and we temporally aligned Her1-YFP traces using the time at which em-bryos completed epiboly as a temporal reference. Fig. 8A shows individual Her1-YFP traces, color-coded by embryos, and their mean intensity (thick black line), for the four categories depicted in Fig. 7B. The fact that single cell traces from different embryos can be aligned according to the time of epiboly completion is further evidence that the dynam-ics of the segmentation clock is temporally registered with the progression of epiboly.

The fact that most cells forming the first boundary display four oscillations (Fig. 7A and C, Fig. 8A) suggests that the first boundary is prefigured by wave number 4, or less. While we cannot formally rule out the possibility that the third wave prefigures the first boundary, spatio-temporal considerations make this possibility very unlikely. Indeed, the third wave only traveled a very short distance (Fig. 6A) and arrived in the anterior PSM before 75% epiboly, more than two hours before the morphological formation of the first boundary. In

addition, cells forming the first boundary displayed their third oscillation around 2 hours before the appearance of the Mesp-ba-mKate2 signal. For these reasons, it is unlikely that the third wave prefigures the first somite boundary.

Together, these results strongly suggest that the fourth wave, travelling in the PSM at 75% epiboly, prefigures the first somite boundary. The fifth and sixth waves prefigure the second and third somite boundary, respectively. Assuming that a travelling wave prefigures a somite boundary, we can extrapolate that the nth somite boundary is prefigured by the wave number n+3. This provides, for the first time, a mapping between kinematic waves and the somite boundaries they prefigure.

Interestingly, most cells located anteriorly to somite 1 also display four oscillations but did not turn on Mesp-ba-mKate2 (Fig. 7A and C, Fig. 8A). This suggests that cells forming the first somite and cells located anteriorly to the first somite cannot be discriminated based on their Her1-wave pattern. We hypothesized that the wavefront might discriminate between these two cell populations. To test that hypothesis, we imaged the transgenic line Tbx6-mNeonGreen during epiboly and early somitogenesis.
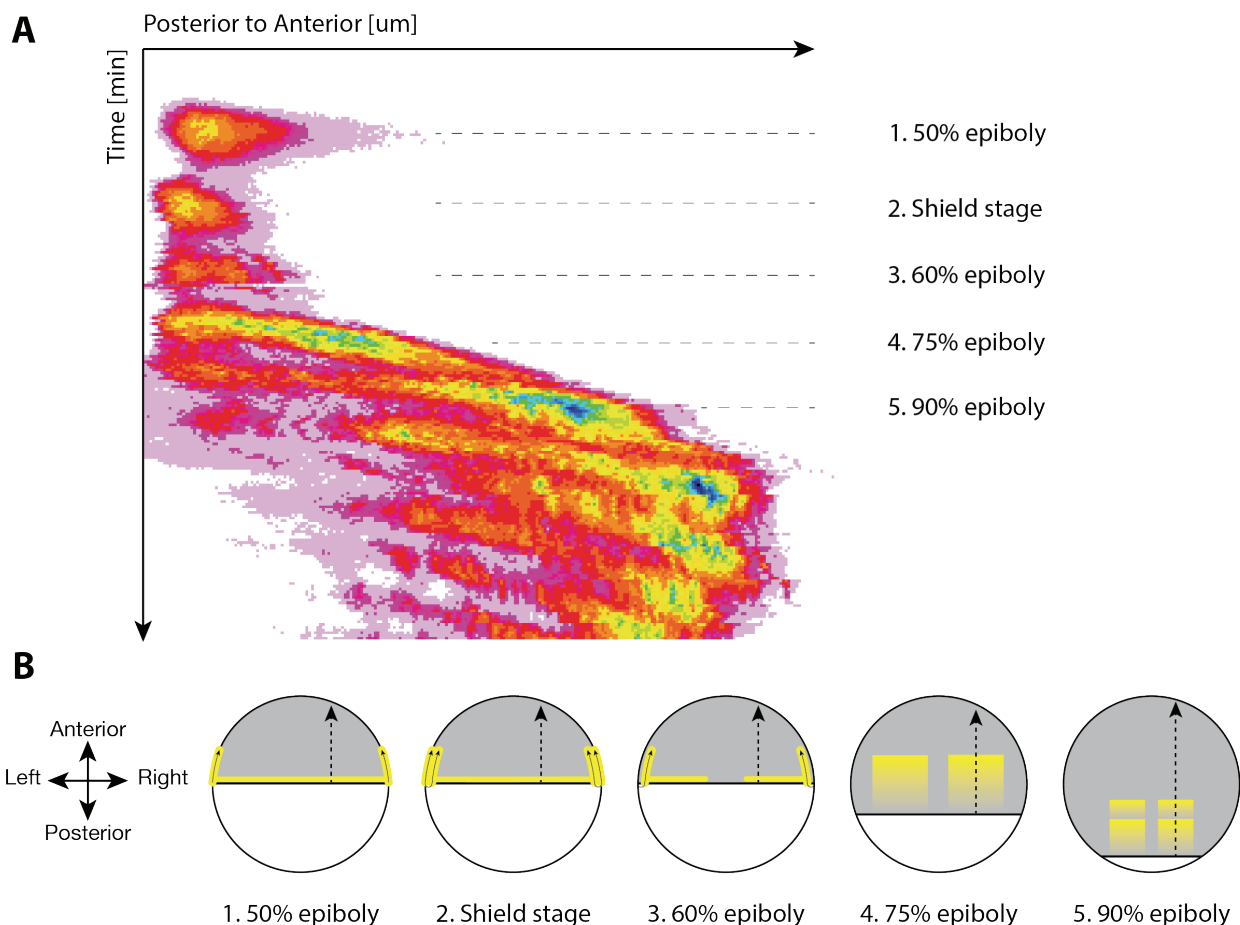
Figure 6: **Her1-YFP expression during the onset of the segmentation clock.** A) Kymograph of a representative Her1-YFP embryo with the staging of the first five travelling waves. B) Schematic of the location of the first five travelling waves in the embryo (with animal pole up) during epiboly. The arrows, pointing towards the anterior, show the position of the lines of interest used to generate the

kymograph in A). The first wave travels from the blastoderm margin towards the animal pole but is limited to epiblast. The second wave travels anteriorly from the margin in both the epiblast and the hypoblast. The third wave is restricted to the hypoblast and the shield is devoid of signal. The fourth wave travels in the left and right PSM that is located in the hypoblast. Around 90% epiboly, several waves simultaneously travel in the PSM.
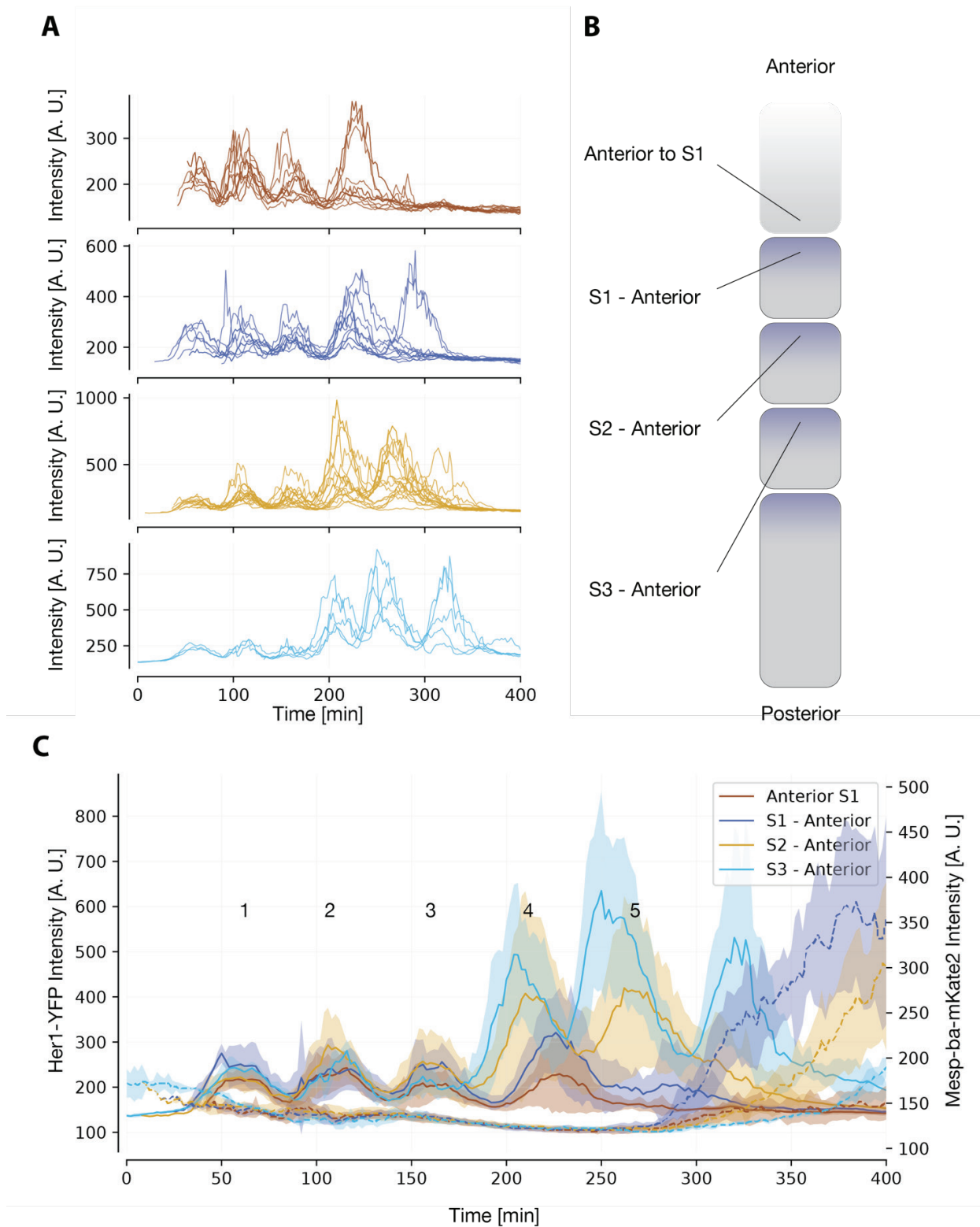
Figure 7: **Her1-YFP and Mesp-ba-mKate2 time traces in single cells during epiboly and early somitogenesis.** A) Her1-YFP traces in cells from categories depicted in B). B) Single cells were back-tracked from four locations illustrated at the 3-somite stage: anteriorly to the first somite boundary, the anterior boundary of somites 1, 2 and 3, labelled « Anterior to S1 », « S1 - Anterior », « S2 - Anterior » and « S3 - Anterior », respectively (n = 13, 12, 17 and 5 cells, respectively). C) Mean intensity (line) and standard deviation (colored surface) of Her1-YFP (filled line) and Mesp-ba-mKate2 (dashed line) signals. Her1-YFP peaks are numbered from 1 to 5 according to the corresponding travelling waves in Fig. 6A and B.
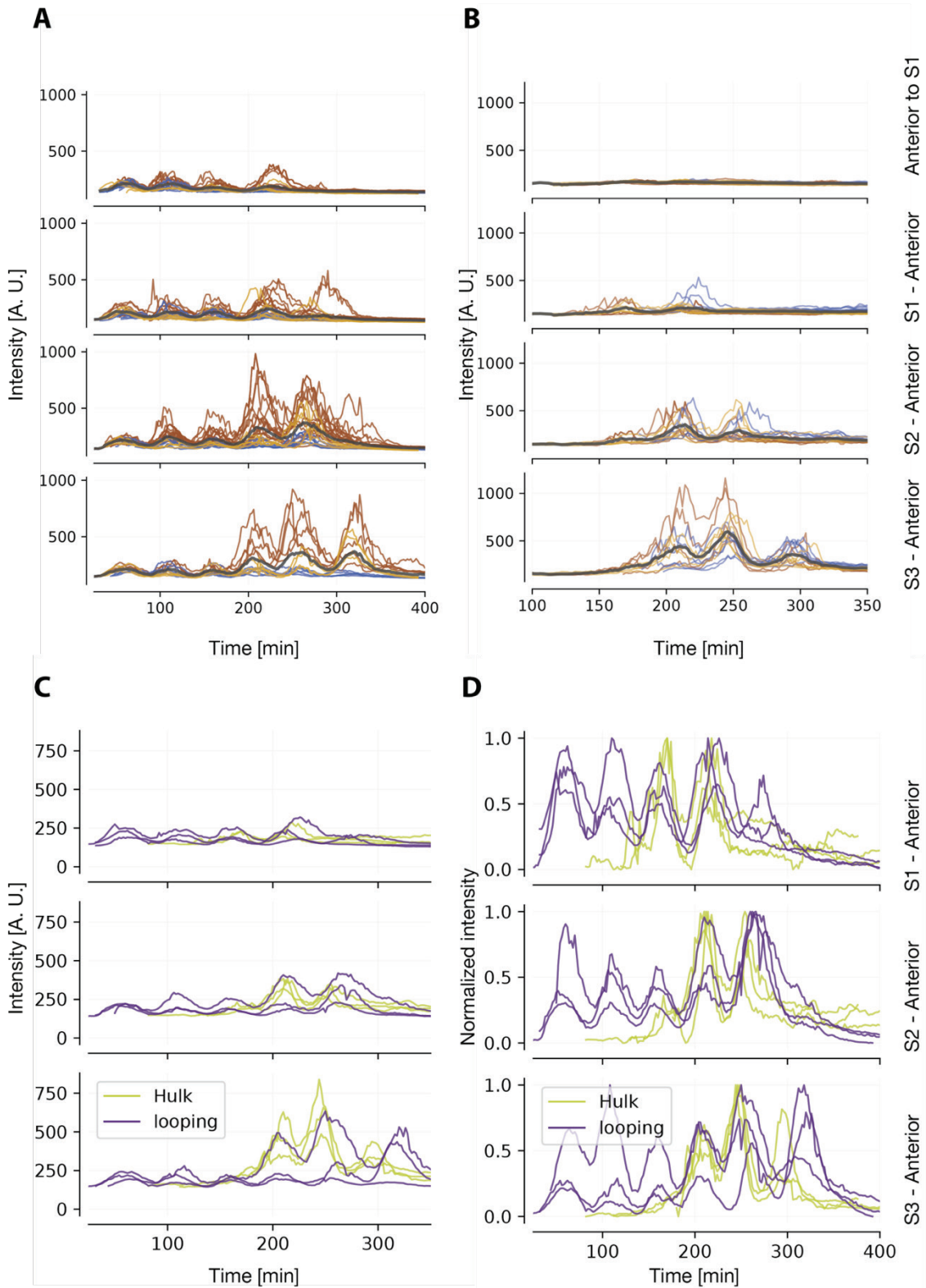
Figure 8: **Pooled Her1-YFP and Tbx6-mNeonGreen traces.** A) Individual Her1-YFP traces in categories « Anterior to S1 », « S1 - Anterior », « S2 - Anterior » and « S3 - Anterior » are temporally aligned between 3 embryos (n = 29, 28, 30, 14 cells in categories « Anterior to S1 », « S1 - Anterior », « S2 - Anterior » and « S3 - Anterior », N = 3 embryos). The mean intensity of the traces, pooled from 3 embryos, is displayed as a thick black line. B) Individual Tbx6-mNeonGreen traces in categories « Anterior to S1 », « S1 - Anterior », « S2 - Anterior » and « S3 - Anterior » are temporally aligned between 3 embryos (n = 24, 26, 20 and 15 in categories « Anterior to S1 », « S1 - Anterior », « S2 - Anterior » and « S3 - Anterior », N = 3 embryos). The mean intensity of the traces, pooled from 3 embryos, is displayed as a thick black line. C) The means intensities of Her1-YFP (blue) and Tbx6-mNeonGreen (yellow) signals in individual embryos are temporally aligned to visualize the temporal correlation between Her1-YFP and Tbx6-mNeonGreen. D) The mean intensity from C) is normalized to better visualize the relationship between both signals.

2.2.3 Characterization of Tbx6-mNeonGreen dynamics

To visualize the dynamics of the Tbx6 protein, a new transgenic line was generated using BAC recombineering to express a Tbx6-mNeonGreen fusion protein from the correct genomic regulatory region. Generation and benchmarking of the transgenic line was performed by Chloé Jollivet in our lab, and is not yet published. Briefly, immunostainings and *in situ* hybridization confirmed that the transgene was expressed where expected. In the progeny of the cross of *tbx6-mNeonGreen$^{+/-}$;tbx6$^{+/-}$* with *tbx6$^{-/-}$*, somites form in 100% (30/30) of the embryos that are positive for Tbx6-mNeonGreen while they only form in 15% (2/13) of Tbx6-mNeonGreen-negative embryos. Therefore, Tbx6-mNeonGreen rescues the phenotype of the *tbx6$^{-/-}$* mutant *fused somites,* indicating that the transgene is functional. *In situ* hybridization for *xirp2a*, a high contrast and sensitive marker for segmental defects, revealed that half the embryos (8/16) exhibit sporadic defects in myotome boundaries at 36 hpf. These embryos make, on average, five defects (4.75 ± 1.28) along their entire axis. However, no defects were observed in the first five somite boundaries and only 2 embryos out of 16 exhibited defects anteriorly to the eighth boundary. Because of this, we deemed this transgenic line suitable for use during early somitogenesis.

Movie 3 shows the maximum-intensity projection of a representative Tbx6-mNeonGreen embryo starting around 30% epiboly. Movie 4 shows the maximum-intensity of this dataset after an elliptic transformation. As can be appreciated in Movie 4 and in Fig. 9A, the expression of Tbx6-mNeonGreen started around shield stage as expected from mRNA in situ, but, surprisingly, exhibited kinematic waves from 75% onwards. Waves traveled on both sides of the shield and were restricted to the hypoblast Fig 9B.

A

Posterior to Anterior [um]

Time [min]

1. 60% epiboly

2. 75% epiboly

3. 90% epiboly

4. Bud stage

B

Anterior

Left ◄──► Right

Posterior

1. 60% epiboly   2. 75% epiboly   3. 90% epiboly   4. Bud stage
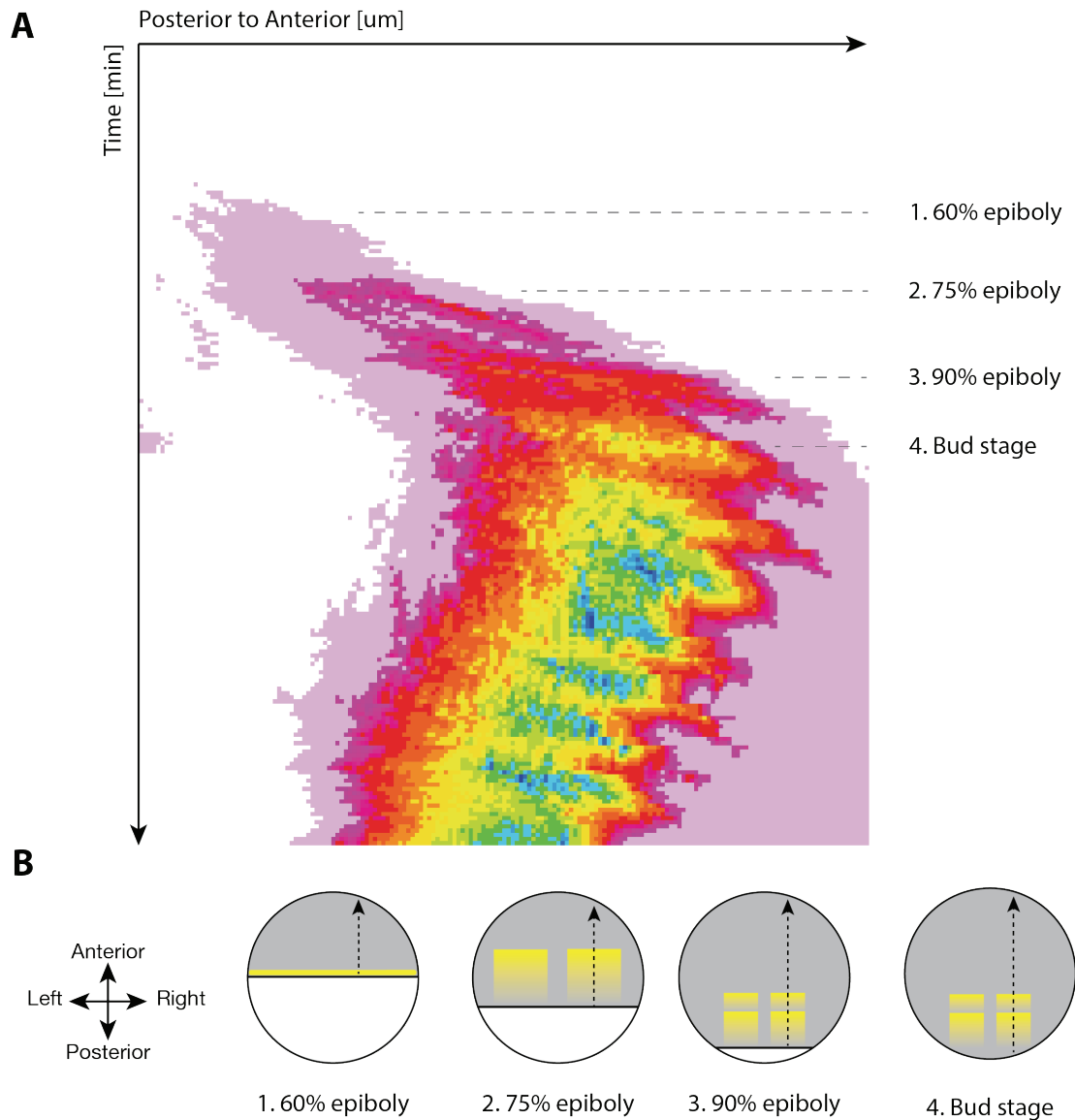
Figure 9: **Tbx6-mNeonGreen expression during the onset of the segmentation clock.** A) Kymograph of a representative Tbx6-mNeonGreen embryo with the staging of the first four travelling waves. B) Schematic of the location of the first four travelling waves in the embryo (with animal pole up) during epiboly. The arrows, pointing towards the anterior, show the position of the lines of interest used to generate the kymograph in A). The first cycle of Tbx6-mNeonGreen does not travel and is restricted to the blastoderm margin. Thereafter, waves of Tbx6-mNeonGreen travel in the PSM, similarly to the Her1-YFP waves described in Fig. 6B.

2.2.4 Tbx6 oscillates at the cellular level during early somitogenesis

To determine if the travelling waves of Tbx6-mNeonGreen signal are phase-waves related to cellular oscillations, we first back-tracked cells from the same locations as we did for Her1-YFP embryos: cells forming the anterior boundary of somites 1, 2 and 3, and cells located just anteriorly to first somite boundary (Fig. 10A and B).

Fig. 10C shows the mean intensity and standard deviation of Tbx6-mNeonGreen (filled line) and Mesp-ba-mKate2 (dashed line) signals in the aforementioned categories in a representative embryo. The numbers 1 to 4 relate to the wave numbers in Fig. 9A and B. Remarkably, cells forming the anterior boundaries of somites 1, 2 and 3 displayed an oscillatory Tbx6-mNeonGreen signal (Fig. 10A). In contrast, cells located just anterior to the first boundary were negative for Tbx6-mNeonGreen. This suggests that the Tbx6 expression

domain defines the location of the first boundary. I will come back to this result in section 2.2.9.

Cells forming the anterior boundary of somites 1, 2 and 3 made 2, 3 and 4 cycles, respectively. These cellular oscillations correspond, at the tissue-level, to the waves of Tbx6 expression observed in Fig. 9A, and are numbered accordingly (Fig. 10C). The first, low-amplitude, cellular oscillation took place during shield stage (Fig. 10C, number 1). Note that this oscillation was not evident in every cell from categories « S2 – Anterior » and « S3 – Anterior ». The second cycle (Fig. 10C, number 2), corresponding to the Tbx6 wave travelling in the hypoblast around 75% epiboly (Fig. 9A, number 2), was the last oscillation of cells forming the anterior boundary of somite 1. This is consistent with the fact that the fourth Her1-YFP wave, also traveling in the hypoblast around 75% epiboly, prefigures the first somite boundary (shown above).

Cells in « S2 – Anterior » made one extra cycle (Fig. 10C, number 3) compared to cells in « S1 - Anterior ». Similarly, cells in « S3 – Anterior » made one extra cycle compared to cells in « S2 – Anterior » (Fig. 10C, number 4). As was the case for Her1-YFP, this relationship between the number of Tbx6-mNeonGreen oscillations and the somite number can be explained by the time duration that cells spent in the PSM after the onset of Tbx6 at shield stage.

To confirm that the results are not specific to a single embryo, we pooled single cell Tbx6-mNeonGreen traces from 3 embryos and temporally aligned the traces using the time of epiboly completion as a temporal reference. Fig. 8B shows the individual Tbx6-mNeonGreen traces, color-coded by embryos, and their mean intensity (thick black line), in cells from the four categories depicted in Fig. 10B. The fact that single cell traces from different embryos can be aligned according to the time of epiboly completion suggests that the dynamics of Tbx6 is also temporally registered with the progression of epiboly.

2.2.5 Tbx6 oscillations decrease at later developmental stages

To determine if Tbx6 oscillations were restricted to cells forming the first three somite boundaries, we back-tracked cells from the anterior boundary of somite 5 and 7 (Fig. 11A and B). Cells forming the anterior boundary of somite 5 displayed obvious oscillations. This indicates that Tbx6 oscillates, not only during the formation of the first three boundaries, but generally during the formation of anterior somites. However, in "S7 – Anterior", the relative level of Tbx6 in the troughs of the oscillations tended to be higher and the amplitude of Tbx6 oscillations was therefore reduced. A gradual increase in the trough levels might induce a smooth transition from oscillatory to non-oscillatory Tbx6 activity at later segmentation stages. This transition is out of the scope of the current work.
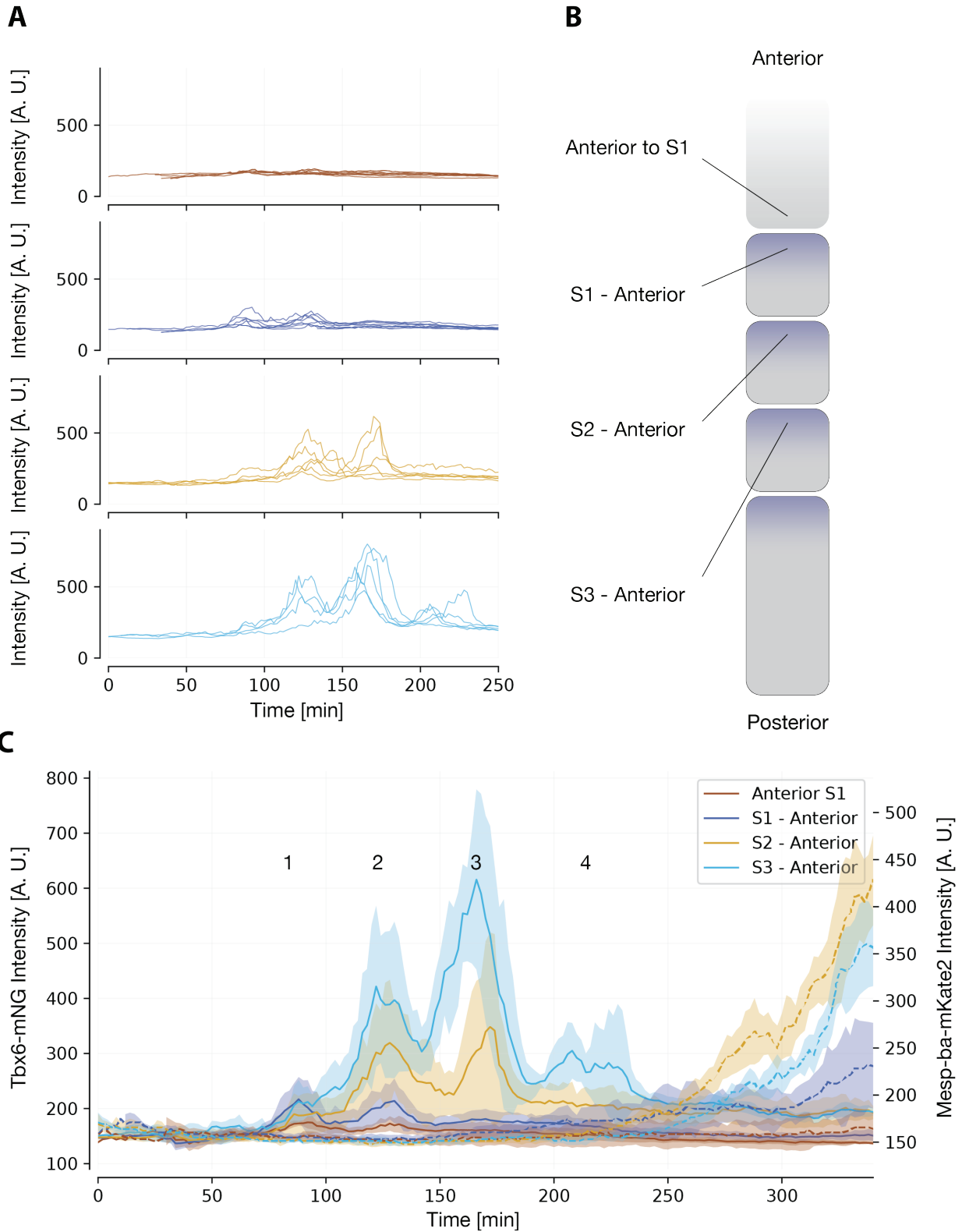
Figure 10: **Tbx6-mNeonGreen and Mesp-ba-mKate2 traces in single cells during epiboly and early somitogenesis.** A) Tbx6-mNeonGreen traces in cells from categories depicted in B). B) Single cells were back-tracked from four locations: anteriorly to first somite boundary, the anterior boundary of somites 1, 2 and 3, labelled « Anterior to S1 », « S1 - Anterior », « S2 - Anterior » and « S3 - Anterior », respectively (n = 9, 9, 6 and 5 cells, respectively). C) Mean intensity (line) and standard deviation (colored surface) of Tbx6-mNeonGreen (filled line) and Mesp-ba-mKate2 (dashed line) signals. Tbx6-mNeonGreen peaks are numbered from 1 to 4 according to the corresponding travelling waves in Fig. 9A and B.

Previous work has not reported evidence of waves of *tbx6* mRNA or Tbx6 protein (Wanglar et al., 2014; Windner et al., 2015). The majority of the work using Tbx6 immunohistochemistry has focused around 8-somite stages or later, potentially explaining why the dynamics reported here may have been missed. Alternatively, the Tbx6 oscillations may be an artifact of the Hulk transgene. To test this latter hypothesis, we performed combined whole-mount *in situ* hybridization for *tbx6* and antibody staining against Tbx6 in wild type embryos, and compared the dynamical pattern of Tbx6-mNeonGreen from timelapses against Tbx6 in wild type embryos.

Before making this comparison, we first needed to generate an expectation of how cellular Tbx6 oscillations would appear in a snapshot at the tissue-level using single time points from a timelapse recording. Fig. 11B shows the location of cells in the tissue (dashed line) at the time of a trough (S5 – Anterior, star) and a peak (S7 – Anterior, star) in oscillations. Despite the clear appearance of waves in the movies and kymographs, peaks and troughs in cellular oscillations were hard to relate to the Tbx6-mNeonGreen pattern in a snapshot at the tissue-level, at least for the cells we back-tracked from somite boundaries.

Nevertheless, in our Tbx6-mNeonGreen timelapses during early somitogenesis we observed the same dynamical pattern of Tbx6 reported by immunostainings at 8 somite-stage (Wanglar et al., 2014) (i.e. the appearance and the disappearance of a Tbx6 upper band) (Fig. 11C, right). Importantly, combined whole-mount *in situ* hybridization for *tbx6* and antibody staining against Tbx6 in wild type embryos at bud stage showed the same dynamical pattern of Tbx6 as observed in Tbx6-mNeonGreen (Fig 11C, left), suggesting that the observed oscillations and waves of Tbx6 expression observed in our timelapses are not an artifact of the transgene.

We next investigated whether Tbx6 oscillations have a transcriptional basis or are due to posttranscriptional regulation. Posttranscriptional regulation by Ripply1/2 is thought to define the anterior boundary of the Tbx6 domain in 8-somite stage embryos, because *tbx6* mRNA expands far anterior to the Tbx6 protein domain at this stage (Wanglar et al., 2014). The expression of *tbx6* mRNA was found to be spatially correlated with Tbx6 protein and did not extend anteriorly (Fig. 11C, left), in contrast to what is reported in zebrafish embryos at 8 somite-stage (Wanglar et al., 2014). This result does not hint at post-transcriptional regulation of Tbx6 during early somitogenesis and we can thus assume that Tbx6 oscillations are transcriptional oscillations.
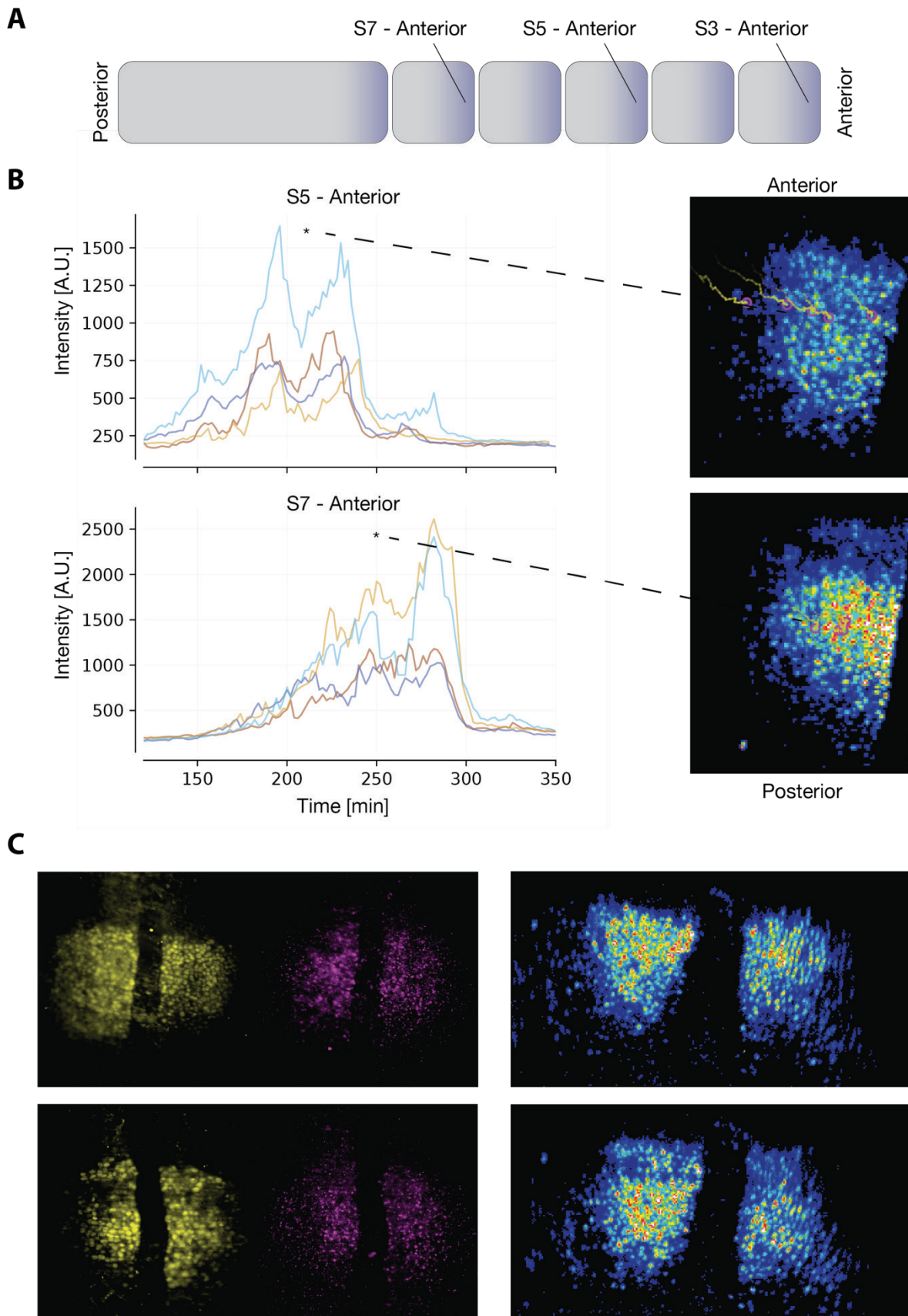
Figure 11: **Tbx6-mNeonGreen oscillate during the formation of anterior somites.** A) Single cells were back-tracked from the anterior boundary of somite 5 and 7. B) Tbx6-mNeonGreen traces in categories "S5 – Anterior" and "S7 – Anterior" (n = 5 and 4 cells, respectively). Cells in "S5 – Anterior" display Tbx6 oscillations. In "S7 – Anterior", the relative level of Tbx6 in the troughs of the oscillations is increased and the amplitude of Tbx6 oscillations is therefore reduced. The stars mark a peak in the category "S5 – Anterior" and a trough in the

category "S7 – Anterior". The dashed line points to the approximate location of the tracked cells at the time of the peak, respectively the trough. Peaks and troughs in cellular oscillations are not readily visible in the Tbx6 pattern at the tissue-level. C) Combined immunostaining against Tbx6 (yellow) and fluorescent *in situ* hybridization for *tbx6* (magenta) in a representative wild type embryo at bud stage (left) show the same dynamical pattern as Tbx6-mNeonGreen (right). The expression of *tbx6* mRNA is spatially correlated with Tbx6 protein, suggesting that the basis for Tbx6 oscillations is transcriptional.

2.2.6 Tbx6 and Her1 oscillate in-phase

Do Tbx6 oscillations constitute an independent oscillator or are they driven by another oscillator? Are they the signature of an interaction between the Clock and the Wavefront? Tbx6 was reported to activate its own expression (Ban et al., 2019). However, oscillatory gene expression are generally considered to require negative-feedback loops (Goodwin, 1965; Monk, 2003). Does the Her1/7 loop repress *tbx6* expression? The *tbx6* promoter contains one E-box binding site (Ban et al., 2019) and bHLH transcription factors, such as Her1 and Her7, are known to bind to E-box sites (Brend and Holley, 2009; Schröter et al., 2012). To address these questions, we compared Tbx6-mNeonGreen and Her1-YFP traces.

As Her1-YFP and Tbx6-mNeonGreen traces from different embryos can be temporally aligned using the time of epiboly completion as a temporal reference (Fig. 8A and B), it is also possible to align Tbx6-mNeonGreen with Her1-YFP. The mean intensity of Tbx6-mKate2 (yellow) and Her1-YFP (blue) in individual embryos is shown in Fig. 8 for cells in the anterior boundary of somite 1, 2 and 3. Comparison between Her1-YFP and Tbx6-mNeon-Green confirms that Her1 started oscillating before the onset of Tbx6 expression. Her1 and Tbx6 appeared to oscillate in-phase, which is better visualized when both signals are normalized (Fig. 8D). This result hints at a potential interaction between the Clock (Her1) and the Wavefront (Tbx6). Indeed, the correlation of Her1 and Tbx6 oscillations is reminiscent of that of *her1* and *deltaC*. The striped expressions of *her1* and *deltaC* have been shown to be spatially correlated, suggesting that their expression is synchronous (Oates and Ho, 2002). In terms of molecular interaction, Her1 is thought to repress *deltaC* expression, potentially driving *deltaC* oscillations (Takke and Campos-Ortega, 1999; Lewis, 2003).

To further investigate a potential interaction between Her1/Her7 and Tbx6, we start by assessing if Tbx6 oscillations are cell-autonomous before imaging Tbx6-mNeonGreen in a *her1⁻/⁻;her7⁻/⁻* background.

2.2.7 Tbx6 oscillates in isolated cells *in vitro*

To determine if Tbx6 oscillations are cell-autonomous, we dissected tailbuds and posterior PSMs of multiple Tbx6-mNeonGreen embryos at bud stage and imaged dissociated cells *in vitro*. Tbx6 oscillates in isolated cells *in vitro* (Fig. 12A). Fig. 12B shows oscillatory traces from several representative cells. Similarly to their behavior *in vivo*, cells make 2 to 4 Tbx6-mNeonGreen pulses *in vitro*, although the oscillations seem to be noisier. While we cannot rule out *cis*-activation of Notch signaling in single cells, such mode a of activation has only been reported in mammalian cell line (Nandagopal et al., 2019). This indicates that Tbx6 oscillations are cell-autonomous and do not require Notch signaling in *trans*. The fact that both Tbx6 and Her1 (Rohde et al., 2021; Webb et al., 2016) oscillate in a cell-autonomous manner further supports a direct interaction between them.
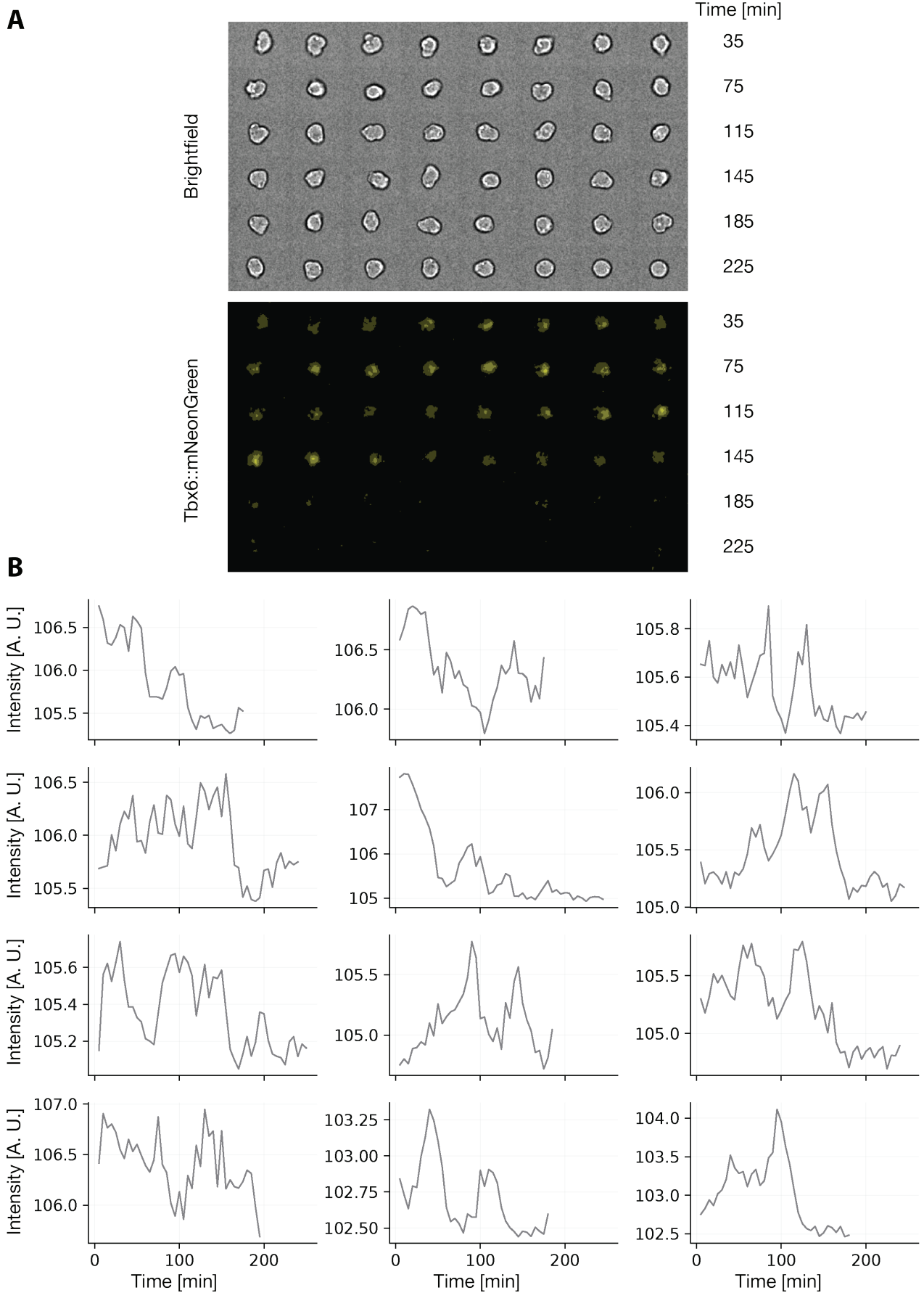
Figure 12: **Tbx6 oscillates in isolated cells *in vitro*.** A) Montage of timelapse images of a representative isolated cell *in* vitro with brightfield (top) and mNeonGreen (bottom) channels. The time interval between images is 5 minutes. Single cells were isolated from tailbud and posterior PSMs. B) Tbx6-mNeonGreen traces from other representative cells.

2.2.8 *her1* and *her7* drive or strongly couple Tbx6 oscillations

Next, we investigated whether the Her1/Her7 loop drives Tbx6 oscillations by imaging *tbx6-mNeonGreen$^{+/-}$;her1$^{-/-}$;her7$^{-/-}$* embryos using lightsheet microscopy. To do so, we outcrossed *tbx6-mNeonGreen$^{+/-}$;her1$^{+/-}$;her7$^{+/-}$* and *her1$^{-/-}$;her7$^{-/-}$* adults. As the *her1* and *her7* loci are only 12kb apart, they segregate together. Therefore, half the embryos that are Tbx6-mNeonGreen-positive are *her1$^{+/-}$;her7$^{+/-}$* and the other half are *her1$^{-/-}$;her7$^{-/-}$*. After the time-lapse, embryos were stained for *xirp2a* using *in situ* hybridization to assess the integrity of segment boundaries and discriminate between the known phenotypes of *her1$^{+/-}$;her7$^{+/-}$* (no defects) and *her1$^{-/-}$;her7$^{-/-}$* (all segments are defective).

Movie 5 shows the maximum-intensity of elliptically-transformed timelapse of a *tbx6-mNeonGreen$^{+/-}$;her1$^{-/-}$;her7$^{-/-}$* embryo. In contrast to Movie 4, waves of Tbx6-mNeonGreen expression are no longer visible. This can also be appreciated with kymographs from representative *tbx6-mNeonGreen$^{+/-}$;her1$^{-/-}$;her7$^{-/-}$* embryos (Fig. 13A, compare with Fig. 9A).

In *her1$^{-/-}$;her7$^{-/-}$* embryos, somite boundaries are severely disrupted and it is therefore challenging to back-track cells from a boundary. Instead, we back-tracked cells from what we estimated to be somite 1, 2 and 3. Our estimation is based on the subtle auto-fluorescence of paraxial mesoderm in the mNeonGreen channel and on the timing of Tbx6-mNeonGreen signal with respect to epiboly completion. In any case, cells in each category were selected from a close vicinity. Although most cells back-tracked from the three somites showed a rising Tbx6-mNeonGreen expression profile, the majority did not exhibit oscillations (Fig. 13B, 14A and B). In contrast, coordinated oscillations are apparent in control *tbx6-mNeonGreen$^{+/-}$;her1$^{+/-}$;her7$^{+/-}$* embryos, although they appear noisier than in *her1$^{+/+}$;her7$^{+/+}$* embryos (compare Fig. 13C with Fig. 10A « S2 – Anterior »).

Noisy pulses were observed in some traces in *tbx6-mNeonGreen$^{+/-}$;her1$^{-/-}$;her7$^{-/-}$* embryos (Fig. 13B, 14A and B). While we cannot formally rule out that some Tbx6-mNeonGreen oscillations take place in absence of *her1* and *her7*, the fact that most cells do not display such oscillations suggests that the Her1/Her7 loop is driving Tbx6 oscillations. Importantly, even if such noisy oscillations exist in some cells, the synchrony between cellular oscillations that can be appreciated in Tbx6-mNeonGreen embryos is lost in the absence of *her1* and *her7* (compare Fig. 13A and B with Fig. 10A and C). Together, these results strongly suggest that the Her1/Her7 loop either strongly couples or entrains Tbx6 oscillations during early somitogenesis, which results in waves of Tbx6 expression travelling posteriorly in the PSM.
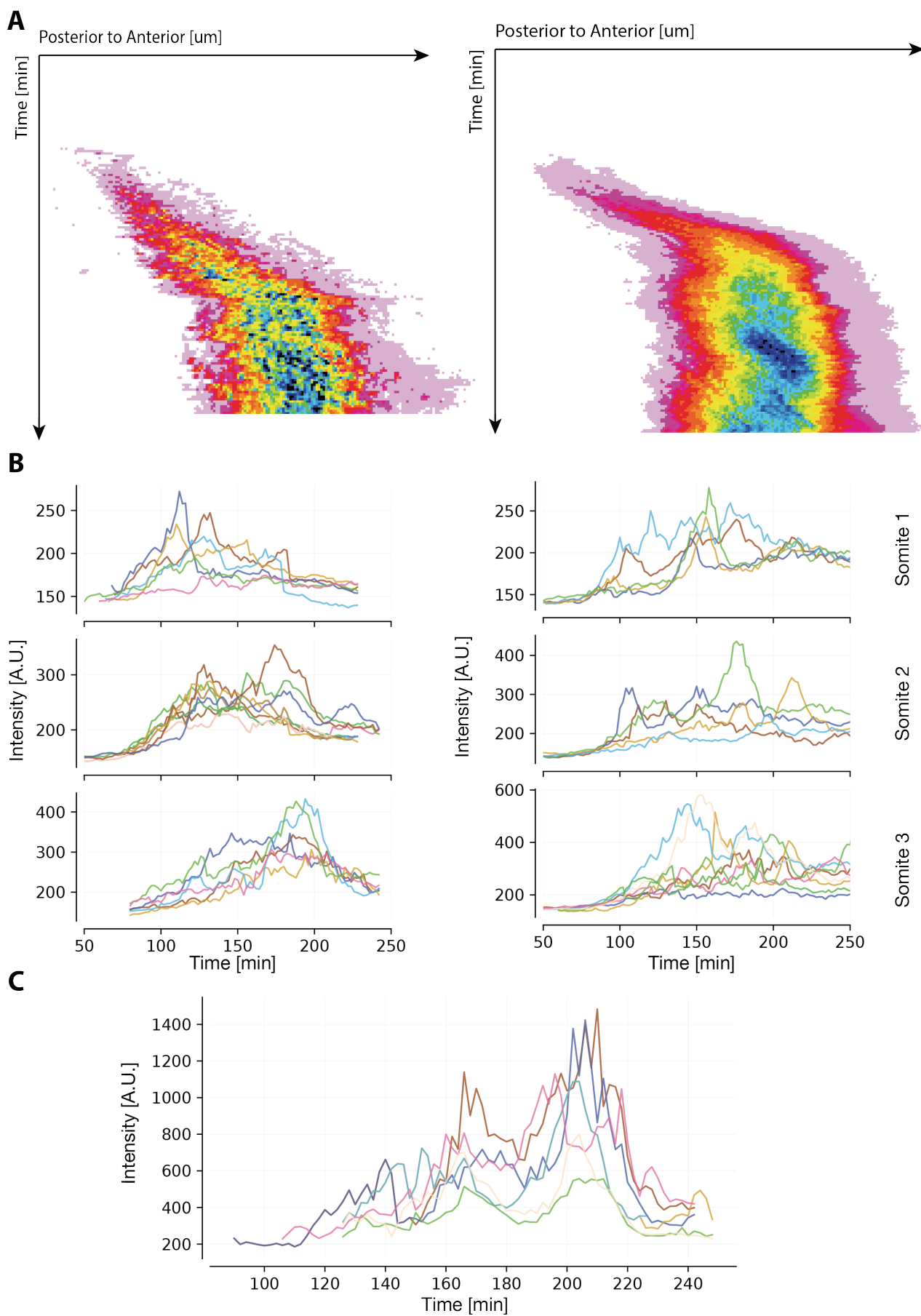
Figure 13: **Synchronous Tbx6 oscillations are abolished in *her1^-/-^;her7^-/-* embryos.** A) Kymographs from 2 representative *tbx6-mneon-green^+/-^;her1^-/-^;her7^-/-* embryos. Neither kymograph show signs of Tbx6-mNeonGreen waves. B) Tbx6-mNeonGreen traces of cells from somites 1, 2 and 3 from two representative *tbx6-mNeonGreen^+/-^;her1^-/-^;her7^-/-* embryos. C) Tbx6-mNeonGreen traces of cells from somite 2 in control *tbx6-mNeonGreen^+/-^;her1^+/-^;her7^+/-* embryos.
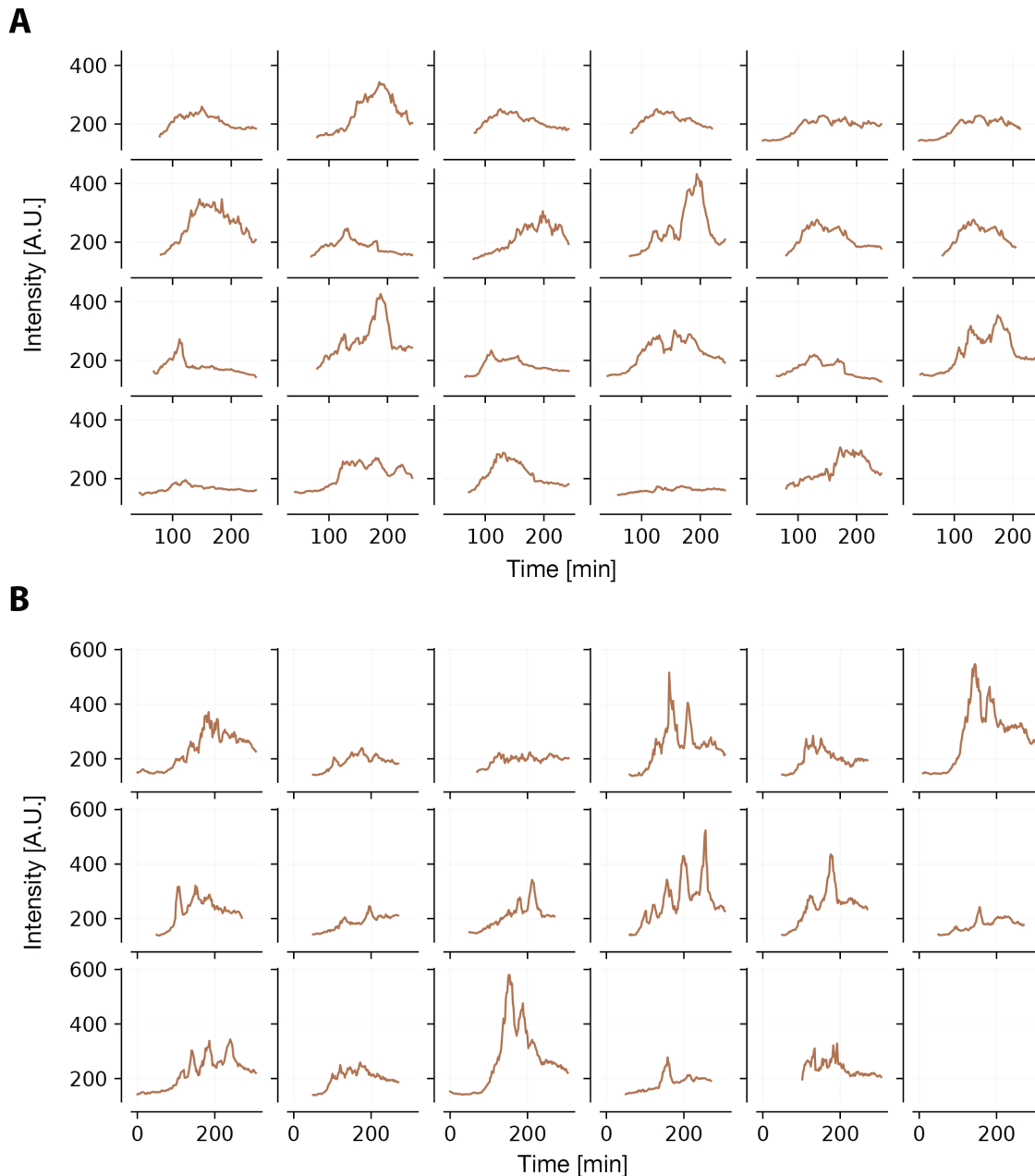
Figure 14: **Tbx6-mNeonGreen traces from Fig. 13B displayed individually.** A) Left embryo from Fig. 13B. B) Right embryo from Fig. 13B.

2.2.9 The anterior edge of the Tbx6 core domain spatially coincides with the presumptive anterior boundary of somite 1

We now address the question of the functional significance of Tbx6 waves in early somito-genesis. First, we come back to the question of how the anterior boundary of the first so-mite is prefigured. As most cells in categories « Anterior to S1 » and « S1 – Anterior » have a similar oscillatory profile, it is unlikely that the Her1 wave pattern alone defines the first boundary (compare Fig. 7A and C with Fig. 8A). However, the Tbx6 profile appears very different in cells from these two categories. Cells forming the first somite boundary display two pulses of Tbx6 while cells that are located just anteriorly to the first somite do not express Tbx6 above background (compare Fig. 10A and C. with Fig. 8B). Cells forming the first boundary express Mesp-ba-mKate2, but cells located anterior to the first boundary do

not (Fig. 7C, Fig. 10C, respectively). This is consistent with the idea that Tbx6 is required for *mesp-ba* expression in a cell-autonomous manner (Oates et al., 2005; Sawada et al., 2000). Together, these results indicate that the edge of the Tbx6 domain coincides with the location of the first presumptive somite boundary (Fig. 15A). Indeed, the edge of the Tbx6 domain is initially set when the first travelling wave of Tbx6 expression arrives in the anterior PSM during epiboly (Cycle number 2 in Fig. 9, Fig. 15A).

Figure 15: **Cells located at the anterior edge of the Tbx6 domain eventually form the first and the second presumptive boundary.**
A) Single cells were back-tracked from the anterior boundary of somite 1 ("S1 – Anterior") and from a location just anterior to the first

boundary ("Anterior to S1"). Two snapshots of a maximum-intensity projection of an elliptically transformed timelapse of Tbx6-mNeon-Green during epiboly are shown here. At this specific timepoint, cells in "S1 – Anterior" are located at the edge of the Tbx6 expression domain but cells in "Anterior to S1" are located just anteriorly to the Tbx6 domain. This suggests that the anterio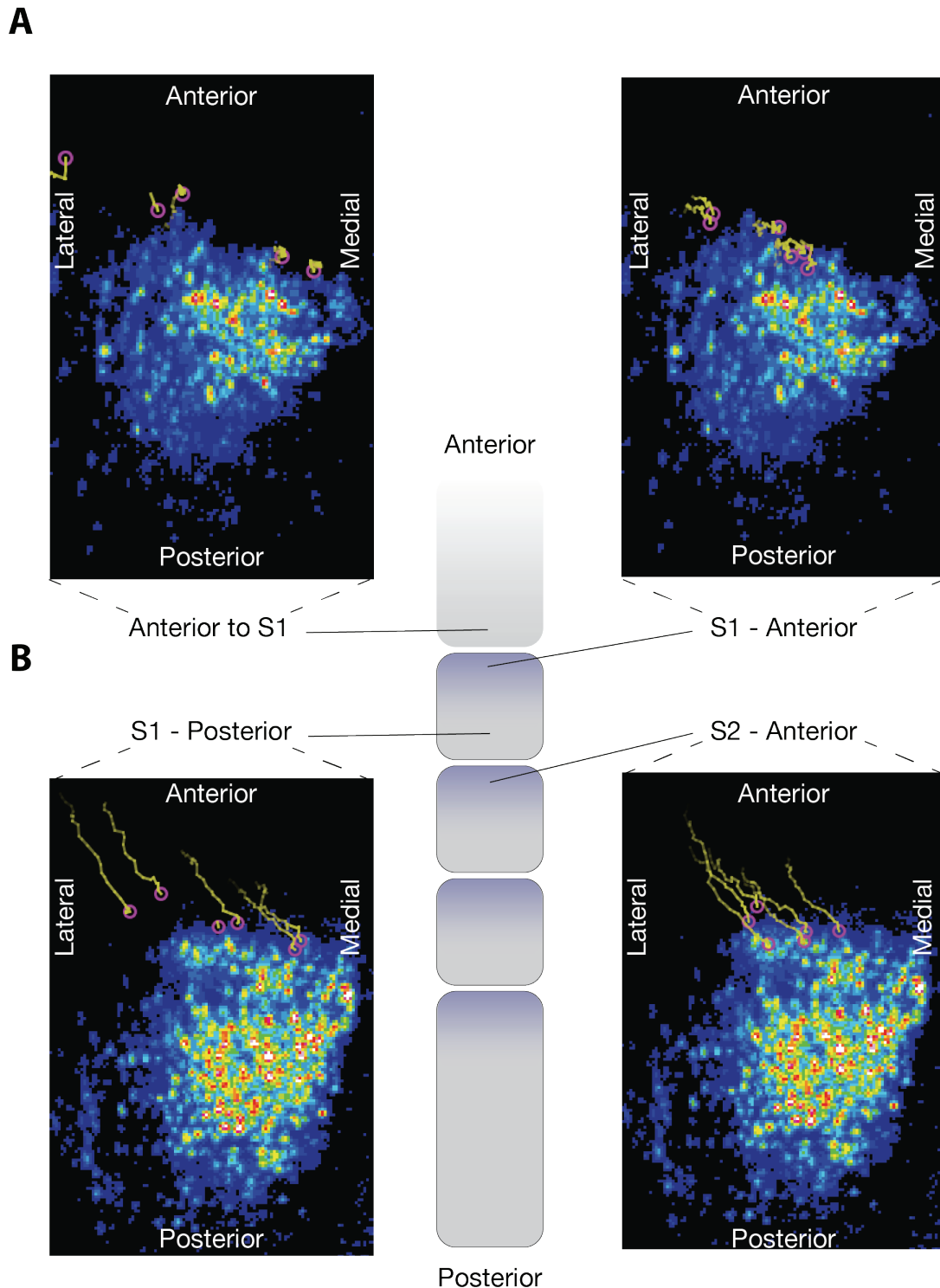r edge of the Tbx6 domain defines the first presumptive boundary. B) Single cells were back-tracked from the posterior boundary of somite 1 ("S1 – Posterior") and from the anterior boundary of somite 2 ("S2 – Anterior"). Two snapshots of a maximum-intensity projection of an elliptically transformed timelapse of Tbx6-mNeonGreen during epiboly are shown here. These snapshots show a later timepoint than in A) and therefore another wave of Tbx6 expression. At this specific timepoint, cells in "S2 – Anterior" are located at the edge of the Tbx6 expression domain but cells in "S1 - Posterior" are located just anteriorly to the Tbx6 domain. This suggests that the anterior edge of the Tbx6 domain also defines the second presumptive boundary. Note that some cells are located medially to the Tbx6 domain and will eventually be part of the somite boundary.

2.2.10 The anterior edge of the Tbx6 core domain spatially coincides with the location of the presumptive anterior boundary of somite 2

We then investigated whether the presumptive boundary of somite 2 coincided with the anterior edge of the Tbx6 core domain formed by the second wave. To do so, we compared individual traces of cells forming the posterior boundary of somite 1 (« S1 – Posterior ») with cells forming the anterior boundary of somite 2 (« S2 – Anterior »). These two categories of cells constitute the two epithelial layers of the same boundary (Fig. 16A). We also included traces from « S1 – Anterior » in our comparison, to assess the differences in Tbx6-mNeon-Green and Her1-YFP activities between cells forming the anterior versus posterior boundaries of the same somite. We pooled cells from 3 Tbx6-mNeonGreen and 3 Her1-YFP embryos and we temporally aligned the traces based on the time of epiboly completion.
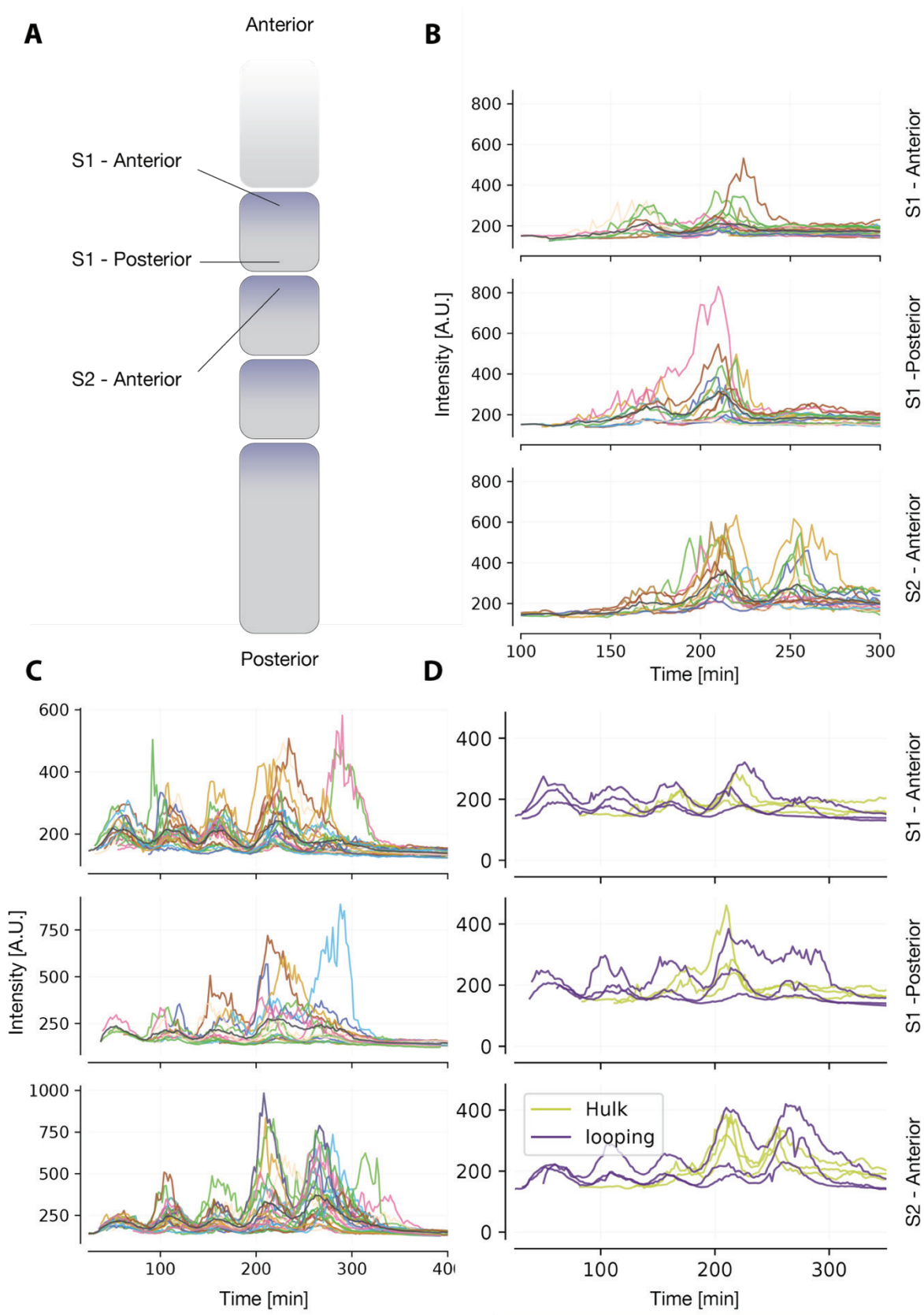
Figure 16: **The anterior edge of the Tbx6 domain coincides with the location of the second presumptive boundary.** A) Single cells were back-tracked from the anterior boundary of somite 1 ("S1 – Anterior"), the posterior boundary of somite 1 ("S1 – Posterior") and the anterior boundary of somite 2 ("S2 – Anterior"). B) Individual Tbx6-mNeonGreen traces in categories « S1 - Anterior », « S1 - Posterior» and « S2 – Anterior » are aligned temporally between 3 embryos. The mean intensity of the traces, pooled from 3 embryos, is displayed as a thick black line. C) Individual Her1-YFP traces in categories « S1 - Anterior », « S1 - Posterior » and « S2 – Anterior » are aligned temporally between 3 embryos. The mean intensity of the traces, pooled from 3 embryos, is displayed as a thick black line. D) Means of Her1-YFP (blue) and Tbx6-mNeonGreen (yellow) signals in individual embryos that are temporally aligned.

Although the amplitudes of oscillations differ slightly, the Tbx6-mNeonGreen profile is similar in cells forming the anterior and the posterior boundary of somite 1 (Fig. 16B). In contrast, cells forming the anterior boundary of somite 2 make one extra cycle (at min. 250). A similar observation can be made about Her1-YFP (Fig. 16C), except that a few cells from somite 1 also make one extra cycle (at min. 275). Comparing the average intensity per embryo between Her1-YFP (blue) and Tbx6-mNeonGreen (yellow) confirms that « S1 – Posterior » and « S2 – Anterior » cells differ in their Her1-YFP and Tbx6-mNeonGreen profiles. This suggests that the Her1-YFP wave n° 5 (Fig. 6) and the Tbx6-mNeonGreen wave n°3 (Fig. 9), which travel in the PSM at 90% epiboly, arrest at a position that coincides with the presumptive boundary demarcating somite 1 and 2 (Fig. 15B). Thus, similar to the first boundary, the position of the Tbx6 wave's arrest in the anterior PSM precisely prefigures the position of the next somite boundary.

2.3   Discussion

We time lapsed the onset of the segmentation clock in zebrafish embryos for the first time. By doing so, we characterized the first waves of Her1 expression during epiboly and we determined that the 4th, 5th and 6th Her1 kinematic waves prefigure the first, second and third somite boundary, respectively. This result provides a mapping between the wave number and the somite number. This mapping has important implications, notably to understand which kinematic wave prefigures the first defective boundary during the desynchronization of the segmentation clock. We reckon this would greatly help to understand what level of synchrony is required for the proper formation of somite boundaries. I come back to this question in the next chapter. We observed that cells located anterior to the first somite boundary also display Her1 oscillations, indicating that the first four Her1 kinematic waves do not stop at the first presumptive boundary. It is therefore unlikely that the wave pattern of the Clock alone instructs cells to form the first somite boundary.

By timelapsing Tbx6-mNeonGreen embryos during epiboly and early somitogenesis, we observed several waves of Tbx6 signal travelling anteriorly in the PSM. Immunostainings against Tbx6 showed a similar dynamical pattern of Tbx6 expression in wild type embryos. Using cell tracking, we found that Tbx6 waves are generated by cellular oscillations of Tbx6. Cells forming the anterior boundary of somite 5 also display Tbx6 oscillations but the amplitude of Tbx6 oscillations was reduced in cells forming the anterior boundary of somite 7, suggesting a smooth transition over time from an oscillatory to a non-oscillatory regime of Tbx6 expression. Of note, Tbx6 also oscillates *in vitro* in isolated cells dissociated from tailbud and posterior PSMs of embryos at bud stage, suggesting Tbx6 oscillations do not rely on Notch signaling in *trans* and are autonomous in nature.

Tbx6 oscillations that are cell-autonomous is consistent with the idea that they are generated by the known Her feedback loop, the clock of the segmentation clock. Temporally aligning Her1-YFP and Tbx6-mNeonGreen traces from multiple embryos, using the time of epiboly completion as a temporal reference, revealed that both signals oscillate in-phase in the anterior PSM. Waves of Tbx6 expression are no longer apparent in *her1*/her7 double mutants. At the cellular level, Tbx6 oscillations were found to be abolished, at least in most cells, in absence of *her1* and *her7*, suggesting that the Her1/Her7 loop drives Tbx6 oscillations. We cannot formally rule out that some noisy Tbx6 oscillations exist in some cells in

her1 ;her7 double mutants. Using classical signal processing methods, such as wavelet analysis (Mönke et al., 2020), to assess whether a signal oscillates is challenging because Tbx6-mNeonGreen traces are relatively short-lived. Therefore, it is possible that the Her1/Her7 does not drive but strongly couples Tbx6 oscillations. In any case, these results show that the Clock (Her1/Her7 loop) interacts with the Wavefront (Tbx6).

It is not clear yet whether this interaction is direct or indirect. The *tbx6* promoter contains one E-box binding site (Ban et al., 2019) and bHLH transcription factors, such as Her1 and Her7, are known to bind to E-box sites (Brend and Holley, 2009; Schröter et al., 2012). It is therefore possible that Her1 and/or Her7 bind directly to the *tbx6* promoter to regulate its transcription. Ripply proteins have been shown to turn Tbx6 protein from transcriptional activators to repressors by recruiting the transcriptional co-repressor Groucho (Kawamura et al., 2008). Groucho forms complexes with bHLH members of the Hairy-Enhancer of Split (Hes) family in *Drosophila* (Paroush, 1994) and is expressed in the PSM of zebrafish embryos (Wülbeck and Campos-Ortega, 1997). It is also possible that Her1/Her7 interact with Tbx6 via the recruitment of Groucho. Interestingly, Tbx6 has been shown to bind to the *her1* promoter (Brend and Holley, 2009). Further work is needed to investigate the molecular details of this bi-directional interaction between the Clock and the Wavefront.

What is the functional significance of this interaction? Waves of Tbx6 expression arrest at a position that prefigures the future anterior boundary of somite 1, and the future boundary demarcating somites 1 and 2. Combined immunostaining and *in situ* hybridization staining suggest that the anterior edge of the Tbx6 core domain coincides with the presumptive somite boundary also in 8-somite stage embryos (Wanglar et al., 2014), but analysis of the protein dynamics remains to be investigated in living embryos. Preliminary analysis suggests that this relationship may not hold in posterior somites. In mice, *Mesp2* is expressed at the anterior edge of the Tbx6 domain (Oginuma et al., 2008). The anterior border of the Tbx6 pattern is perturbed in embryos injected with *her1 ;*her7 double morpholinos (Wanglar et al., 2014). As somite boundaries are defective in these embryos, this result suggests that the anterior edge of the Tbx6 domain might carry a function in establishing boundaries (Wanglar et al., 2014). It also indicates that the Her1/Her7 loop still interacts with Tbx6 in embryos at 8-somite stage. Further research is required to gain deeper insight into the functional significance of Tbx6 waves. Some important questions remain. Can the spatial relationship observed between the anterior border of the Tbx6 domain and the presumptive boundaries of the first two somites be generalized to other somite boundaries during somitogenesis? If not, are somite boundaries prefigured by different mechanisms over the course of somitogenesis?

Together, our results show that the Her1/Her7 loop in required for waves of Tbx6 expression travelling anteriorly and arresting at a position prefiguring the location of the first two boundaries. Considering that Tbx6 is a key component of the Wavefront, our findings suggest that the spatial pre-pattern prefiguring the positions of the anterior-most boundaries is established by a mechanism that differs from the classical view of the Clock and Wavefront model. The co-existence of waves of Her1 and Tbx6 expression in the zebrafish PSM is reminiscent of the waves of Wnt and Notch signaling in the mouse segmentation clock (Sonnen et al., 2018).

As discussed in the introduction of this chapter, the formation of the anterior-most somites is, in many aspects, different than the formation of the posterior trunk somites and the tail somites. As the first somites form, convergence-extension movements drive the axis

elongation of the embryo. From 60% epiboly to bud stage, the length of the PSM, defined as the distance from the blastoderm margin to the location where kinematic waves stop, appears to grow (Fig. 6 and Fig. 9). That might be explained by the fact that cells in the hypoblast are convected towards the animal pole as gastrulation proceeds. In contrast, the PSM length shrinks during mid- and late-somitogenesis (Soroldoni et al., 2014). It is therefore possible that the interaction between the Clock and the Wavefront to establish the spatial pre-pattern is different for the formation of the anterior-most somites than for other somites. We can also speculate that such a difference in somite formation might reflect greater developmental constraints for anterior somites and a higher variability in the formation of posterior somites.

Chapter 3 Resynchronization of the segmentation clock[4]

3.1 Background

The segmentation clock drives the formation of somites with remarkable spatio-temporal precision and robustness. It manifests itself as waves of gene expression travelling anteriorly in the PSM. This wave pattern relies on the synchronization of cell-autonomous oscillations (Horikawa et al., 2006; Jiang et al., 2000; Riedel-Kruse et al., 2007; Tsiairis and Aulehla, 2016a). In Delta-Notch mutants that affect the synchronization of the cellular oscillators, the wave pattern is abolished and somite boundary formation is disrupted. Here, we are interested in determining what level of synchrony in the wave pattern is required for the correct formation of somite boundaries. We hope to better understand how the synchronization of the segmentation clock influences the robustness of patterning. Additionally, investigating how the segmentation clock fails to produce correct somite boundaries can provide a deeper insight into the mechanistic basis of congenital scoliosis.

Synchronization is an important concept in many fields, but it is not always intuitive to understand and predict the outcome of interactions between oscillators. Following the first proposal that Delta-Notch signaling might be the coupling mechanism that synchronizes the oscillating cells of the PSM in zebrafish (Jiang et al., 2000), mathematical models have played a prominent role in designing and interpreting experiments. These models have fallen into two basic types. In the first, the system dynamics is described in terms of concentrations and interactions of proteins of the Delta-Notch signaling system (e.g. Lewis, 2003; Horikawa et al., 2006; Uriu et al., 2009). This representation is perhaps the most straightforward to express the typical results of genetic and molecular experiments, which alter the levels and activities of distinct molecular species, and will be familiar to many biologists as a biochemical or Genetic Regulatory Network (GRN). A second type of model describes the system dynamics in terms of generic oscillator variables, such as the frequency and phase. The dynamics of an oscillator can be abstracted as a point moving on a circle. A phase, the angle θ this point makes with the horizontal axis, can be then assigned to oscillator, indicating the progression of an oscillator through a cycle. These phase models are reductions of more explicit oscillator models, such as described above, and are often analytically tractable. A famous example of phase model is the Kuramoto model (Kuramoto and Nishikawa, 1987). In this model, oscillators are all weakly coupled with each other. The phase θ of an oscillator *i* changes over time as:

$$\dot{\theta}_i = \omega_i + \frac{K}{N}\sum_{j=1}^{N}\sin\left(\theta_j - \theta_i\right), \qquad i = 1, \dots, N$$

---

[4] BAC recombineering and transgenesis have been performed by Daniele Soroldoni. Characterization of morphological segmentation has been performed by Chloé Jollivet and myself. Cell tracking has been performed by Laurel Rohde and myself.
Some material in this chapter has been adapted from (Venzin and Oates, 2020) according to the publisher's policy on authors' rights.

Where ω_i is the intrinsic frequency of an oscillator i, K is the coupling strength and N is the number of coupled oscillators in the system. A complex order parameter can be computed based on the phases of all the oscillators as:

$$re^{i\psi} = \frac{1}{N}\sum_{j=1}^{N}e^{i\theta_j}$$

The radius r represents the phase coherence, i.e. how close are the phases of the different oscillators, and the angle ψ represents the average phase (Strogatz, 2000). It is important to distinguish the level of synchrony (i.e. the phase coherence) from the level of synchronization. As we just mentioned, the level of synchrony is a measure of how close the phases of different oscillators are at any given time. In contrast, the level of synchronization is measured by the difference in frequency between different oscillators. Two oscillators are considered to be synchronized if they communicate to reach the same frequency (i.e. they are phase-locked). Therefore, two oscillators can be synchronized but not synchronous, and vice-versa.

As discussed in section 1.1, the proposed mechanism of synchronization between neighboring PSM cells relies on the transcriptional activation of Notch target genes including, among others, the clock gene *Hes7* in mouse and its homologs *her1* and *her7* in zebrafish. The first proposal to link Notch signaling and oscillations was the "desynchronization hypothesis" (Jiang et al., 2000). This hypothesis seeks to explain the characteristic somite phenotype in zebrafish Notch pathway mutant embryos, in which a small number of somites are properly formed in the anterior, followed by defective segments in the posterior. The hypothesis proposes that PSM cells start oscillating in-phase before the onset of somitogenesis, but because genetic oscillations are noisy and cells are not coupled to each other through Delta-Notch signaling in the mutants, their phases gradually become asynchronous over time. In the absence of Notch signaling, waves of gene expression visible in a snapshot of the PSM (Fig. 17A) would be gradually replaced by a salt and pepper pattern that arises from the intermingling cells in low- and high-expression states (Fig. 17B), and this pattern would be incompatible with normal segment boundary formation.

The "desynchronization hypothesis" is experimentally supported by the fact that, at developmental time points when defective segments are being formed in Delta or Notch mutants, individual cells continue to oscillate in the PSM and a salt-and-pepper pattern is observed at the tissue level (Delaune et al., 2012). Thus, although the gradual desynchronization of oscillating PSM cells described above has not been observed in mutants *in vivo*, existing evidence strongly supports the idea that Delta-Notch signaling is required in zebrafish for synchronization between oscillating PSM cells. Note that the role of Notch signaling in the mouse segmentation seems to be different than in zebrafish. In addition to its role in synchronizing cellular oscillations, Notch signaling is thought to be a core component of the mouse segmentation clock (reviewed in (Venzin and Oates, 2020)).
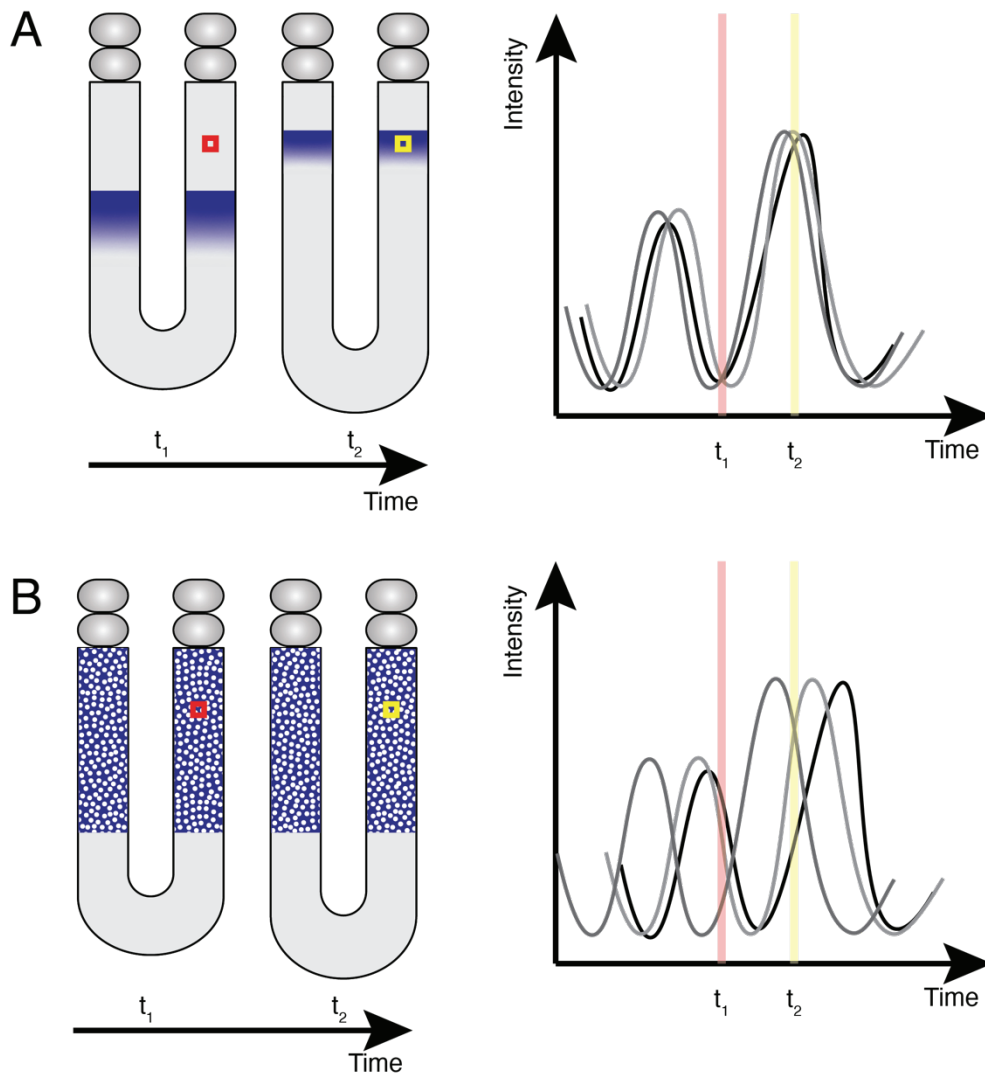
Figure 17: **Synchronization and travelling waves**. A) Snapshots of a travelling wave of gene expression (left). When the segmentation clock is synchronized, waves of gene expression spanning multiple cells travel along the PSM. At t_1, cells in the magenta box display a low level of cyclic gene expression. At t_2, the same cells now display a high level of cyclic gene expression and, along with other cells in the vicinity, comprise the stripe visible in the PSM. Oscillation time series of four individual cells from the same region of the anterior PSM (boxes) are represented on the graph (right). The magenta, respectively yellow, region on the graph corresponds to the timepoint t_1, respectively t_2. B) Loss of Notch signaling results in a desynchronized segmentation clock. Because neighboring cells no longer oscillate in synchrony, the stripe pattern is replaced by a salt-and-pepper pattern of gene expression.

Drugs blocking Notch signaling, like DAPT, can desynchronize the segmentation clock, mimicking Notch mutants (Fig. 18C, D) (Horikawa et al., 2006; Riedel-Kruse et al., 2007; Tsiairis and Aulehla, 2016b). It is thought that when the phase coherence of the segmentation clock falls under a critical threshold Z_c, defective somite boundaries start to form (Fig. 18)(Jiang et al., 2000; Riedel-Kruse et al., 2007). The number of first, and thus anteriormost, defective segment is termed the anterior limit of defects (ALD).

Upon drug washout, the segmentation clock resynchronizes and, it is assumed that once the phase coherence of the segmentation clock is higher than Z_c, normal segments form again (Fig. 18E, F) (Riedel-Kruse et al., 2007; Uriu et al., 2021). The first segment that forms normally during the resynchronization is called the first recovered segment (FRS). It was recently observed, in embryos treated with DAPT from 4 hpf (before the onset of the segmentation clock) to 9.5 hpf (bud stage), that defective segments formed posteriorly to the FRS (Uriu et al., 2021), giving rise to a region along the anterior-posterior (AP) axis where

normal and defective segments were intermingled (Fig. 18G, H). We call this region "the intermingled region". The observation of intermingled normal and defective segments along the AP axis is not consistent with a monotonic increase in the phase coherence upon DAPT washout and suggests that the phase coherence fluctuates around the threshold Z_c during the formation of these somite boundaries. However, large fluctuations of the phase coherence are not expected to happen once a population of oscillators is synchronized. By creating a physical model of the PSM, Uriu and colleagues found that the advection of persistent phase vortices of oscillators could theoretically explain the fluctuations in the phase coherence and consequently the formation of intermingled normal and defective segments during the resynchronization of the segmentation clock (Uriu et al., 2021). In contrast to normal waves of gene expression travelling linearly along the long axis of the PSM, phase vortices exhibit a *rotation* of the phase pattern along an axis.
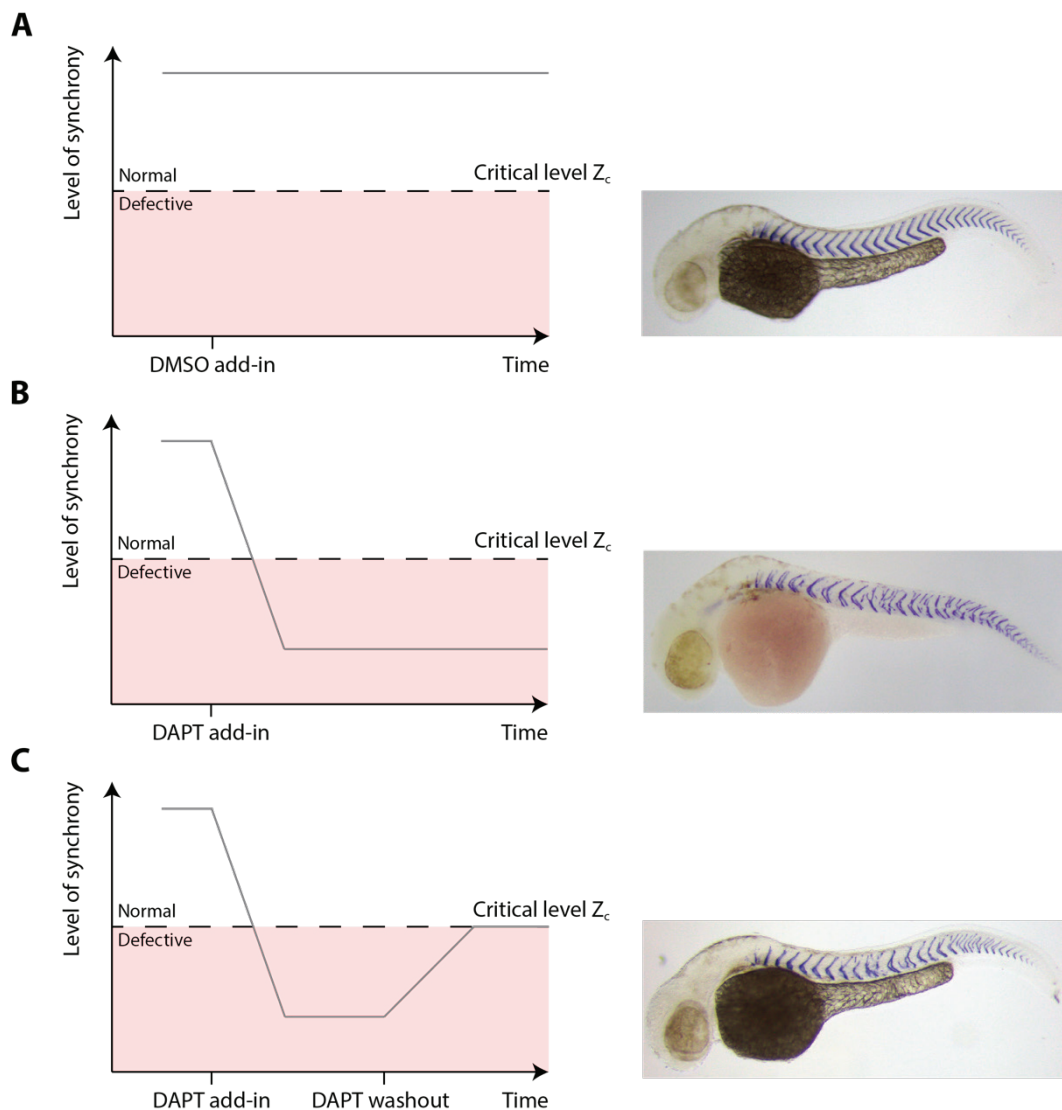
Figure 18: **Segment boundaries (visualized with *in situ* hybridization for *xirp2a)* in embryos treated with DMSO and DAPT.** A) DMSO-treated. B) DAPT treatment, no washout. C) DAPT treatment from 4.5 to 9.5 hpf.

Determining what level of synchrony is required for the correct formation of somite boundaries essentially corresponds to finding the critical phase coherence Z_c under which defective somite boundaries start to form. This can be done during the desynchronization (Fig.

18B) and the resynchronization of the segmentation clock (Fig. 18C). Addressing this question during the resynchronization of the segmentation clock also allows us to investigate whether we can experimentally observe the phase vortices that were predicted to travel in the PSM and to cause intermingled defects in somite boundaries (Uriu et al., 2021). We addressed both questions by back-tracking cells forming defective boundaries located in the "intermingled region" of DAPT-treated embryos. Note that I consider the current state of this research as preliminary and more samples are needed to confirm some of the results.

3.2   Results

3.2.1   Characterization of *Hoff,* a new transgene for *her1*

The first Her1 transgene generated in our lab, *Looping (Tg(her1::Venus))*, has contributed to improve our understanding of the zebrafish segmentation clock over the past few years (Rohde et al., 2021; Soroldoni et al., 2014). However, this transgene comes with limitations reported in the original paper (Soroldoni et al., 2014). Some minor, sporadic segment defects were reported in 47% of *Looping* embryos. The somitogenesis period in *Looping* embryos is 10% slower than in their wildtype (WT) siblings. The expression pattern of the reporter mRNA *venus* is striped, as the *her1* expression pattern in WT embryos, but these stripes are fuzzier than stripes of *her1* expression in WT (Soroldoni et al., 2014). Since the stripe pattern is not as sharp as in WT embryos, *Looping* is not the ideal transgene to study the synchronization of the segmentation clock

Here, we introduce our new *her1* transgene *Hoff.* While the construct of *Looping* contained the shared promoter and the coding regions of both *her1* and *her7*, the coding region of *her7* has been replaced by the fluorophore mKate2 attached to a nuclear localization signal (NLS) in the *Hoff* construct (Fig. 19A). The expression pattern of *her1* in Hoff embryos mimics the WT pattern and stripes of *her1* expression are reasonably sharp (Fig. 19B). The somitogenesis period was found to be 6% longer in *Hoff* embryos than in their wildtype siblings (Fig. 19C, E). No segment defects were detected in *Hoff* embryos (n = 15) (Fig. 19D). On average, the 17th segment aligns with the proctodeum, which is used as a fiducial marker to compare the number of somites formed in different embryos. This confirms that the somitogenesis period of *Hoff* embryos is slighter higher than WT embryos where the 18th segment aligns with the proctodeum, on average. As a comparison, the 15th segment aligns with the proctodeum in *Looping* embryos on average (Soroldoni et al., 2014). The presence of the *Hoff* transgene in *her1*^{-/-};*her7*^{-/-} double mutants was sufficient to rescue the double mutant phenotype (all segments are defective) to a *her7*^{-/-} phenotype (the first 7-8 segment form normally, posterior segments are defective). This suggests that Her1-mNeonGreen (hereafter Her1-mNG) is functional (Fig. 19F).

With a *her1* expression pattern very similar to WT and an absence of segment defects, *Hoff* is a suitable transgene to study *her1* dynamics in the segmentation clock. The main limitation of this transgene is that comes with a mKate2-NLS as a nuclear marker and therefore does not offer the possibility to image other transgenes with a red reporter. In addition, DAPT treatments were found to reduce the levels of mKate2-NLS fluorescence. This is probably due to the fact that the mKate-NLS expression is driven by the *her7* promoter and that the Notch intra-cellular domain is thought to activate *her1/her7* expression by binding

to their shared promoter (Brend and Holley, 2009; Oates and Ho, 2002; Sieger et al., 2003; Takke and Campos-Ortega, 1999). While the mKate2-NLS nuclear signal is bright enough for subsequent analysis in DAPT-treated embryos, it can be made brighter by crossing *Tg(hoff)* with *Tg(h2b-mcherry)*. To facilitate cell-tracking during the analysis, we imaged embryos that expressed both *Hoff* and *H2B-mCherry*. For the sake of clarity, we will refer to the genotype of *Hoff* embryos simply as *her1-mneongreen* and to the Hoff signal as Her1-mNG.
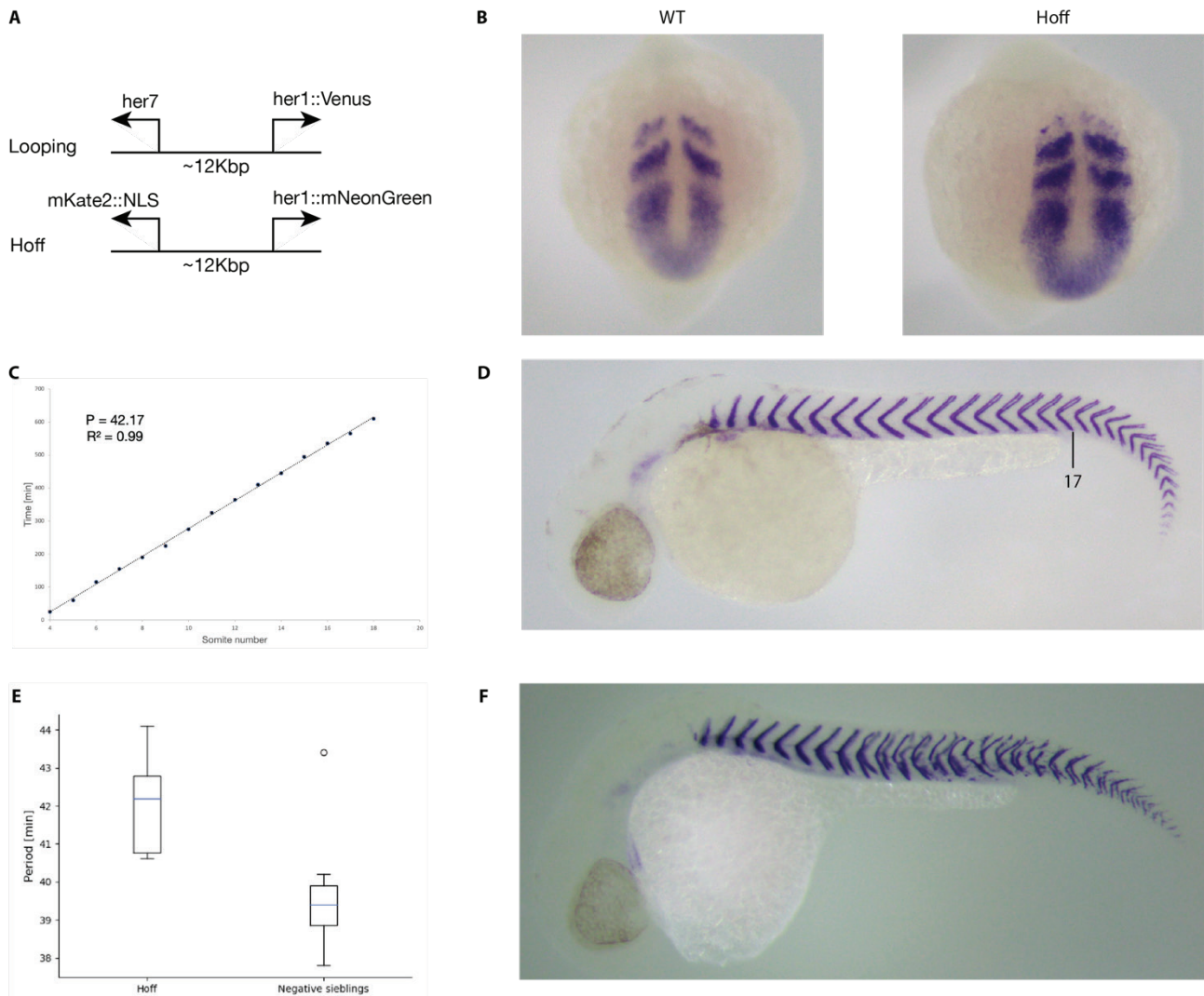

Figure 19: **Characterization of morphological segmentation in *Hoff*, a new transgene for *her1*.** A) Comparison between the new transgene construct *Hoff* and the previous state-of-the-art construct *Looping*. B) *In situ* hybridization against *her1* in representative WT and *Hoff* embryos. C) Somitogenesis period for somites 4 to 18. Somite boundaries is scored visually from a widefield timelapse. For each embryo, the somitogenesis period is calculated from a linear regression (n = 9 embryos). D) *In situ* hybridization against *xirp2a*, which marks segment boundaries, in a *Hoff* embryo. No somite defects were detected. The proctodeum is used as a fiducial marker to compare the number of somites in *Hoff*, *Looping* and their negative siblings (WT). On average, 17 boundaries are counted at the proctodeum in *Hoff* versus 18 in negative siblings, indicating a slightly higher segmentation period in *Hoff* embryos. E) Box-plot of *Hoff* (n = 9) and negative siblings (n = 11). The mean period is 42.1 min in *Hoff* and 39.6 min in negative siblings. The somitogenesis period in *Hoff* embryos is therefore 6% higher than in WT. F) *In situ* hybridization against *xirp2a* in a *Hoff*^{+/-}*;her1*^{-/-}*;her7*^{-/-} embryo, which displays a *her7*^{-/-} phenotype, indicating that *her1::mneongreen* can rescue the *her1*^{-/-}*;her7*^{-/-} phenotype to a *her7*^{-/-} phenotype. This shows that Her1-mNG is functional.

3.2.2 The dynamics of the resynchronization of the segmentation clock is different in *her1-mneongreen* embryos than in wildtype

Before imaging the resynchronization of the segmentation clock, we tested whether the presence of exogenous *her1-mneongreen* copies could affect the outcome of the resynchronization assay. Using *in situ* hybridization for *xirp2a*, we scored segment boundaries in wildtype (WT) and in Her1-mNG-positive embryos treated with 50 μM DAPT from 4.5 to 9.5 hpf. The distribution of segmentation defects was different in WT than in Her1-mNG embryos (Fig. 20A). Compared to WT, defects were overall less frequent, and the range of defects was narrower in Her1-mNG-positive embryos. The mean number of defective segments per embryo was higher in WT than in Her1-mNG-positive embryos. We compared the ALD between these two conditions and found that the ALD was lower in WT than in *her1-mneongreen* embryos (Fig. 20C).
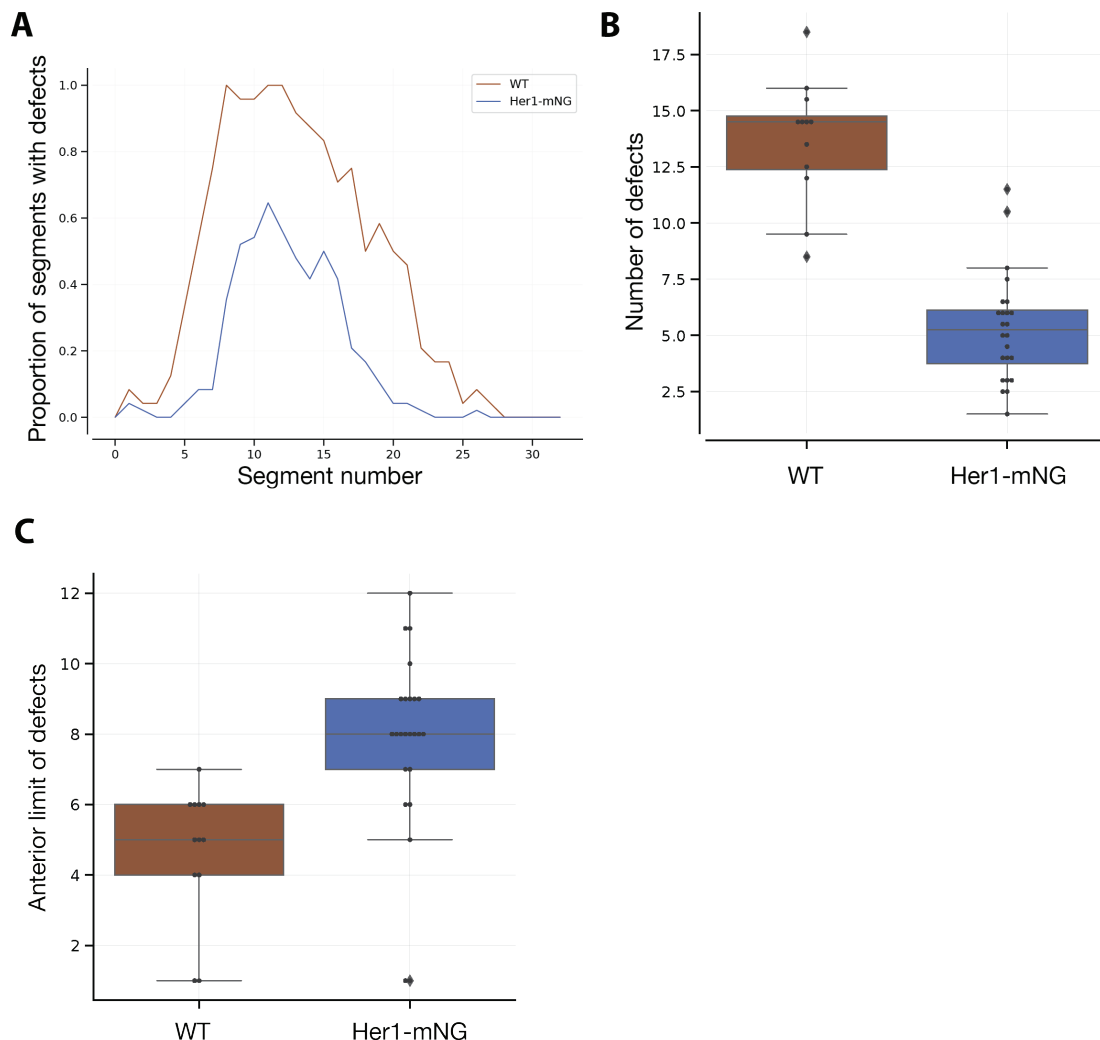
Figure 20: **The DAPT washout resynchronization assay leads to different segmentation phenotype in wildtype and *her1-mneongreen* embryos.** A) Proportion of segments with defects by segment number in wild type and Her1-mNG-positive embryos treated with 50 μM DAPT from 4.5 to 9.5 hpf (n = 24 Her1-mNG-positive embryos, n = 12 wild type (WT) embryos. Left and right sides are scored and included in the analysis. N = 2 independent experiments). Defects are overall less frequent, and the range of defects is smaller, in Her1-mNG-positive embryos than in WT. B) Comparison between the mean number of defective segments per embryos between WT and Her1-mNG-positive embryos. C) The number of the anterior-most defective segment, termed the anterior limit of defects (ALD), is lower in WT than in Her1-mNG-positive embryos.

Overall, these results suggest that, in presence of the *her1-mneongreen* transgene, the ALD is shifted posteriorly and the FRS is shifted anteriorly, leading to a narrower range of defective segments.

Note that the *her1-mneongreen* transgene contains an unknown number of *her1-mneongreen* copies. Indeed, transgenesis with I-SceI Meganuclease ensures only one insertion site of the transgene in the genome of injected embryos, but the number of inserted copies at the insertion site can vary between different founders (Liao et al., 2017). It is possible that cell-autonomous oscillations are less sensitive to transcriptional noise because of the additional, functional copies of *her1-mneongreen.* Cellular oscillators would then drift out of synchrony more slowly than in WT. This hypothesis can explain the posterior shift of ALD observed in Her1-mNG-positive embryos. Another hypothesis is that the additional *her1-mneongreen* copies provide more binding sites for the Notch Intracellular Domain to activate the *her1* expression. Therefore, the effective coupling strength would be higher, allowing the segmentation clock to resynchronize faster in Her1-mNG-positive embryos upon DAPT washout. These two hypotheses are not mutually exclusive.

In any case, there is no obvious reason to assume that the presence of the *her1-mneongreen* transgene would affect the synchrony level of the segmentation clock that is required for proper somite formation. Furthermore, there is currently no mapping of synchrony level to boundary formation in any context. Therefore, although the range of segment defects is different in Her1-mNG-position embryos than in WT embryos, we can still use our new transgenics to compare the level of synchrony between normal and defective segments. Importantly, we observed the reported region of intermingled normal and defective boundaries (Uriu et al., 2021) in 21 out of 24 DAPT-treated *her1-mneongreen* embryos. As a control, we confirmed that segment boundaries formed normally in *her1-mneongreen* embryos treated with 0.5% DMSO (Fig. 20B and C, no defect in 30 DMSO-treated embryos from 3 experiments).
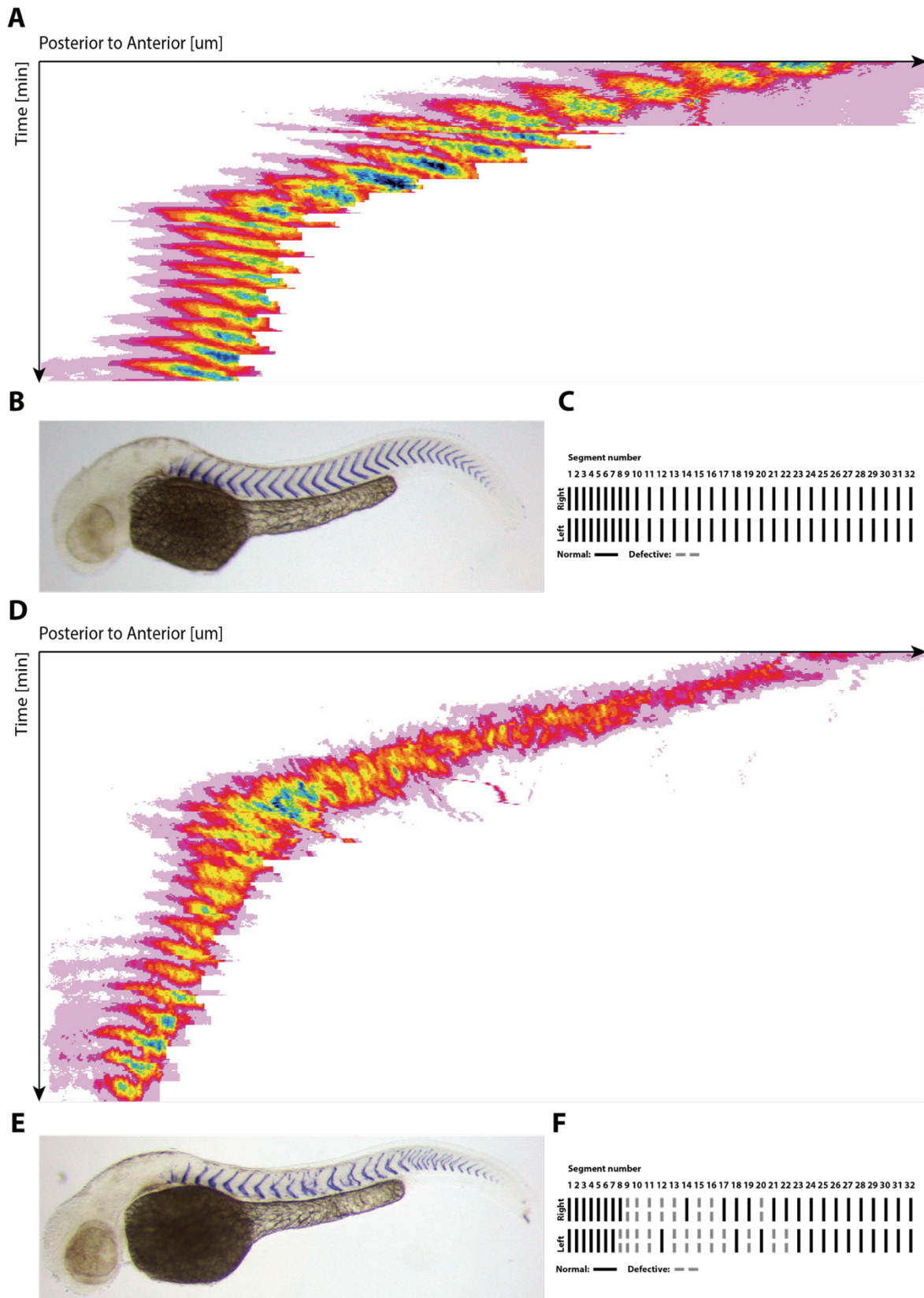
Figure 21: **Dynamics of the resynchronization of the segmentation clock.** A) Kymograph of the maximum-intensity projection of the right PSM of a representative DMSO-treated embryo. B) Brightfield picture of the same embryo in A stained by *in situ* hybridization for *xirp2a*. C) Binary scoring of segment boundaries by visual inspection of the *in situ* hybridization staining for *xirp2a*. Segment boundaries were scored as either normal or defective based on criteria listed in Materials and Methods. No defects were found in 30 DMSO-treated embryos from 3 independent experiments. D) Kymograph of the maximum-intensity projection of the right PSM of a representative, DAPT-treated embryo. Note that kymographs in A) and D) have different settings for brightness and contrast for better visualization of the Her1-mNG dynamics. E) Brightfield picture of the same embryo in D stained by *in situ* hybridization for *xirp2a*. F) Binary scoring of segment boundaries by visual inspection of the *in situ* hybridization staining for *xirp2a*. Segment boundaries are scored as either normal or defective based on criteria listed in Materials and Methods.

3.2.3 Her1-mNG dynamics during the resynchronization of the segmentation clock

Her1-mNG-positive embryos were treated with 50 μM DAPT, or 0.5% DMSO for control embryos, from 4.5 to 9.5 hpf. DAPT- and DMSO-treated embryos were timelapsed with lightsheet microscopy from around 6-somite stage in 0.02% tricaine. Movie 6 and Movie 7 show the maximum intensity projection of representative DAPT- and DMSO-treated embryos, respectively. Since the dynamics of the resynchronization of the segmentation clock might not be symmetric between the left and the right sides of the embryo, only one side of the PSM was included in the maximum intensity projection (details in Materials and Methods). In DMSO-treated embryos, waves of Her1-mNG signal travelled anteriorly in the PSM, as expected (Fig. 21A). In DAPT-treated embryos, the Her1-mNG signal was initially disordered but the wave pattern slowly came back as the segmentation clock resynchronizes (Fig. 21D).

3.2.4 Qualitative mapping between somite and segment boundaries.

After the timelapse, embryos were fixed and stained for *xirp2a* using *in situ* hybridization to assess the integrity of their segment boundaries. Segment boundaries were scored as either normal or defective based on criteria listed in Materials and Methods. The scoring of segments based on the *xirp2a in situ* hybridization staining confirmed that timelapsed embryos display the expected phenotype of the DAPT washout resynchronization assay.

With this information in hand, I elaborate the two main goals of this chapter more precisely: to compute the phase coherence in the oscillatory traces of cells that end up making a defective segment boundary and to look for potential phase vortices in this cell population. Both goals rely on finding a defective somite boundary located in the "intermingled region" and back-tracking cells forming this boundary to look at their Her1-mNG traces. Note that use the term « segment boundary » to define the boundary, marked by the expression of *xirp2a*, between morphological segments during pharyngula period. We call « somite boundary », the boundary formed by the posterior epithelial layer of one somite and the anterior epithelial layer of the next somite during somitogenesis. We can easily find defective boundaries located in the "intermingled region" by scoring segment boundaries from the *xirp2a in situ* hybridization staining. Can we find the corresponding somite boundaries in the timelapses? In other words, can we map the somite boundaries from timelapses with segment boundaries from *xirp2a in situ* hybridization staining?

Is it possible to distinguish normal from defective somite boundaries in timelapses? Using the nuclear markers (mKate2-NLS and H2B-mCherry), we assessed the integrity of somite boundaries in timelapses. When a normal boundary forms, nuclei spatially rearrange on both sides of the boundary and form a characteristic cleft (Fig. 22A)(Falk et al., 2022). We found that the spatial arrangement of nuclei was disrupted in somite boundaries with severe defects (Fig. 22D). Somite boundaries can therefore be scored by visually assessing the arrangement of nuclei with scoring criteria that are listed in Materials and Methods. However, scoring somite boundaries based on nuclei spatial arrangement has some limitations. The scoring is limited to somite boundaries that are in the field of view during the timelapse. As the anterior-most boundary is not always in the field of view of the timelapse, there is some uncertainty about the exact identity of somite boundaries. In addition, the scoring of

somite boundaries can sometimes be ambiguous, probably in the case of mild defects. To account for that, we scored somite boundary as normal, defective or ambiguous (Fig. 22B). Despite these challenges, we found that the scoring patterns of somite and segment boundaries were globally matching (Fig. 22B). Indeed, the distinctive intermingled defects yielded unique spatial patterns that aided the matching process.

By aligning the scoring pattern of somite boundaries from timelapses with the scoring pattern of segment boundaries from the *in situ* hybridization staining for *xirp2a*, we obtained a preliminary mapping between somite and segment boundaries. This mapping allowed us to qualitatively compare the shape and the location of defects in somite and segment boundaries. Defects in segment boundaries located in the region of intermingled normal and defective segments were found to be usually restricted to a specific location of the boundary (Fig. 22C). Note that both left and right sides of the embryo are visible on this brightfield image due to the high depth of field of the stereoscope. Therefore, we did not score segment boundaries from images. Instead, we scored segment boundaries directly on the stereoscope where we can visually distinguish the left and the right sides of the embryo. In this figure, we marked three segment boundaries from the left side of the embryo (18, 19 and 20). Boundary 18 is mildly disrupted on its dorsal side. The ventral part of boundary 19 is missing in the *in situ* hybridization for *xirp2a* (Fig. 22C). Boundary 20 appears normal. When we compare the corresponding somite boundaries of the same embryo in the timelapse, we found that the shape and the location of defects were similar (Fig. 22D). The ventral side of somite boundary 18 formed correctly, but the spatial organization of nuclei is a bit disordered on the dorsal side. More strikingly, somites 19 and 20 appeared to be fused ventrally but a partial boundary formed on the dorsal side (Fig. 22D, boundary 19). This defect in somite boundary qualitatively matches the defect observed in the segment boundary 19 (Fig. 22C). Thus, using the scoring patterns between somite and segment defects, and the qualitative matching between defects, we could map for the first time the correspondence between live somite defects and permanent segment boundary defects from the same embryo, and do this with cellular resolution.
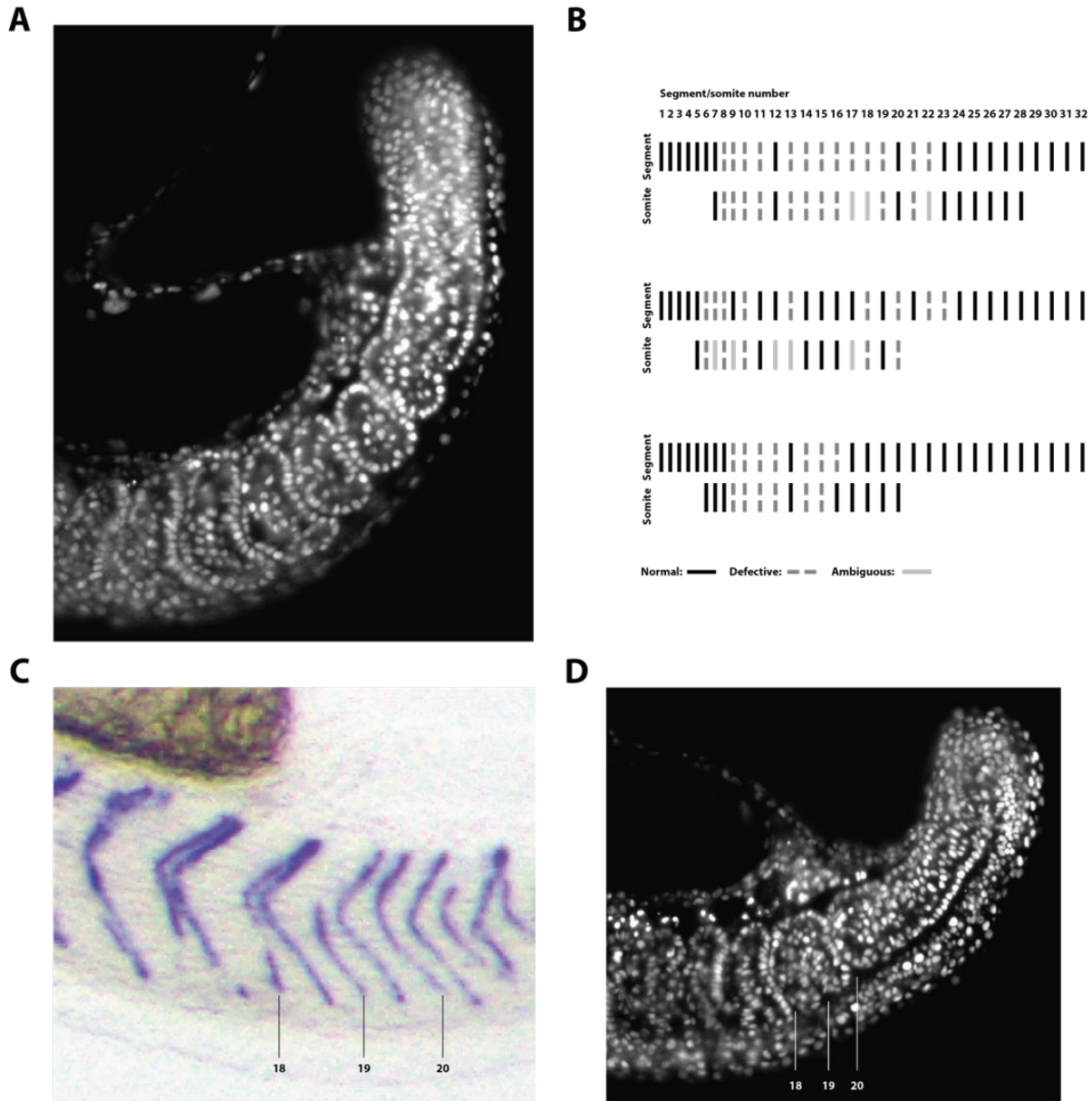
Figure 22: **Mapping between somite and segment boundaries.** A) Single z-slice of the nuclear marker mKate2-NLS from a DMSO-treated embryo. Nuclei align on both sides of boundaries and form a characteristic cleft. B) Binary scoring of segment (from Fig. 21F) and somite boundaries of the left side of the DAPT-treated embryo from Fig. 20. Somite boundaries are scored by visually assessing the alignment of nuclei from the mKate2-NLS channel of timelapses. The scoring criteria are listed in Materials and Methods. Despite some ambiguous boundaries, the general scoring patterns of segment and somite boundaries were found to be matching. It is therefore possible to map the segment boundaries from *in situ* hybridization staining for *xirp2a* with the somite boundaries from the timelapses. C) Zoom on the *in situ* hybridization staining for *xirp2a* from Fig. 21E (reflected horizontally). Left and right sides of the embryo are both visible on this image due to the high depth of field of the stereoscope. Three segment boundaries (18, 19 and 20) from the left side of the embryo are marked with lines. The ventral part of the boundary 19 is missing on the *in situ* hybridization staining for *xirp2a*. The boundary 20 is normal. D) Single z-slice of the nuclear marker mKate2-NLS from the same DAPT-treated embryos as in B) and C). In the boundary 19, the cleft between nuclei is restricted to the dorsal side of the boundary. This qualitatively matches the *in situ* hybridization staining for *xirp2a* where the ventral part of the boundary is missing.

3.2.5 Oscillatory traces of cells back-tracked from defective somite boundaries appear asynchronous

We back-tracked cells forming the posterior and anterior epithelial layers of normal somite boundaries in DMSO-treated embryos using the Mastodon plugin in Fiji (cite) (Fig. 23). As expected, Her1-mNG oscillations appeared synchronous (Fig. 23 C). We selected severe,

unambiguous boundary defects located in the "intermingled region" in DAPT-treated embryos and we back-tracked cells forming the posterior and anterior epithelial layers of these boundaries (Fig. 24). Her1-mNG oscillations appeared more asynchronous than in DMSO-treated embryos (Fig. 24B). As these cells were back-tracked from somite boundaries located in the "intermingled region", at least one correct boundary had already formed by the time these cells are forming the somite boundary. This means that the level of synchrony of the segmentation clock had previously crossed the Z_c threshold.

The wave pattern prefiguring somite boundaries that form correctly in DMSO-treated embryos might have a level of synchrony that is far above the Z_c threshold. To answer the question of what level of synchrony is required for the correct formation of somite boundary, we included a normal somite boundary that was located in the "intermingled region", as we expect the level of synchrony in the cell populations that forms this boundary to be just above the Z_c threshold. Additional normal boundaries located in the "intermingled region" will be included in our analysis in the near future. Cells forming the posterior and anterior epithelial layers of normal somite boundaries in DAPT-treated embryos show oscillatory traces that appear less coherent than oscillatory traces in DMSO-treated embryos, but more coherent than oscillatory traces of cells back-tracked from defective boundaries (Fig. 25).

Figure 23: **Oscillatory traces from normal boundaries in 2 DMSO-treated embryos**. A) Cells were back-tracked from the two epithelial layers forming a somite boundary. B) Snapshot (single-slice) of a somite boundary in a DMSO-treated embryo. Circles show cells in that z-slice that are selected for tracking. C) Her1-mNG traces of cells back-tracked from both sides (posterior and anterior) of a somite boundary in two DMSO-treated embryos (n = 20 and 37 cells).
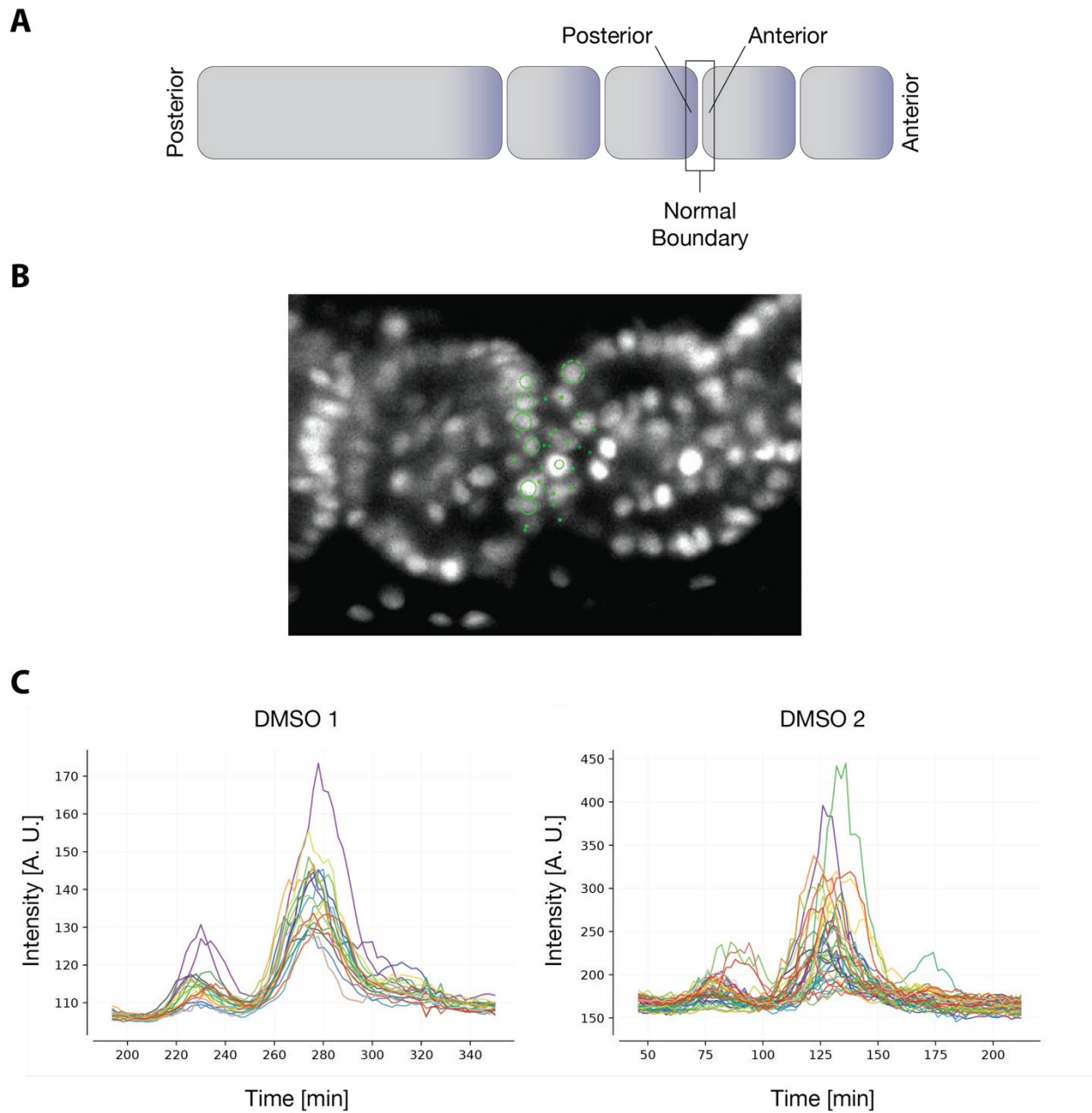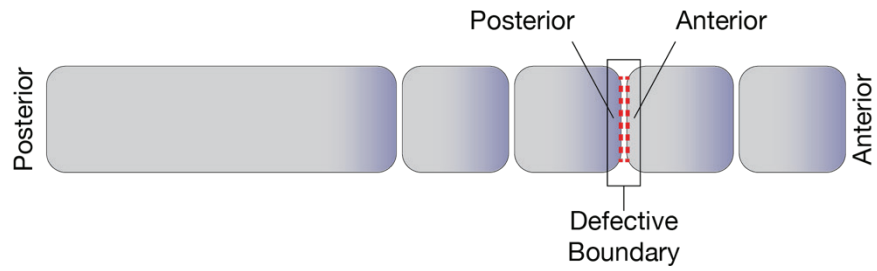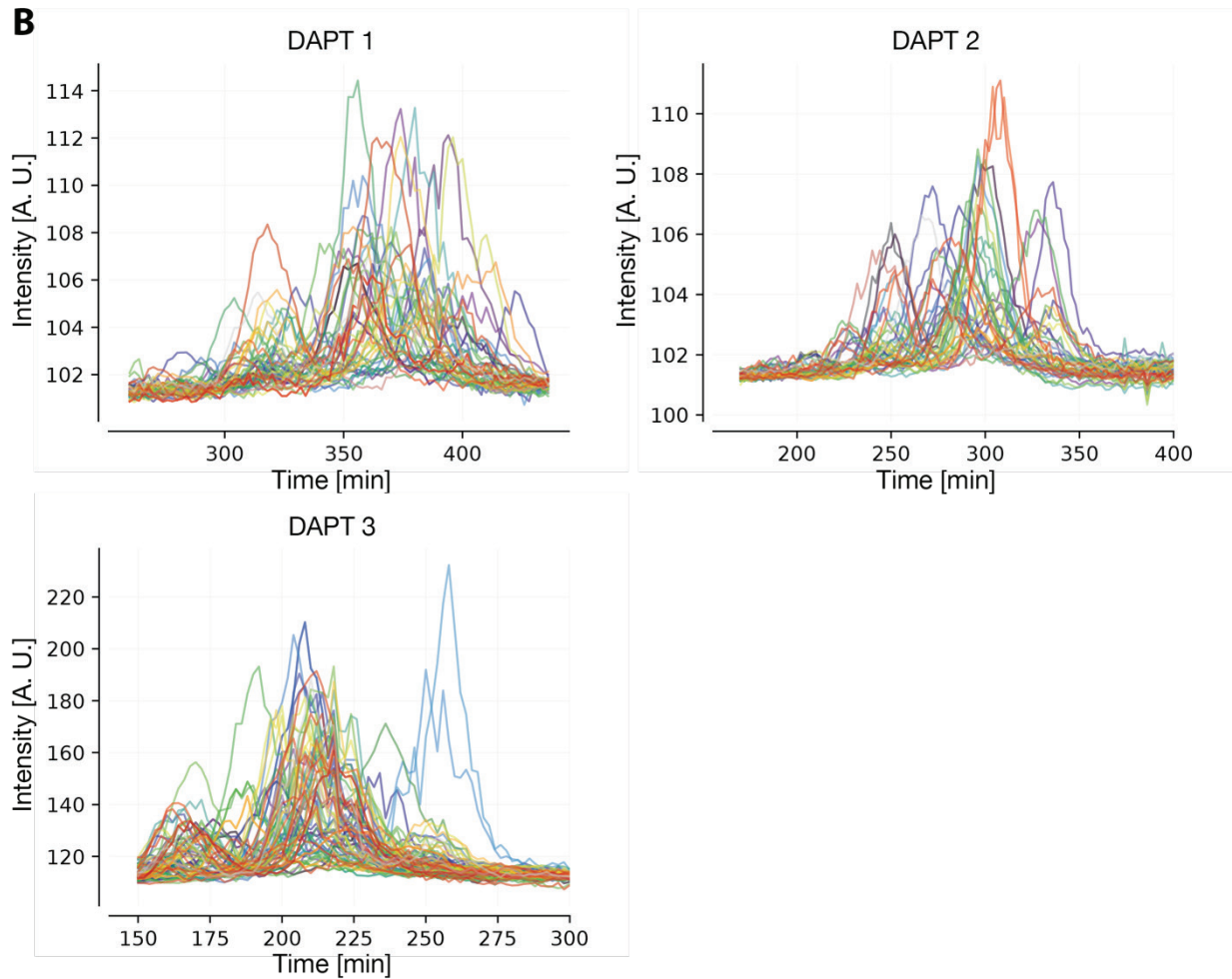
Figure 24: **Oscillatory traces from defective boundaries in 3 DAPT-treated embryos**. A) Cells were back-tracked from the two epithelial layers forming a defective somite boundary. B) Her1-mNG traces of cells back-tracked from both sides (posterior and anterior) of defective somite boundaries located in the "intermingled regions" of 3 DAPT-treated embryos (n = 47, 48 and 74 cells).

A

B
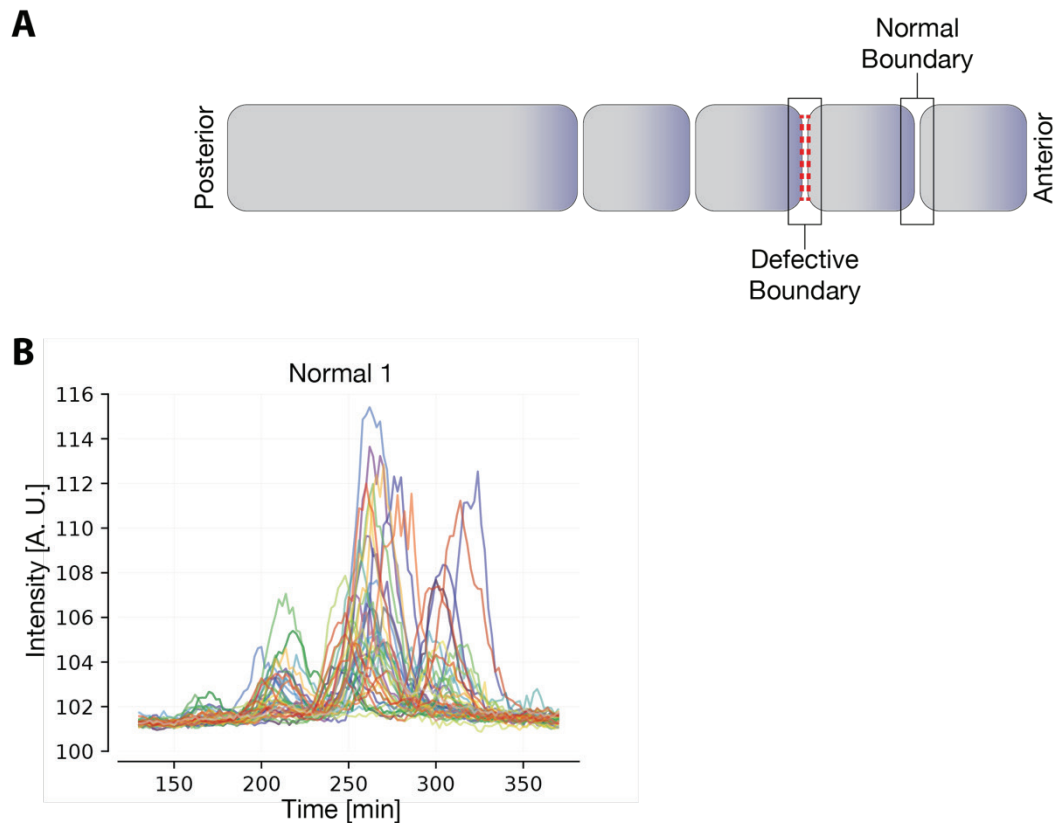
Figure 25: **Oscillatory traces of cells back-tracked from a normal boundary in a DAPT-treated embryo**. A) Cells were back-tracked from the two epithelial layers forming a normal somite boundary that is located in the "intermingled region" of the DAPT-treated embryo "DAPT 2". B) Her1-mNG traces of cells back-tracked from both sides (posterior and anterior) of a normal somite boundary located in the "intermingled regions" of the DAPT-treated embryo "DAPT 2" (n = 40 cells).

3.2.6 The global phase coherence is higher in cell populations forming normal boundaries than in cell populations forming defective ones

To quantify the phase coherence of the cell populations forming normal ("DMSO 1" "DMSO 2" and "DAPT 2 – Normal boundary") or defective boundaries ("DAPT 1", "DAPT 2" and "DAPT 3"), we need to obtain the phase of Her1-mNG oscillations. Using wavelet analysis (Mönke et al., 2020) (parameters and details in Materials and Methods), we computed the phase of the Her1-mNG time traces from DMSO-treated embryos (Fig. 26). Using the same parameters, we computed the phase of Her1-mNG oscillations in DAPT-treated embryos (Fig. 27). The phase of Her1-mNG traces could be successfully computed using wavelet analysis. However, as shown by grey stars in Fig. 27, the method also returned a phase estimate after the arrest of Her1-mNG oscillations. Therefore, we restricted our phase analysis to time windows where most cells were oscillating. As the amplitude of Her1-mNG oscillations tend to increase before the arrest of oscillations (Rohde et al., 2021), we used

the maximum value of the mean of the Her1-mNG signal to define the time at which cells completed their last peak of Her1-mNG on average.
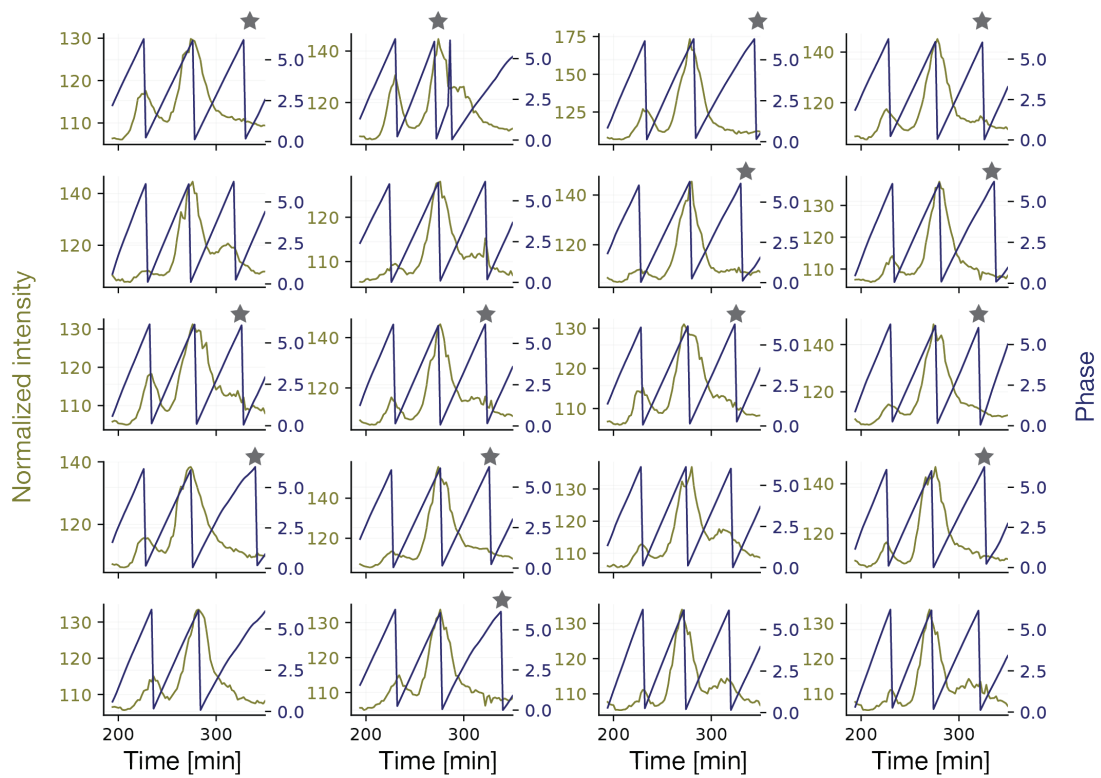
Figure 26: **Comparison between the normalized intensity of Her1-mNG time traces in representative cells from DMSO-treated embryos (green) and their phase (blue) obtained with pyBOAT** (Mönke et al., 2020). The phase of oscillations ranges from 0 to 2π. The phase is defined as 0 or 2π at the peaks of oscillations and π at the troughs. Grey stars show when a phase of $0/2\pi$ does not visually correspond to a peak in Her1-mNG traces.

Figure 27: **Comparison between the normalized intensity of Her1-mNG time traces in representative cells from DAPT-treated embryos (green) and their phase (blue) obtained with pyBOAT** (Mönke et al., 2020)**.** The phase of oscillations ranges from 0 to 2π. The phase is defined as 0 or 2π at the peaks of oscillations and π at the troughs. Grey stars show when a phase of $0/2\pi$ does not visually correspond to a peak in Her1-mNG traces.
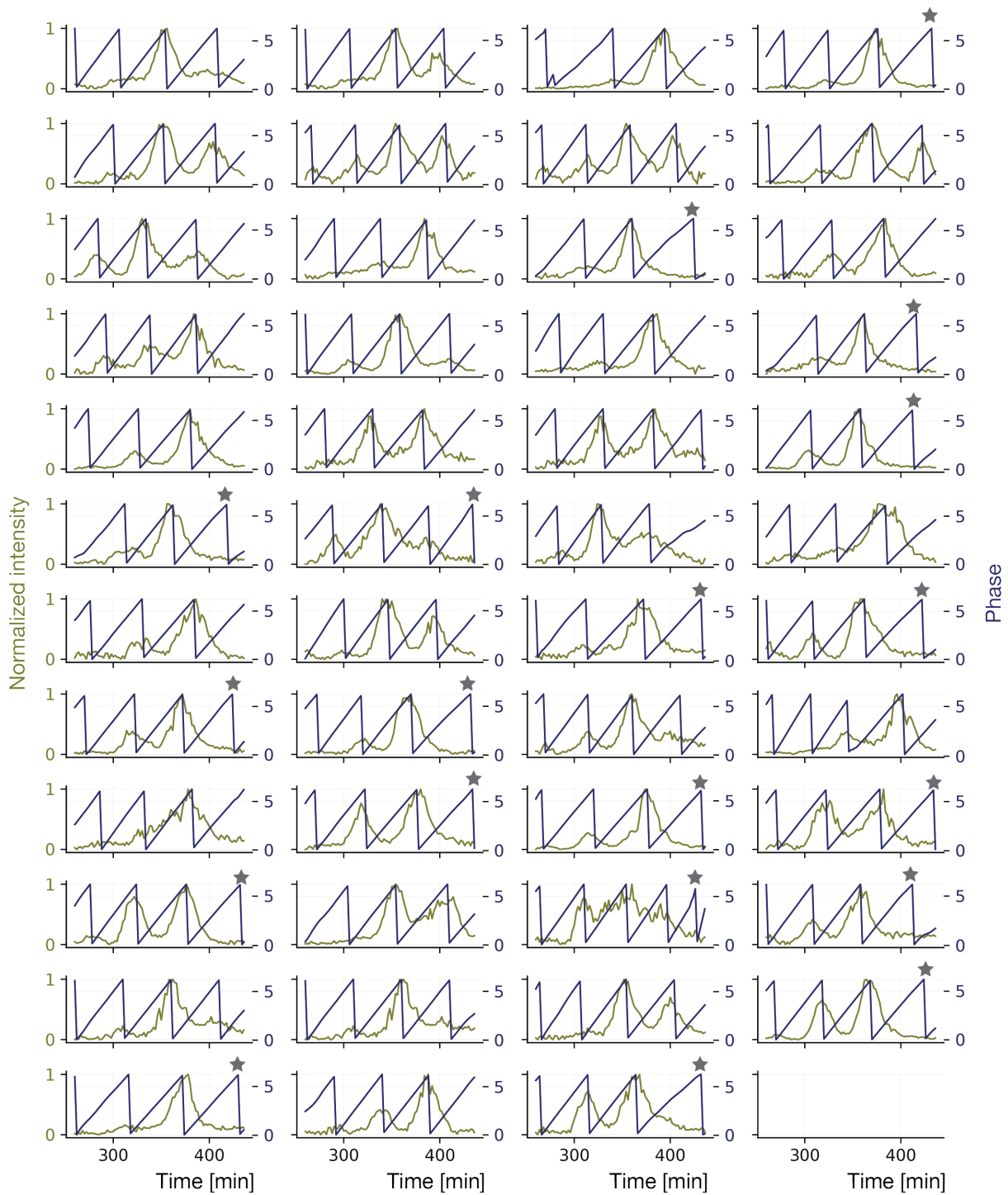
We calculated the global phase coherence of the different cell populations forming somite boundaries. For a given timepoint, the global phase coherence is given by:

$$r = \left| \frac{1}{N} \sum_{j=1}^{N} e^{i\theta_j} \right|$$

where r is the global phase coherence, N is the number of cells in the population and θ_j is the phase of the cellular oscillator *j* at that timepoint. Fig. 28 shows the phase coherence over time of cells back-tracked from normal ("DMSO 1", "DMSO 2", "DAPT 2 – Normal boundary") or defective somite boundaries ("DAPT 1", "DAPT 2" and "DAPT – 3"), aligned by the last peak of their mean Her1-mNG signal. As suggested by the Her1-mNG traces (Fig, 23-25), the phase coherence is higher in cell populations that form normal somite boundaries than in cell populations that form defective somite boundaries. The phase coherence in cells back-tracked from normal boundaries in DMSO-treated embryo is higher (> 0.8, DMSO 1 and 2) than the phase coherence in cells back-tracked from a normal boundary located in the « intermingled region » of a DAPT-treated embryo (~0.6, DAPT 2 – Defective boundary). The phase coherence in cell populations forming defective boundaries range from approximately 0.1 to 0.45. This suggests that value of the phase coherence threshold Z_c for the formation of normal boundaries might be between 0.45 and 0.6.
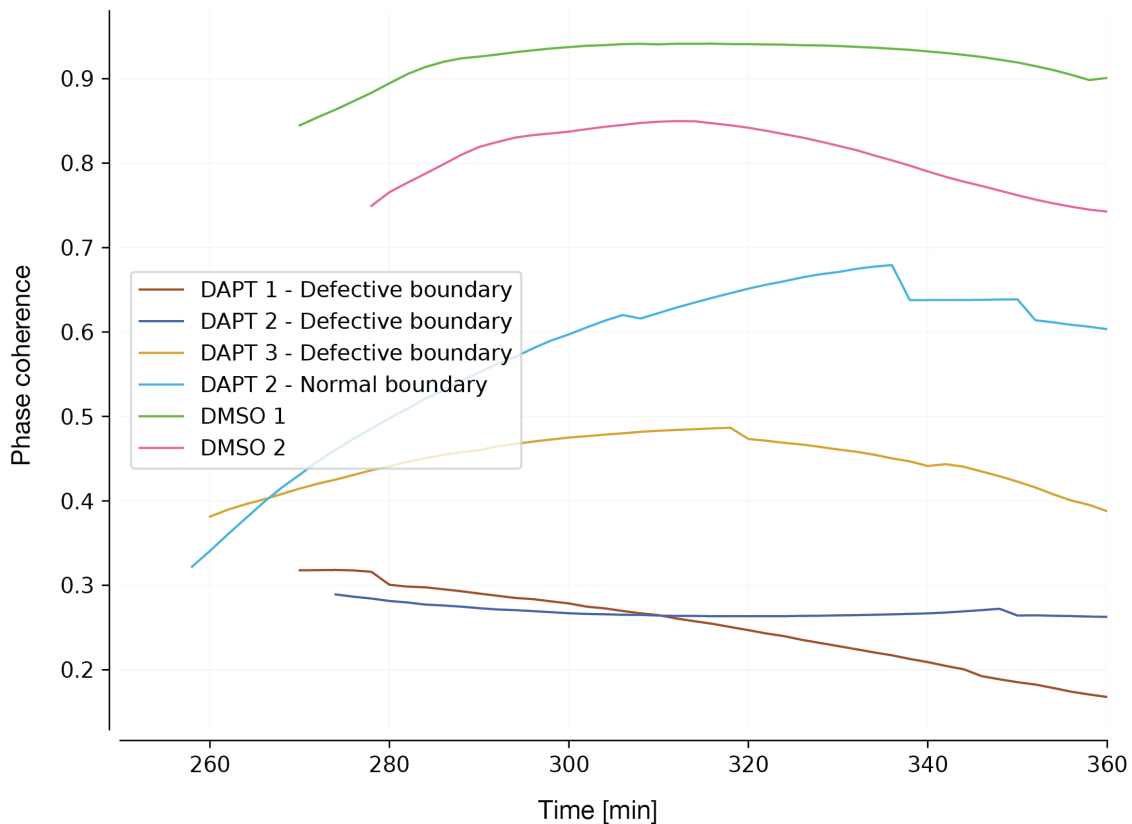

Figure 28: **Global phase coherence over time of cells back-tracked from normal or defective somite boundaries**. Signals are aligned by the last peak in their mean Her1-mNG signals.

3.2.7 The cellular phase coherence is heterogenous in cell populations forming defective boundaries

The global phase coherence only measures the level of synchrony in the entire cell population and does not explain the underlying cause of a given level of synchrony. Different oscillatory behaviors can lead to the same global phase coherence. For example, the phase coherence of a given population of oscillators can be low because every oscillator has a slightly different phase or because two subpopulations of oscillators oscillate in anti-phase. To distinguish between such cases, we calculated the local phase coherence in the PSM. To do so, we computed the cellular phase coherence, which corresponds to the phase coherence between one cellular oscillator and its neighbors. The cellular phase coherence is given by the same equation than the global phase coherence except that N, the number of oscillators in the system, now corresponds to the number of neighbors instead of the size of the cell population. The cellular phase coherence is calculated for each cell in population and for each timepoint.

In absence of a membrane marker, we do not know which cells are actually physically touching. Therefore, we computed the cellular phase coherence between one cell and its nearest neighbors, based on the distance between the center of their nuclei. We varied the number of nearest neighbors from 2 to 7 and we compared the distribution of cellular phase coherence between cell populations forming normal ("DMSO 1", "DMSO 2", "Normal boundary in DAPT 2") and defective boundaries ("DAPT 1, 2 and 3"). Although the distribution of cellular phase coherence varied depending on the number of nearest neighbors, the relative differences between the different conditions did not change. This suggests that the computation of the cellular phase coherence is relatively robust to changes in the number of nearest neighbors. Since we did not track all the cells in the PSM but only a subset of cells that end up forming a somite boundary, we estimated that 6 neighbors was a reasonable assumption in these cell populations and we use this number to compute the cellular phase coherence in our future analysis. For each cell, the mean value of the phase coherence over time was taken to generate a distribution used for comparing treatments and boundaries (Fig. 29).
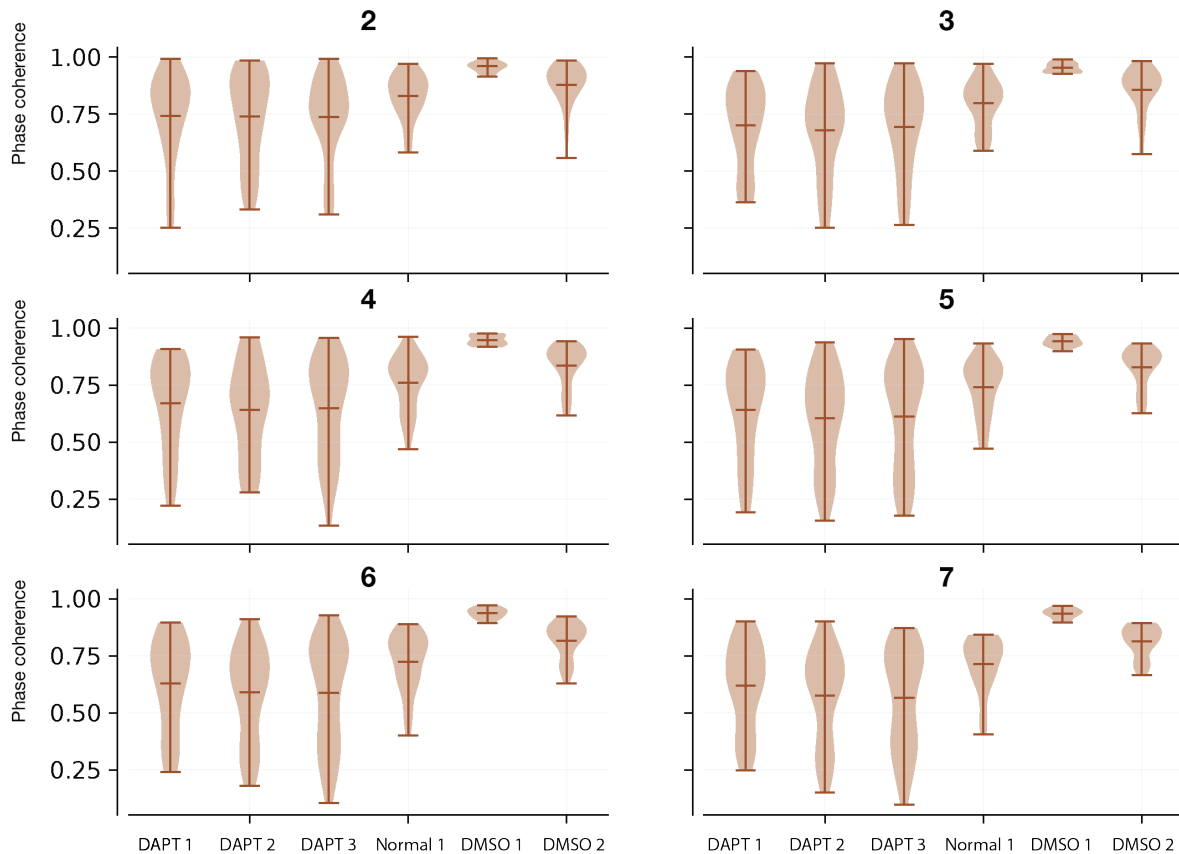
Figure 29: **Violin plot of the cellular phase coherence in cell populations forming normal (DMSO 1, DMSO 2, Nomal 1) or defective somite boundaries (DAPT 1, DAPT2, DAPT 3) for different number of nearest neighbors**. The cellular phase coherence of one cell and its nearest neighbors is calculated for each cell and each timepoint. For each cell, the median value of the phase coherence over time is taken for the distribution. The number of nearest neighbors ranged from 2 to 7. Although the distribution of cellular phase coherence varies depending on the number of nearest neighbors, the relative differences between the different conditions do not change.

The distribution of cellular phase coherence showed a higher intra-variability within cell populations forming defective boundaries than those forming normal boundaries (Fig. 29, DAPT 1, 2 and 3). Thus, the local phase coherence is a measure that appears to distinguish whether a boundary will be defective or not. We observed that defect in somite and segment boundaries were often restricted to a specific part of the boundary (Fig. 22C and D). Some defective boundaries can therefore be divided in a locally correct part and a locally defective part. Are locally-restricted defects caused by a locally low level of phase coherence?

3.2.8 The cellular phase coherence is lower in cells making the defective part of somite boundaries

To address whether locally-restricted defects are caused by a locally low level of phase coherence, we divided defective somite boundaries into a correctly-formed part and a defective part by visual assessment of the spatial arrangement of nuclei. Somite boundaries are made of a posterior and an anterior epithelial layer of nuclei (Fig. 23A and B). It is possible that only one side of the boundary causes the local defect. Therefore, we also divided somite boundaries into a posterior and an anterior side. Cells back-tracked from defective boundaries ("DAPT 1, 2 and 3") were distributed into four categories: "Defective – Anterior", "Defective – Posterior", "Correct – Anterior" and "Correct – Posterior" (Fig. 30A).

Figure 30: **Her1-mNG traces in cells forming defective somite boundaries divided in four categories.** A) Schematic of a defective boundary, with the locally defective part marked in red. Cells back-tracked from defective boundaries ("DAPT 1, 2 and 3") were distributed into four categories: "Defective – Anterior", "Defective – Posterior", "Correct – Anterior" and "Correct – Posterior". B) Her1-mNG traces of cells in each category for the defective boundaries in embryos "DAPT 1, 2 and 3". (n = 6, 15, 12 and 14 cells in DAPT 1, n = 23, 12, 5 and 8 cells in DAPT 2, n = 23, 23, 17, 11 cells in DAPT 3).

When comparing Her1-mNG oscillations between the four categories, the Her1-mNG traces seemed to be overall more coherent in cells from categories "Correct – Anterior" and "Correct – Posterior" than in categories "Defective – Anterior", "Defective – Posterior" (Fig. 30B). This trend was confirmed by directly comparing the cellular phase coherence values between these categories (Fig. 31). Cellular phase coherence values were generally lower in cells making the defective part of defective boundaries (Fig. 31B). This result suggests that the high intra-variability in the distribution of cellular phase coherence in a defective boundary (Fig. 29) can be explained by the difference between the cellular phase coherence of cells making the correct and the defective parts of the boundary. Note that cells in different categories are not independent samples since they come from the same embryo. This violates the assumption of independence that most statistical tests rely on. Therefore, we only show the distribution of cellular phase coherences, without performing any statistical test.
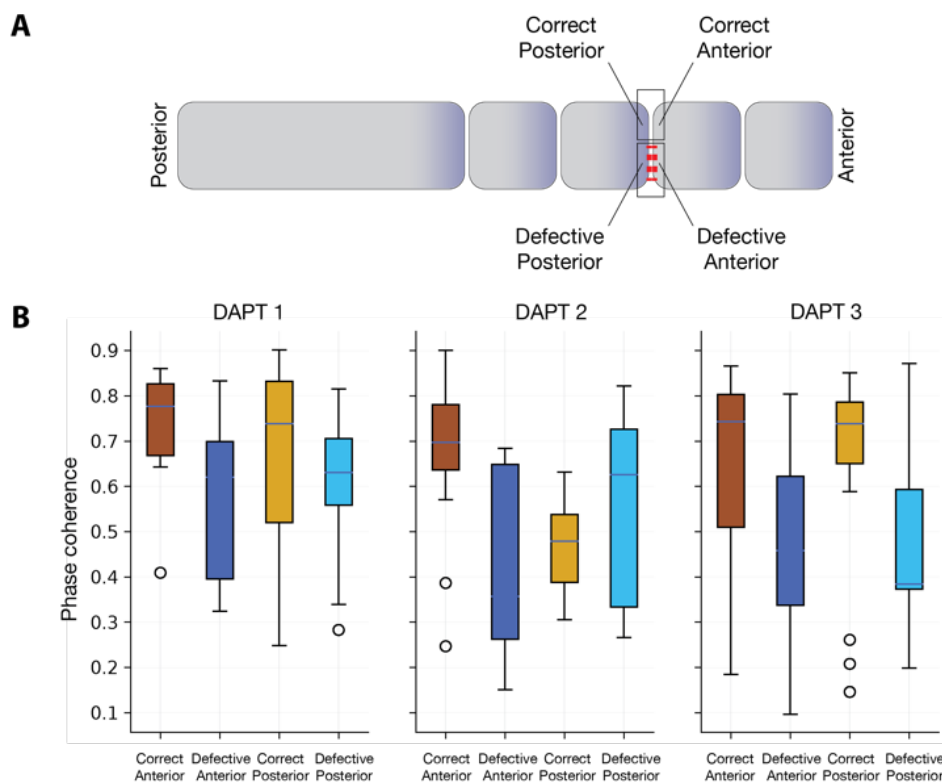
Figure 31: **Distribution of the mean cellular phase coherence in cells forming defective somite boundaries.** A) Schematic of a defective boundary, with the locally defective part marked in red. Cells back-tracked from defective boundaries ("DAPT 1, 2 and 3") were distributed into four categories: "Defective – Anterior", "Defective – Po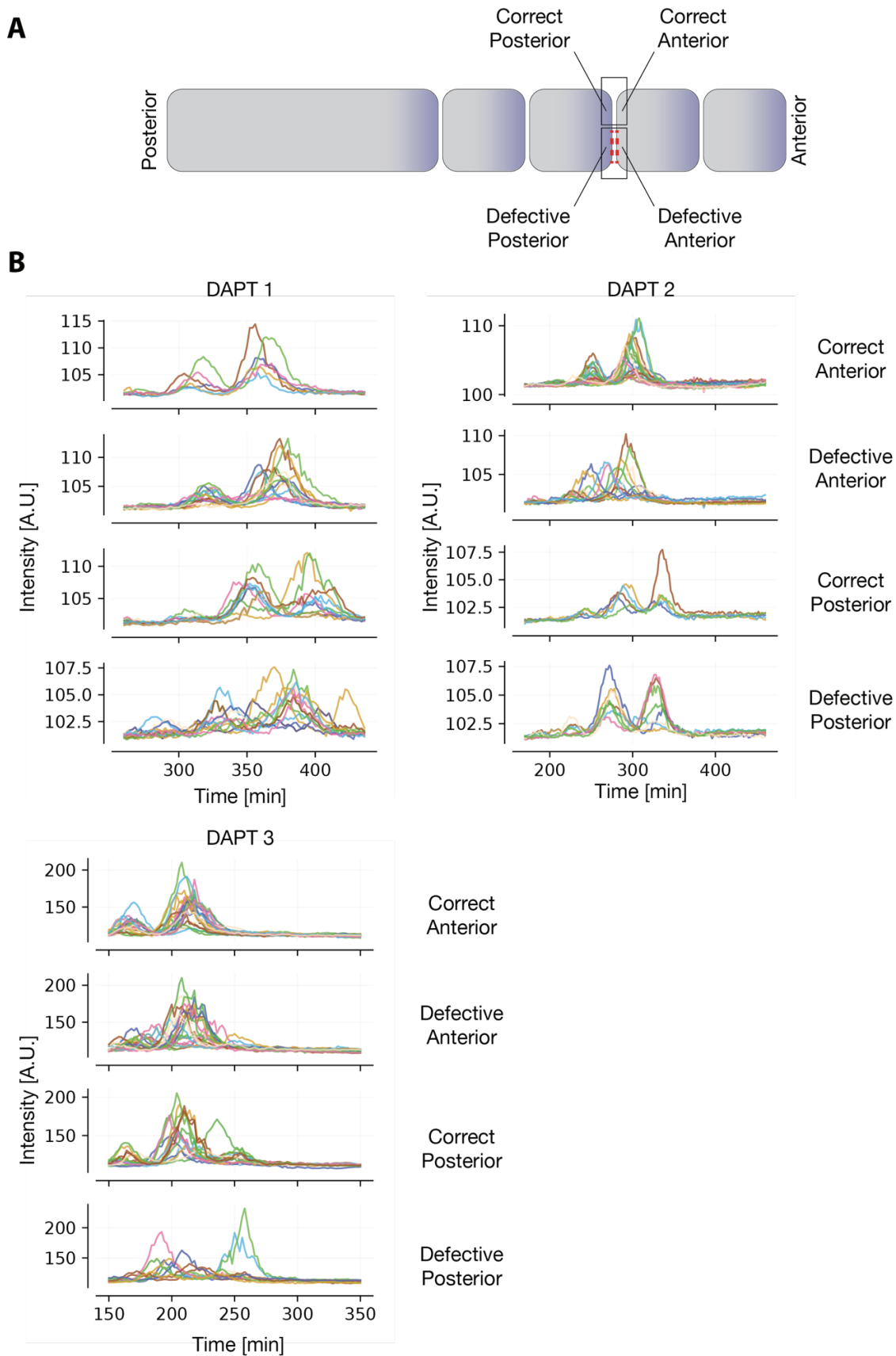sterior", "Correct – Anterior" and "Correct – Posterior". B) Distribution of the mean cellular phase coherence of cells from categories "Defective – Anterior", "Defective – Posterior", "Correct – Anterior" and "Correct – Posterior" for three defective boundaries (DAPT 1, 2 and 3).

3.2.9 Spatial representation of cells in "PSM transections"

To confirm the trend that cells forming the defective part of boundaries have a lower cellular phase coherence than cells forming their correct part, we wanted to spatially visualize the cellular phase coherence in the PSM and compare it with the location of somite defects in boundaries. Since defects in somite boundaries were often spatially restricted to a specific area of the somite boundary, they are best visualized when projected along the A-P axis,

and represented into the dorso-ventral (D-V) and media-lateral (M-L) axes (Fig. 32A). We call this view a "PSM transection" as it virtually represents a transverse cut of the PSM.

The mathematical details of the geometrical transformation are explained in the Materials and Methods section. To project cell positions along the A-P axis, we needed to find a reference of the A-P axis in our timelapses. As the notochord forms a straight line along the A-P axis, it can be used as a spatial reference. For each timelapse, we tracked two positions in the notochord. One position is anterior (yellow star, Fig. 32), and the other is posterior (magenta star, Fig. 32) to the position of cells back-tracked from somite boundaries. For each timepoint, the reference points on the notochord (yellow and magenta stars, upper left part of the 3D plot) were translated and rotated so that one of the reference points (yellow star) is placed at the origin (0, 0, 0) and the other reference point (magenta star) is aligned along the x-axis (lower right part of the 3D plot). The same transformation (translation and rotations) was applied to the positions of cells (Fig 32B). This transformation did not modify the relative position of cells, it simply allowed the represention of their positions in the D-V and M-L axes (Fig. 32C), making possible the visualization of defects in somite boundaries in two dimensions.
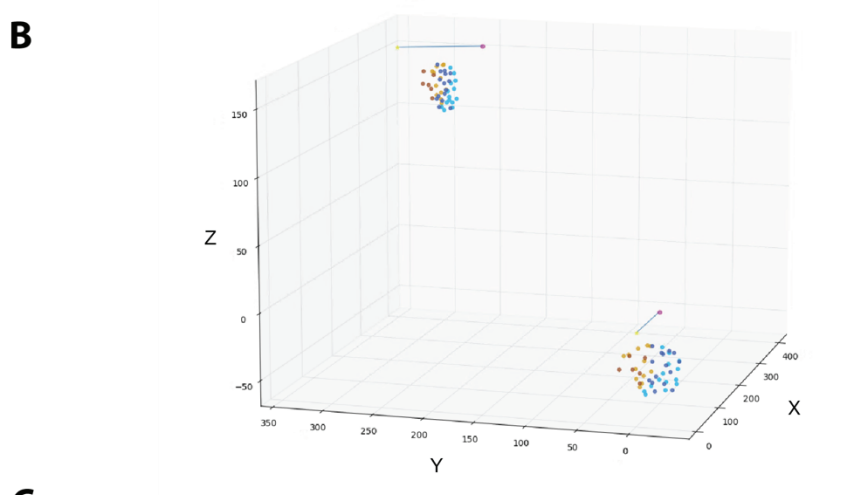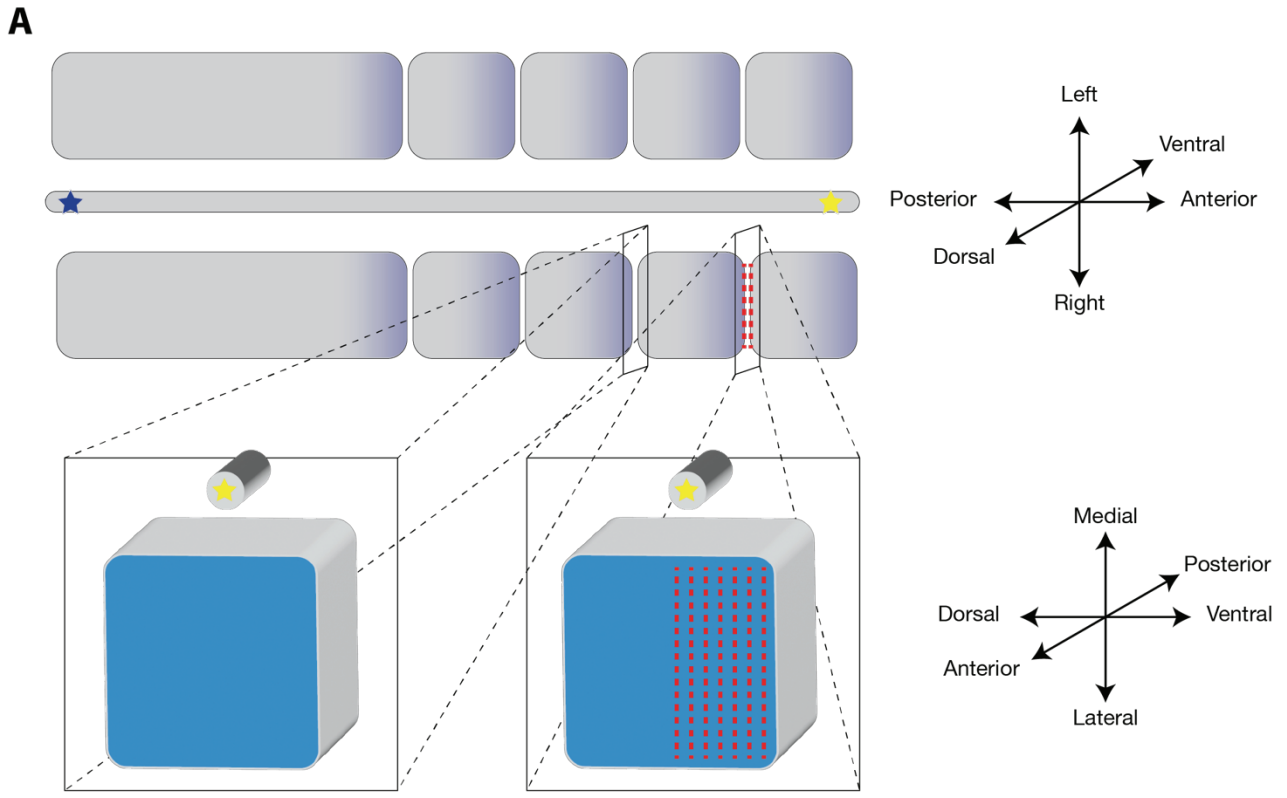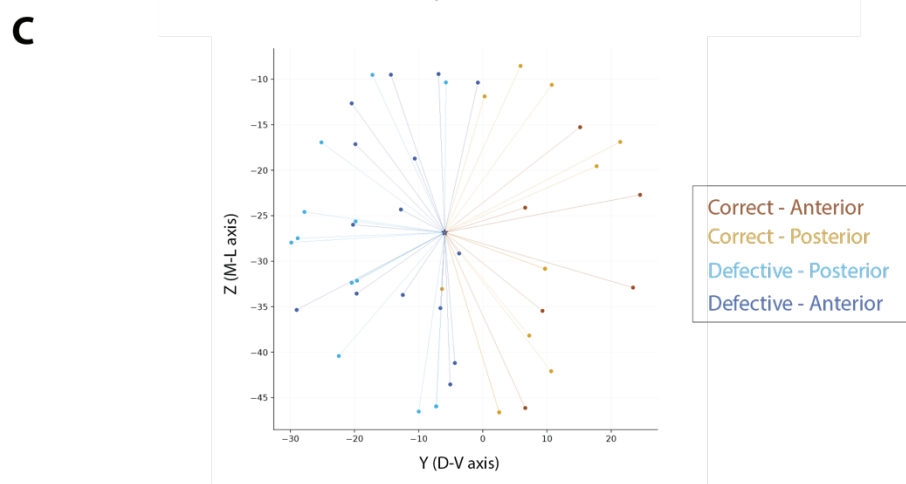
Figure 32: **Transformation and projection of cell positions along the antero-posterior (AP) axis.** A) Schematic of the PSM, formed somites, and the notochord along the 3 embryonic axes. Since defects in somite boundaries are often spatially restricted to a specific area of the somite boundary, they are best visualized when projected along the A-P axis and represented into the dorso-ventral (D-V) and media-lateral (M-L) axes. This schematic shows two boundaries composed of synthetic data for illustration. One normal boundary

(left) and one defective boundary with a defect restricted to its ventral part (right). The notochord is used as a reference for the projection along the AP axis. Two positions in the notochord are tracked in timelapses to provide spatial references of the AP axis. One position is anterior (yellow star), and the other is posterior (magenta star) to the position of cells back-tracked from somite boundaries. B) Positions of tracked cells in 3 dimensions, along with the positions of the reference points in the notochord. Cells are color-coded by their category ("Defective – Anterior", "Defective – Posterior", "Correct – Anterior" and "Correct – Posterior"). For each timepoint, the reference points of the notochord (yellow and magenta stars, upper left part of the 3D plot) were translated and rotated so that one of the reference point (yellow star) is at the origin (0, 0, 0) and the other reference point (magenta star) is aligned along the x-axis (lower right part of the 3D plot). The same translation and rotations were then applied to cell positions. C) After the transformation, the x-, y- and z-axes respectively corresponded to the A-P, D-V and M-L axes of the embryo. The y- and z-axes represented a transection of the PSM and of somite boundaries. Cells are color-coded by their category ("Defective – Anterior", "Defective – Posterior", "Correct – Anterior" and "Correct – Posterior"). In this example, the boundary has a ventral defect. The blue star represents the mean position of cells in this transect.

3.2.10 The cellular phase coherence is spatially heterogeneous in the PSM

Displaying the temporal average of cellular phase coherence values in a PSM transection revealed areas of high and low phase coherence (Fig. 33). In the theory of oscillators, the coexistence of synchronous and asynchronous populations of oscillators is termed a chimera state (Petrungaro et al., 2017).To the best of our knowledge, chimera states have never been observed in the segmentation clock of any model organism. PSM regions with high, respectively low, phase coherence levels spatially correlate with the location of correct, respectively defective, parts of the somite boundary (Fig. 33). This confirms that local synchrony of oscillators is predictive of the final state of a boundary.

The transition from local synchrony to global pattern recovery has been recently studied using a physical model of the PSM (Uriu et al., 2021). Simulations combining tissue mechanics and coupled oscillator suggested that spatially heterogeneous resynchronization of the segmentation caused intermingled defects. The results of these simulations are in agreement with our analysis of the phase coherence in the PSM during the resynchronization of the segmentation clock. Interestingly, in these theoretical studies, phase vortices were observed during the transition from local synchrony to global pattern recovery, and we now turn to investigating their existence during resynchronization in the embryo.
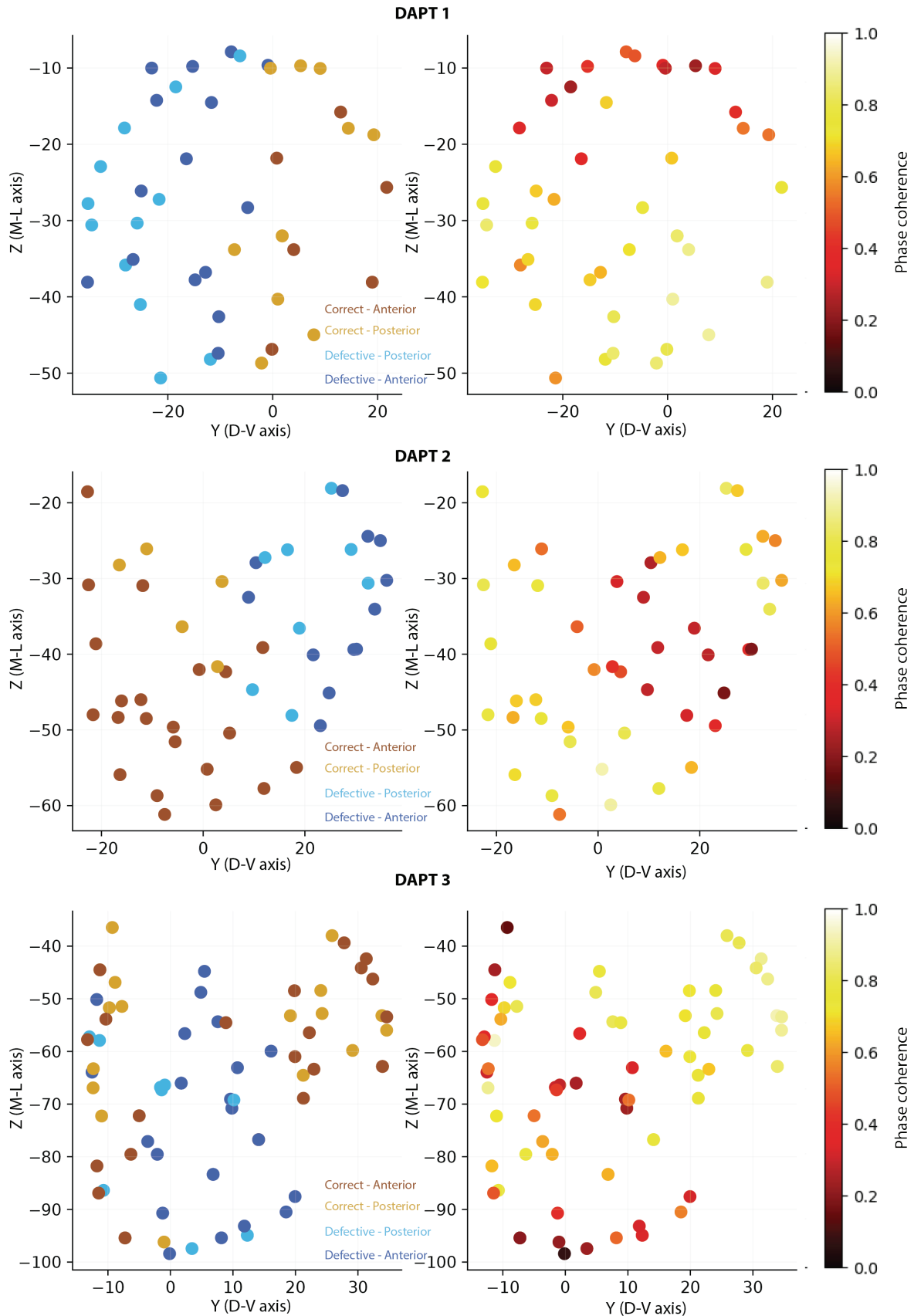
Figure 33: **The cellular phase coherence is spatially heterogeneous in the PSM.** Left) Mean positions of cells back-tracked from defective boundaries of embryos "DAPT 1, 2 and 3" represented in the D-V and M-L axes. Each dot represents the temporal mean position of a cell in the PSM. Cells are color-coded by their category ("Defective – Anterior", "Defective – Posterior", "Correct – Anterior" and "Correct – Posterior"). Right) Temporal mean of cellular phase coherence values as a function of the position in the D-V and M-L axis in the PSM. The mean values of the cellular phase coherence are spatially heterogeneous in the PSM. Regions of lower cellular phase coherence values seem to spatially correlate with the location of defects in the somite boundary.

3.2.11 Phase vortices were experimentally observed during the resynchronization of the segmentation clock

Can we observe phase vortices in our timelapses during the resynchronization of the segmentation clock? Cells back-tracked from a somite boundary have roughly the same position with respect to their neighbors and within the ML and DV axes of the PSM as they move along the antero-posterior axis of the PSM. Therefore, cells from a given PSM transection should have a similar phase at any timepoint if waves of gene expression are travelling anteriorly in the PSM. In contrast, if the phase pattern rotates along one axis, cells in different areas of the PSM transection should have a gradient of phases around this axis. In the case of a phase vortex rotating along the AP axis, we should observe a phase vortex in the PSM transection (Fig. 34A). Since we already transformed the positions of cells and projected them in PSM transections, we started by investigating whether we could observe a rotating phase pattern along the A-P axis of the PSM.

To test whether a cell's phase is a function of its position in the PSM transection, we assigned an angle α for each cell in the PSM transection at every timepoint. For each timepoint, we computed the center of the PSM transection by taking the mean position of all cells in PSM transection. For each cell, we defined α as the angle between a vector joining the center of the PSM transection and the cell position in the transection and the horizontal line running through the center of the PSM transection (Fig. 34B). We computed the angle α for each cell in the PSM transection at every timepoint. To visualize the relationship between a cell's phase and its position in the PSM transection, we plotted, for each cell, the angle α over time, color-coded by the cell's phase. Fig 35. and Fig. 36 show this representation of the phase pattern in cells back-tracked from normal or defective boundaries, respectively.

At a given timepoint, cells back-tracked from a normal boundary had a similar phase irrespective of their angle α (Fig. 35). In other words, the phase pattern was vertically straight in this representation. This indicates that the phase of oscillations did not depend on the cell position in the PSM transection, which is expected when waves of gene expression travel anteriorly in the PSM. With this representation, it also appeared that the angle α of most cells remained fairly constant over time, indicating that cells did not move much over time in PSM transections. This results is expected as cells travel along the PSM with little to no cell mixing (Mongera et al., 2018; Thomson et al., 2021) and therefore supports the fact that the angle α faithfully captures cell positions in the PSM transection.

The phase pattern was found to be more complex in cells forming defective somite boundaries located in the "intermingled region" (Fig. 36). We could distinguish 3 qualitative features of the phase pattern during the resynchronization of the segmentation clock. In some subregions of the PSM transection, the phase pattern was relatively straight, suggesting that a group of cells were synchronized with the same phase. The straight phase pattern suggests that, in this cell population, waves of gene expression travelled anteriorly along the PSM, similarly to what happens during the formation of normal somite boundaries. In contrast, there were other subregions in the PSM transection where the phase of cells varied with the angle α. In other words, the phase pattern made a slope in this representation. This indicates a relationship between the phase of oscillations and the position of cells in the PSM transection, which is a signature of phase vortices travelling in the PSM. In some other areas of the PSM transection, the phase pattern appeared to be fuzzy, probably due to a lower local level of synchrony. Note that phase patterns (waves, vortices, fuzzy

patterns) were found to repeat over Her1-mNG oscillations (Fig. 36), which suggests that they are likely advected by cells as they cross the PSM.
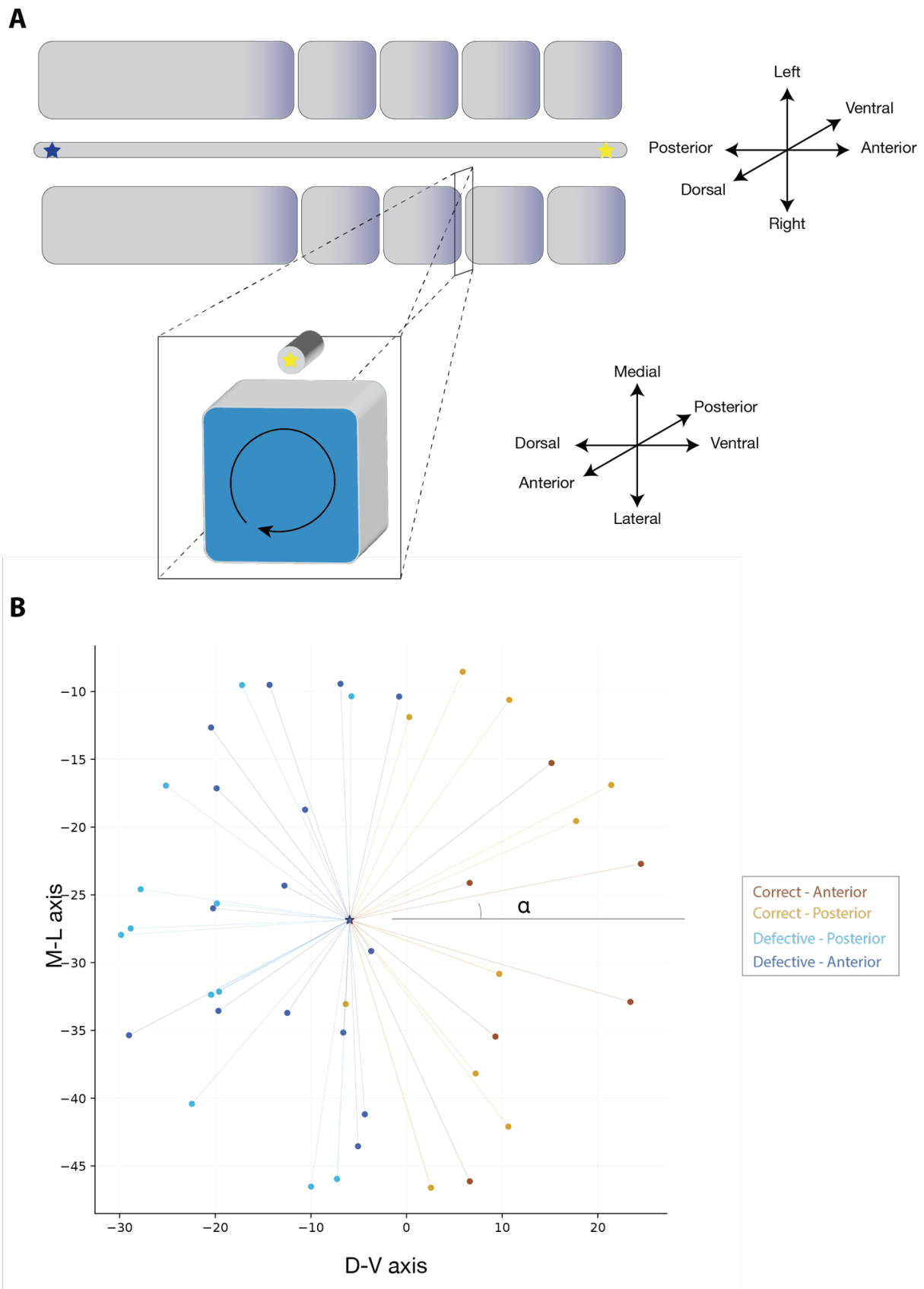
Figure 34: **The angle α defines the positions of cells in the PSM transection.** A) Schematic of a phase vortex rotating along the A-P axis of the PSM. B) α was defined as the angle between a vector joining the center of the PSM transection (star) and the position of a cell (dot) in the transection and the horizontal running through the center of the PSM transection (line).
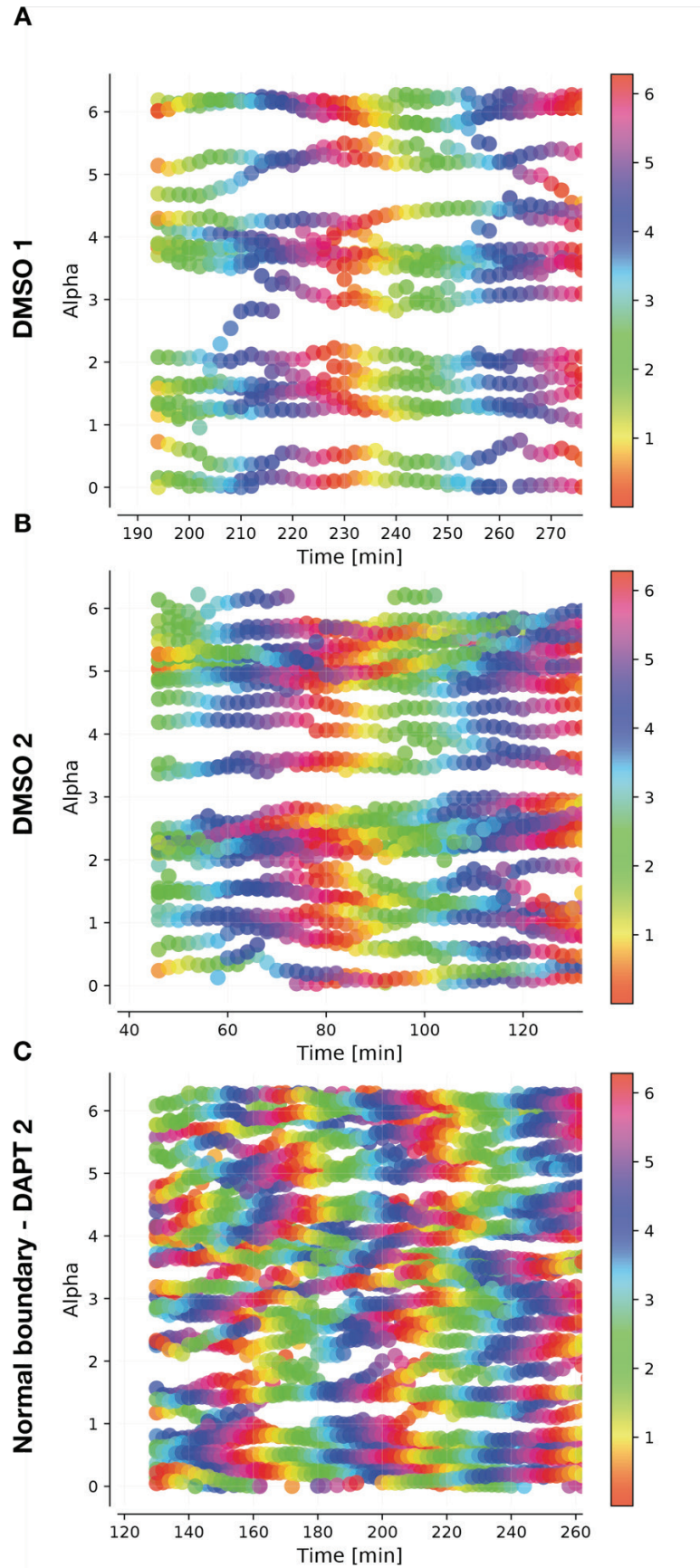
Figure 35: **Relation between a cell's phase and its position in the PSM transection over time in cells back-tracked from normal boundaries.** A and B) Cells were back-tracked from normal somite boundaries in DMSO-treated embryos. C) Cells were back-tracked from a normal boundary located in the "intermingled region" in a DAPT-treated embryo ("DAPT 2"). In these 3 examples, cells at a given timepoint had a similar phase irrespective of their angle α. In other words, the phase pattern was vertically straight in this representation. This indicates that the phase of oscillations does not depend on the cell position in the PSM transection, which is expected when waves of gene expression travel anteriorly in the PSM. Note that the angle α is 2π-periodic so there is a continuum between the bottom and the top parts of the plot.
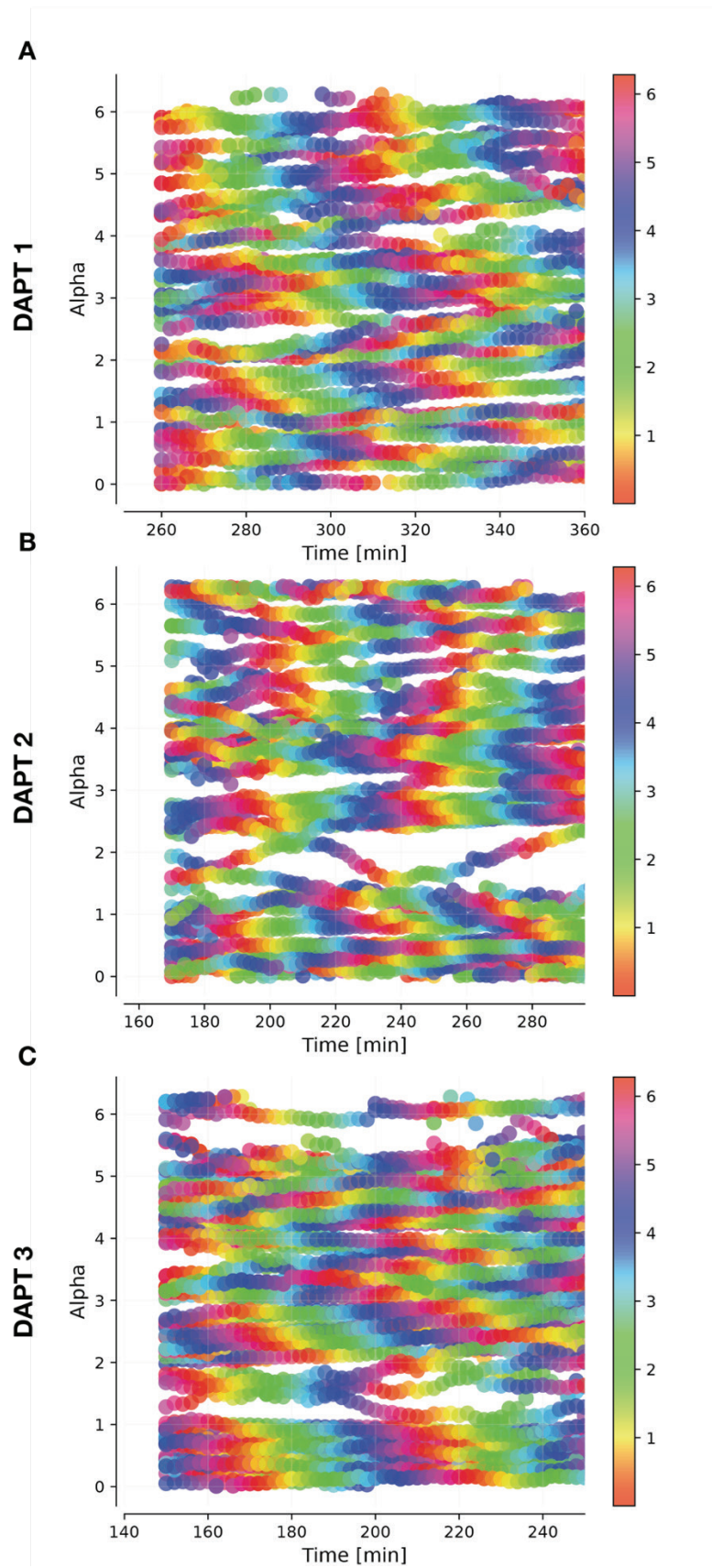
Figure 36: **Relation between a cell's phase and its position in the PSM transection over time in cells back-tracked from defective boundaries.** A, B and C) Cells were back-tracked from defective somite boundaries located in the "intermingled region" in DAPT-treated embryos ("DAPT 1, 2 and 3"). In these 3 examples, there were regions in the PSM transection where the phase of cells varied with the angle α. In other words, the phase pattern had a slope along α in this representation. This indicates a relationship between the phase of oscillations and the position of cells in the PSM transection, which is expected if phase vortices travel in the PSM. In some other areas of the PSM transection, the phase pattern appeared to be fuzzy, probably due to a lower local level of synchrony. Note that the angle α is 2π-periodic so there is a continuum between the bottom and the top parts of the plot.

3.2.12 Correct parts of defective boundaries spatially correlate with the normal wave pattern

To investigate the spatial relationship between the three qualitative phase patterns (waves, vortices, fuzzy pattern) and the location of boundary defects in PSM transections, we compared the locations of cells forming correct and defective parts of somite boundaries, with the phase pattern and the cellular phase coherence in PSM transections.

We first examined normally forming boundaries. The phase coherence of cells forming normal boundaries in DMSO-treated embryos was high and the phase pattern was vertically straight (Fig. 37). In cells forming a normal boundary located in the "intermingled region" of a DAPT-treated embryo, the phase coherence appeared to be lower and more spatially heterogeneous than in DMSO-treated embryos (Fig. 37). The phase pattern seems to be less straight.

In contrast, in the three defective somite boundaries that were analyzed, cells located in regions where the phase pattern behaved as normal travelling waves had a high cellular phase coherence and ended up forming the correct parts of defective boundaries. In contrast, cells located in regions of the PSM transection where the phase pattern was either fuzzy or travelled as a vortex, tended to form the defective parts of somite boundaries. Thus, the analysis of local synchrony in resynchronizing embryos has revealed the existence of phase vortex patterns, and shows that their location predicts the presence of a defective somite boundary.
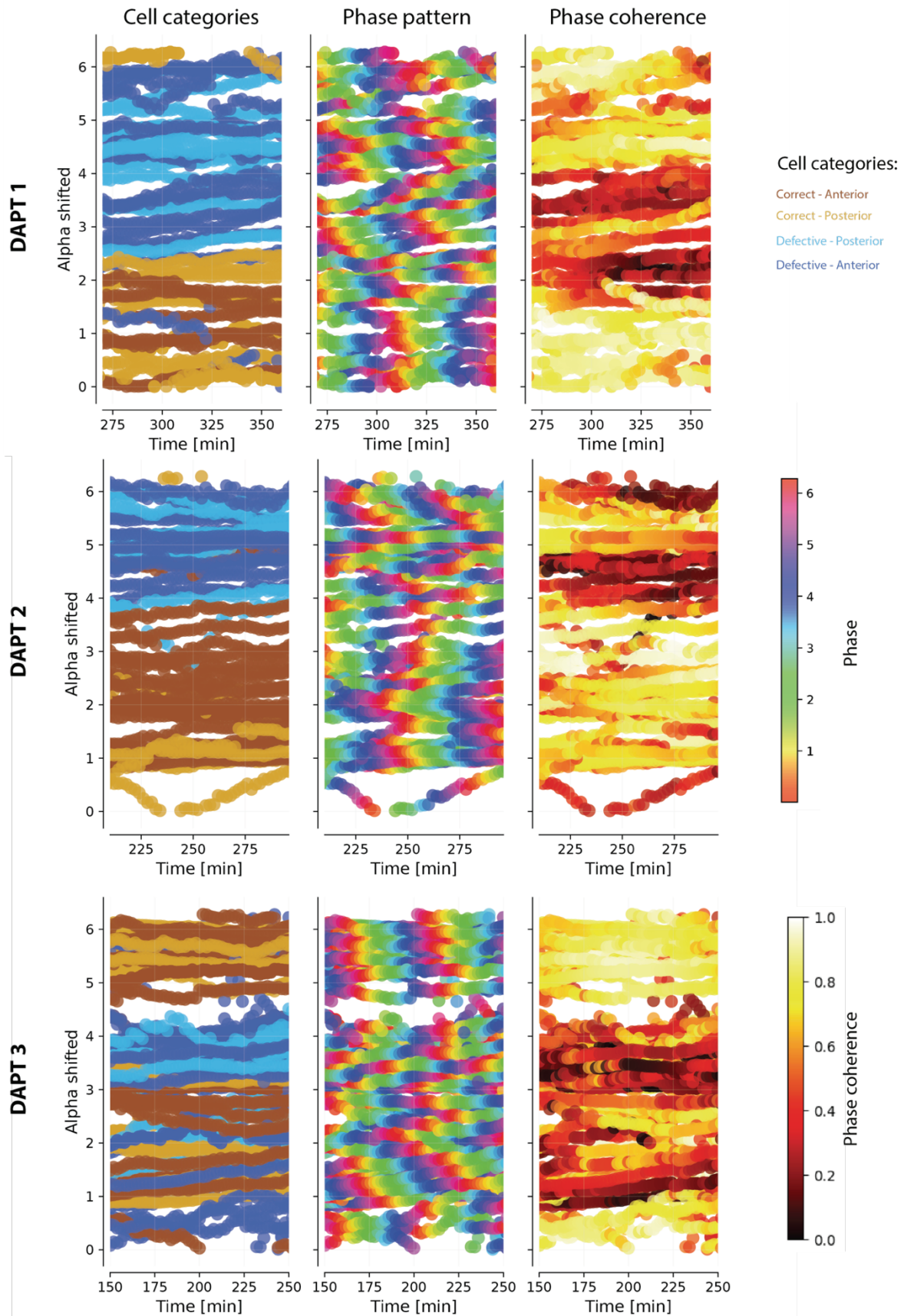
Figure 37: **Comparison between cell categories ("Correct – Anterior", "Correct – Posterior", "Defective – Anterior" and "Defective – Posterior"), phase pattern and cellular phase coherence in PSM transections of defective boundaries**. The phase pattern tended to act as waves in cells from categories "Correct – Anterior" and "Correct – Posterior". These cells also tended to have a higher cellular phase coherence. In cells from categories "Defective – Anterior" and *Defective – Posterior", the phase pattern tended to either behave as a vortex or to be fuzzy. Since the bottom and the top parts of the plot are continuous, an offset can be applied to the angle α so that cells making the defective or the correct parts of boundaries are not split between the upper and the lower parts of the graph.
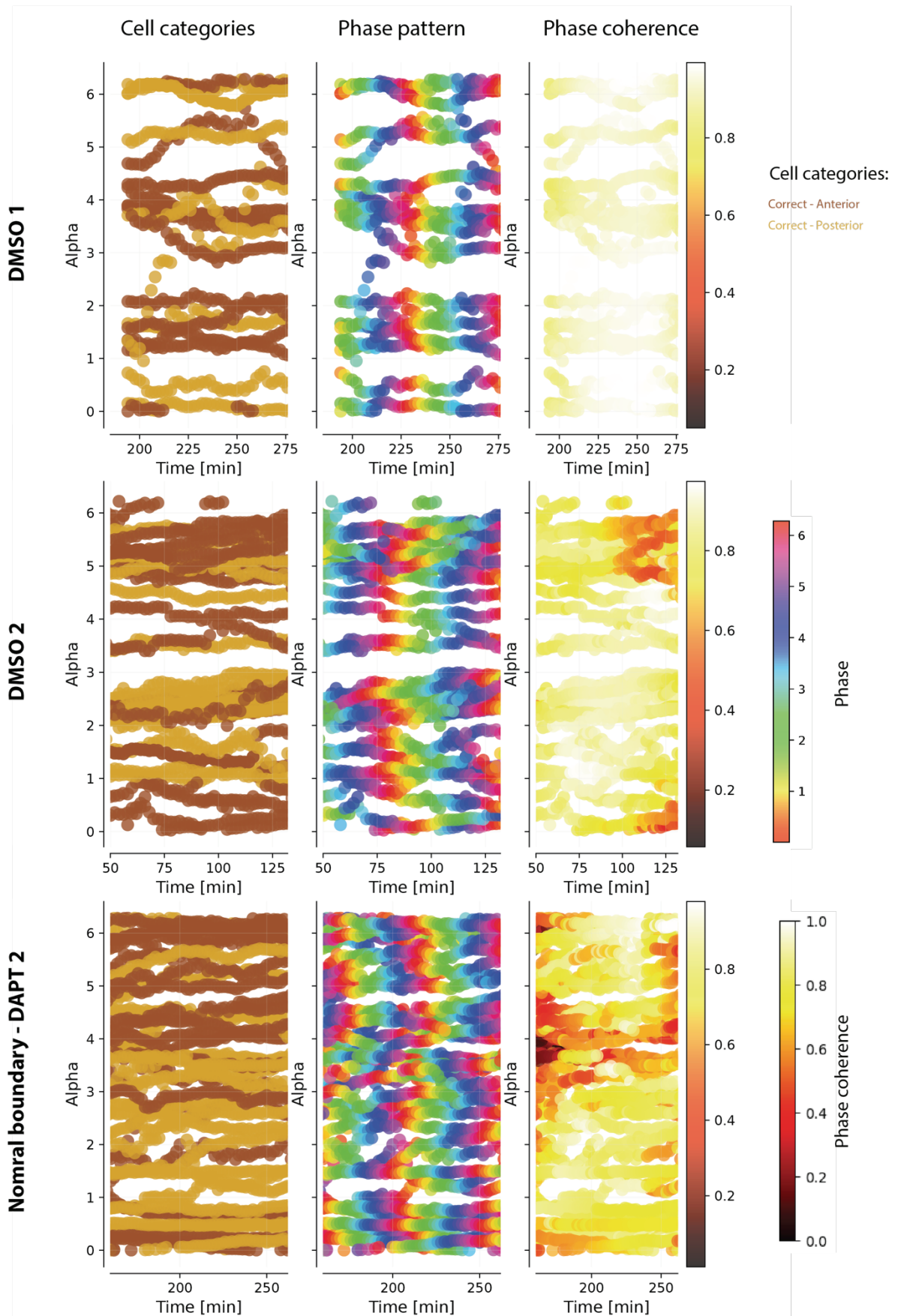
Figure 38: **Comparison between cell categories ("Correct – Anterior", "Correct – Posterior"), phase pattern and cellular phase coherence in PSM transections of normal boundaries**. Overall, the phase pattern tends to act as normal travelling waves and cells have high values of cellular phase coherence.

3.3   Discussion

In this work, we investigated the formation of defective somite boundaries during the re-synchronization of the segmentation clock. We noticed that some qualitative features of segment defects, such as the location and the shape of the defect, were already visible in somite boundaries. This suggests that defects in somite boundaries, at least relatively severe ones, are not corrected as somites mature to segments. In defective segment boundaries located in the « intermingled region », defects were often not spanning the full somite or segment and were locally restricted to a specific part of the boundary. The location of the earlier somite defect predicted the location of the later segmental defect.

By following individual segmentation clock cells and tracking their oscillations, we observed that the local phase coherence was generally lower in cells forming the defective part of the boundary than in cells forming the correct part of the boundary. The spatial distribution of the phase coherence in PSM transections revealed that the phase coherence was spatially heterogeneous, with regions of high and regions of low phase coherence. The co-existence of synchronous and asynchronous regions in a population of oscillators is termed a chimera state.

To investigate the cause of the spatial heterogeneity in the phase coherence, we assessed the relationship between the phase of oscillators and their positions in PSM transections, defined by an angle α. We observed three kinds of phase patterns that co-existed in the PSM during the resynchronization of the segmentation clock: normal waves travelling anteriorly in the PSM, phase vortices rotating along the A-P axis and fuzzy phase patterns.

In some regions of PSM transections, oscillators were synchronous and their phase was independent of their angle α. This indicates that, in these regions, waves travelled anteriorly in the PSM, similarly to waves of gene expression in control embryos. In other regions of the PSM transections, we found a relationship between the phase of an oscillator and its angle α. This indicates that the phase pattern rotates in the PSM transection as it travels anteriorly in the PSM. As the angle α was defined in dorso-ventral, media-lateral PSM transections, we only observed local phase vortices rotating along the A-P axis travelling along the PSM. This does not exclude that phase vortices also rotate along other axis but we cannot test that with our current analysis.

Note that phase vortices are repeated over a few cycles (Fig. 36). This suggests that they are formed in the tailbud or in the posterior PSM and are slowly carried by cell advection across the PSM. Cells forming phase vortices are likely to be phase-locked with their neighbors along the angle α. In other words, they have a constant phase offset with their neighbors along the angle α and this offset creates the persistent phase vortex.

Cells where the phase pattern behaved as travelling waves tended to form the correct parts of defective boundaries while the phase pattern was generally either fuzzy or travelling as a vortex in cells forming the defective parts of boundaries. This suggests that, as the phase pattern is advected along the PSM and reaches the determination wavefront, phase

vortices or fuzzy patterns do not create a sharp stripe of gene expression that might be necessary for correct boundary formation.

Although the current study is not complete, the results suggest that boundary defects can arise when the level of synchrony is locally under a certain threshold. We can speculate that the severity of boundary defects depends on the size of the region where the local phase coherence is under this threshold. Importantly, these preliminary results provided experimental support for the advection of persistent phase vortices predicted by a physical model of the PSM (Uriu et al., 2021). This model suggests that the global resynchronization of the segmentation clock occurs at two different spatio-temporal scales: a rapid synchronization between neighboring cellular oscillators and the slow advection of the phase pattern across the PSM.

Chapter 4   Image analysis pipeline[5]

Title: But, what are the cells doing? Image Analysis pipeline to follow single cells in the zebrafish embryo

Authors:

Arianne Bercowsky-Rama[1,†], **Olivier F. Venzin[1,†],** Laurel A. Rohde[1], Nicolas Chiaruttini[2], Andrew C. Oates[1,*]

Affiliations:

[1]Institute of Bioengineering, École Polytechnique Fédérale de Lausanne; Lausanne, CH

[2]BioImaging and Optics Core Facility, École Polytechnique Fédérale de Lausanne; Lausanne, CH

†Equal contribution

*Corresponding author. Email: <u>andrew.oates@epfl.ch</u>

One-sentence Summary

User friendly cell-tracking pipeline that connects from image acquisition through to data analysis of cellular dynamics in multicellular systems.

Abstract

Microscopy has rapidly evolved at pace with live markers to enable higher spatiotemporal resolution of multicellular dynamics within bigger fields of view. Consequently, we are now in the era of widespread production of terabyte (TB)-sized timelapse movies of experimental model systems, including developing embryos and organoids. Working with these large datasets has brought a new set of challenges and, as of yet, standardized open-source pipelines for acquiring, handling and analyzing data are still lacking. Moreover, although tracking cells throughout an entire biological process, for example vertebrate

---

[5] I wrote the « Procedure » section of this manuscript.

segmentation, is key to revealing underlying cellular dynamics, this has proven elusive to many researchers. To specifically address the question "But, what are the cells doing?", we created an image analysis pipeline optimized to track single cells in light-sheet acquired datasets (1 TB sized timelapse, 8h of imaging, 30 min genetic oscillatory cycle, speed cell movement (µm/minute), 200-400 µm tissue depth). Our modular pipeline optimizes and connects the following: image acquisition parameters to improve tracking feasibility; hardware specifications; data handling and compression tools; pre-processing steps; connections to state-of-the-art cell tracking tools (Mastodon, Elephant, MaMuT) and a novel open-source/ python-based tool (Paleontologist) to analyze spatiotemporal dynamics of the tracked cells. Importantly, our pipeline is adaptable to a variety of experimental systems and accessible to researchers regardless of expertise in coding and image analysis.

Introduction

Live imaging of multicellular systems for the purpose of describing tissue and cellular spatiotemporal dynamics has become a common? practice in many labs (Attardi et al., 2018; McDole et al., 2018; Shah et al., 2019). We have also recently used this approach to understand the cellular-level dynamics underlying the segmentation clock wave pattern in the developing zebrafish embryo (Rohde et al., 2021; Soroldoni et al., 2014). Here we detail the pipeline we created to facilitate imaging, cell-tracking and data analysis of rapid oscillatory dynamics (30-minute gene expression cycles) and cell movements of individual cells throughout the hours-long timeframe of segmentation. This pipeline is modular and adaptable to similar challenging systems including organoids in which researchers wish to track spot-like structures.

When imaging a tissue at cellular resolution, the ultimate goal is usually to quantify spatio-temporal dynamics of tracked cells. There are two main approaches to cell tracking, the first of which is *in toto* cell tracking, such as performed by McDole et al., 2018, and Shah et al., 2019, in mouse and zebrafish embryos, respectively. These *in toto* approaches relied on automatic algorithms, including TGMM (Tracking with gaussian mixture model, Amat et al., 2014), to generate the cell tracks in the order of many thousands, a scale that renders manual curation unrealistic. Automated tracking accuracy exponentially decays over trajectory length, thus limiting analysis to short tracks as in Shah et al., 2019 (cell tracks of 10 frames, 20 minutes), or requiring custom statistical analysis to infer the dynamics as in McDole et al. 2018 (less than 30 time points over a 2-hour period improved by a factor of 3) The second cell-tracking approach relies on manual or semi-automatic cell tracking (Delaune et al., 2012; Shih et al., 2015; Rohde et al., 2021), in which the user selects cells within a region of interest then manually curates the tracks. Although the number of tracks obtained is relatively lower, in the order of many hundreds, this approach produces reliable trajectories that run considerably longer (100 frames, 150 min, Rohde et al., 2021 using Mastodon). Selection of one of these two approaches will depend on the question being asked and the accuracy required to answer it. Here, our pipeline takes a semi-automatic tracking approach, but includes optimized parameters for both imaging and processing steps to reduce the burden of manual curation.

Despite examples of successful cell tracking and analysis at various scales and timeframes, it remains out-of-reach for many labs due to lack of expertise. A diverse set of skills is required across the many steps of the process, including the following: 1 - preparing and mounting live samples (Kleinhans and Lecaudey, 2019; Hirsinger and Steventon, 2017); 2 - adjusting microscopy setups to produce high resolution images and low photo-toxicity

(Garcia et al., 2011; McConnell et al., 2016); 3 – customizing ? imaging software and hardware (Mc Dole et al., 2018); 4 - post-processing of the acquired data, e.g. deconvolution (Sage, et al., 2017; Preibisch et al., 2014) and registration (Preibisch et al., 2010); 5 - assembling efficient processing and analysis computing hardware (Roger et al., 2016); 6 - segmenting and/or tracking cells in 3D over time (Schmidt, et al. 2018; Weigert et al., 2020) (Tinevez et al., 2017); 7 - and finally, writing bespoke code to analyze the dynamics of the tracked cells (de Medeiros et al., 2021; Zhisong et al., 2020). Thus, without standardized pipelines in place, analysis of spatiotemporal cell dynamics can be a daunting task. Keeping increased accessibility as a goal, here we provide a user-friendly cell-tracking pipeline accompanied by guidance, open-source code and novel analysis software.

In this paper we first give an overview of each of the modules in the pipeline, explaining the main goals and concepts of the process, as well as their application and limitations. In the Materials section, we give the concentrations, parameters and settings that we have optimized specifically for study of the segmentation clock in zebrafish. In the Procedure section, we go into detail of each of the steps in all four modules, also pointing out where, how and why the concentrations, parameters and settings can be modified for application to other samples.

Pipeline Overview, Application and Limitations

The pipeline has 4 main modules (Figure 1): 1) a time-lapse of a live sample is acquired; 2) the time-lapse is processed to facilitate data handling and further analysis; 3) cells are detected as spots and are tracked within the time-lapse and 4) spatiotemporal features are extracted from the cell tracks and analyzed.

Here we demonstrate the step-by-step application of our pipeline as we follow individual cells throughout segmentation of the developing zebrafish embryo. The segmentation clock is a multi-cellular patterning system that translates the rhythm of cellular genetic oscillations into the successive and periodic formation of blocks of tissue in the trunk and tail called somites. Clock activity produces tissue-level waves of gene expression in presomitic mesoderm (PSM) that travel anteriorward until arrest at the position of the newly forming somite (Aulehla et al., 2008; Delaune et al., 2012; Masamizu et al., 2006; Palmeirim et al., 1997; Soroldoni et al., 2014). Historically, rapid cellular-level clock oscillations and ongoing tissue morphogenesis have made it difficult to describe the full picture of cellular dynamics underlying the clock pattern in zebrafish and other model systems (Delaune et al., 2012; Morelli et al., 2009; Shih et al., 2015; Yoshioka-Kobayashi et al., 2020). In creating the cell tracking pipeline our motivation was thus two-fold, first to directly answer questions about cellular clock dynamics, and second, to standardized a pipeline that makes this level of analysis accessible to a broader range of researchers and model systems.
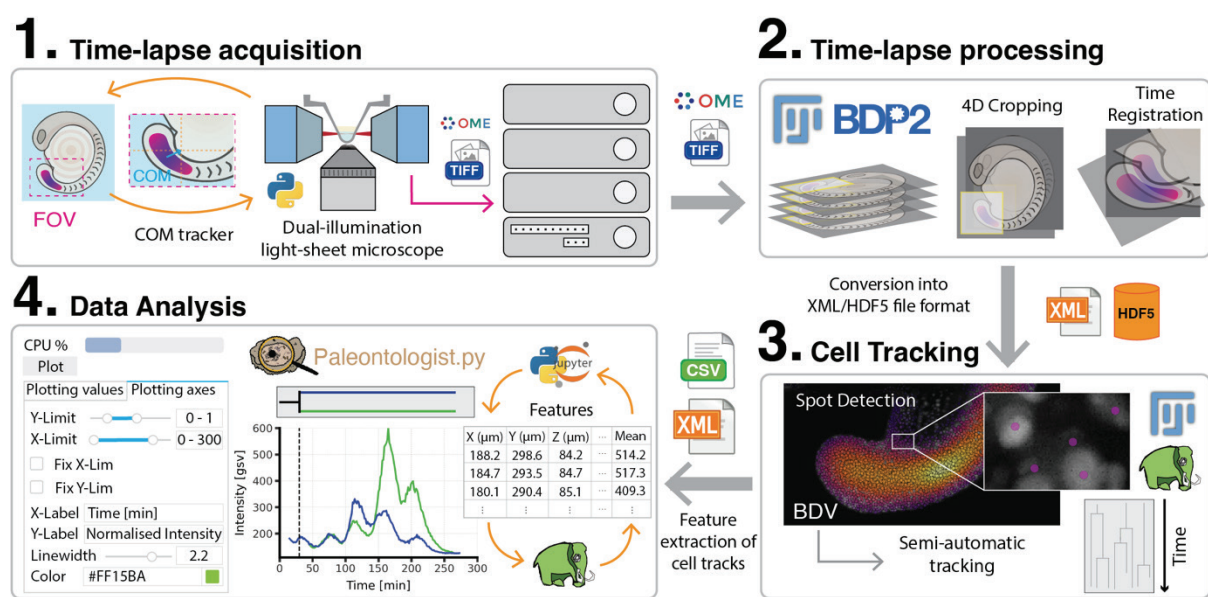

Figure 1. Cell tracking pipeline overview. 1) Cellular resolution time-lapse acquisition using, for example, light-sheet microscopy. To keep the region of interest inside the field of view (FOV), Python-based Centre Of Mass (COM) tracking is implemented. Resulting OME-TIFF data is saved into

a centralized workstation. **2)** The 5D time-lapse data cropping, drift correction and time-registration to facilitate later cell tracking. Processed time-lapses are saved in XML-HDF5 file format to allow interaction between the visualization and analysis tools. **3)** Tracking is done using Mastodon, a Fiji plugin. Mastodon outputs all the features from the cell tracks (XYZ cell coordinates, intensities, velocities, etc.) as an XML or CSV file. **4)** Data analysis of the features is made easy in Paleontologist, a modular python package that was built in our lab to interactively analyze tracked cells and output publication quality figures. Features from Mastodon can be iteratively plotted and edited in Paleontologist, then re-checked in Mastodon for cell visualization in the context of the embryo.

1. Acquisition: Cell-tracking in our system relies on a fluorescent nuclear marker, however the pipeline could also be adapted to track intra- or inter-cellular spot-like structures, for example tracking centrioles (Erpf et al., 2020). Feasibility is in large part determined by the quality of the acquired data; thus, it is an important first step to consider sample-dependent limitations including constraint-free mounting of the live sample, photo-bleaching, photo-toxicity, and spatiotemporal resolution relative to the dynamics of interest. Each experimental system will present unique limitations that require troubleshooting.

Depending on the sample size and microscopy hardware, the field of view (FOV) required to image at cellular resolution may fail to cover the entire region of interest (ROI). Particularly challenging is that the ROI itself may simply move out of the FOV due to growth and morphogenesis, a limitation we faced in the extending tail of the zebrafish. Happily, FOV problems can be resolved using short scripts of code to communicate with the microscope software controlling the camera and stage movement. For example, to enable long-term imaging of the segmentation clock, we designed a center of mass tracker that keeps the fluorescent clock signal inside the FOV as the embryo extends its tail. Our tracking script included here can easily be translated into other microscope systems that allow custom scripts. As microscopy has evolved, so has the level of automation enabled by these scripts which allow adaptive imaging (Roger et al., 2016). Von Wangenheim et al., 2017 developed

custom software – TipTracker – to automatically track diverse moving objects on various microscope setups.
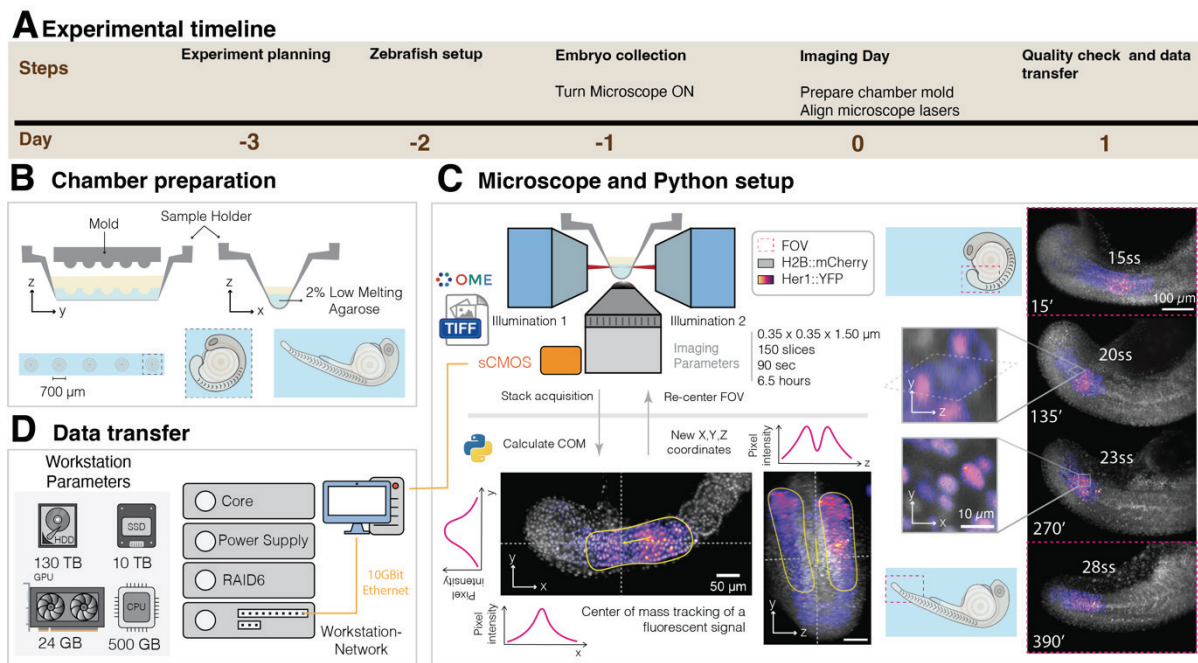
Figure 2. Time-lapse acquisition of zebrafish embryonic segmentation. A) Timeline to acquire a time-lapse of a zebrafish embryo. **B)** Preparation of the imaging chamber and mounting embryo. A 3D-printed sample holder is glued to a transparent filament sheet, creating a trough. Low-melting point agarose is added to the trough, then a 3D printed mold is used to create depressions into which the yolk of the embryo sits. **C)** We use a dual-illumination light-sheet microscope to acquire 5D time-lapse movies (voxel size: 0.35 µm in X-Y and 1.5 µm in Z, 150 slices, 90 seconds time-step and at least 6.5 h of imaging). Data is saved as an OME-TIFF file. During acquisition, the center of mass (COM) of the signal of interest (Magenta), is tracked to instruct the microscope to re-center the field of view (FOV) in XYZ. **D)** Acquired data is transferred from the imaging computer to an image processing station equipped with 24 GB of GPU, 500 GB of RAM, 10 TB of SSD and 130 TB of HD storage.

2. Processing: Following the acquisition of a TB-sized time-lapse movie, even the initial visualization can be problematic without the correct tools (software and hardware) due to

the limitations of a standard computer's RAM. To guide users over this hurdle, we detail pre-processing steps that convert the time-lapse into a manageable, ready-to-be tracked format. We cover cropping to reduce size in all dimensions XYZT, conversion to HDF5 files, and time registration to reduce sample movement and drift. Our pipeline consolidates and smooths the workflow through pre-processing steps that have been published as stand-alone operations (cropping, registration, chromatic aberration corrections), custom built for a specific project (tracking of all the cells in a developing mouse embryo, McDole et al., 2018) or available as a commercial product (Imaris (Bitplane), Arivis). The tools we recommend for pre-processing are mainly open-source (although we propose the equivalent commercial solutions), tested in multiple systems, and include a user-friendly interface (Fiji as open source and Imaris (Bitplane), Arivis as commercial). To facilitate the transfer and storage of the TB-sized datasets, we recommend data compression systems (Lempel-Ziv-Welch (LZW), Deflate compression as open source and Jetraw (Dotphoton) as commercial).

Figure 3. Pre-processing the Time-lapse. A) Timeline of pre- processing using the specified memory parameters from Figure 2B. **B)** Cropping and channel shift correction using

BigDataProcessor2. After loading the OME-TIFF files, the user interface allows a choice of transformations to apply (affine transformed viewing, cropping, binning, bit-depth conversion, drift correction and channel alignment). **C)** The transformed and cropped data is saved into XML-HDF5 file format, while the OME-TIFF raw data is stored in HDD as backup. The XML-HDF5 is saved in the SSD to speed future read-write processes. HDF5 data is organized in a pyramidal structure that enables interactivity wh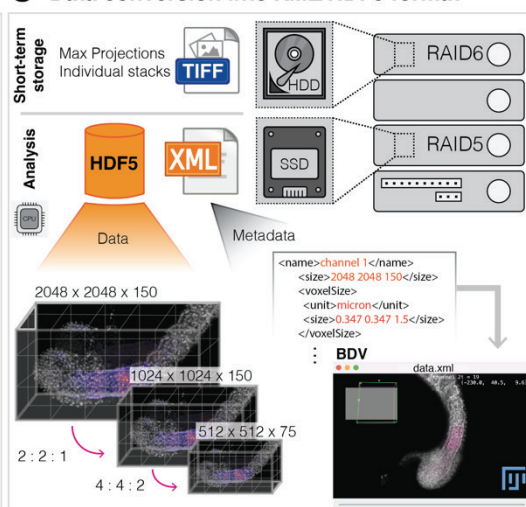en opened in BigDataViewer. **D)** To correct for embryo movement or drift, time registration is applied using the nuclei as registration markers. This step can be performed in CPU or GPU, with the resulting registration matrices for each timepoint stored in the companion XML file.

3. Cell Tracking: Pre-processing results in files that are easily opened and viewed in the cell-tracking tool Mastodon – a large-scale tracking and track-editing framework for large, multi-view images (https://github.com/mastodon-sc/mastodon). Although automation of the cell tracking within Mastodon is limited by time-lapse quality, we will cover how tracking parameters can be tuned for particular spot size, signal intensity, cell density, movement, etc. Manual tracking and editing are also user-friendly. Features including mean intensity, XYZ coordinates, number of links, and velocities can be extracted from the tracks and saved in CSV (comma separated values) files for later analysis.

4. Data Analysis: To explore features extracted from the cell tracks we created Paleontologist (https://github.com/bercowskya/paleontologist), a novel open-source analytical tool that requires no coding experience, but allows custom scripting. Paleontologist has been designed to interactively aid in quantitative and qualitative analysis of spatiotemporal features for single or multiple cell tracks of interest. The user can move back and forth between Paleontologist and Mastodon to investigate, correct and refine cells or groups of cells of interest. After using the data exploration interface, users can output their results as publication-quality figures.

We were motivated to develop Paleontologist due to the limited tools available to analyze spatiotemporal dynamics, especially those from individual cell tracks. Louveaux and Rochette developed an R package mamut2r (https://marionlouveaux.github.io/mamut2r/), which imports and visualizes xml files from MaMuT, a Fiji Plugin precursor to Mastodon (Carsten et al., 2018). However, besides custom-built scripts for specific purposes, no open-source tool exists to perform similar tasks for Mastodon. Mastodon outputs large CSV files that include the necessary information to reconstruct cell tracks, however the reconstruction process can be a challenge in the presence of cell division. Paleontologist solves these issues and returns arrays of tracks already reconstructed and including an ID for cell division to keep track of daughter cells. Moreover, spatiotemporal analysis can be complicated due to the large amount of data and the need to consider data pre-processing. For example, if registration was performed, then coordinates provided by Mastodon must also be registered. Paleontologist allows you to undo the registration if needed.

Materials

1. Zebrafish

Transgenic (Tg) fish were maintained according to standard procedures in École Polytechnique Fédérale de Lausanne (EPFL, Lausanne, CH). Embryos were produced by natural pairwise spawning. We used double Tg embryos heterozygous for a real-time segmentation clock reporter *Tg(her1:her1-yfp)* (Soroldoni et al., 2014) and the nuclear marker *Tg(Xla.Eef1a1:H2BmCherry)* (Recher et al., 2013). Embryos were incubated at 28.5°C in facility water until shield stage, then incubated at 19.5°C until the 8 to 10 somite stage when they were returned to 28.5°C until imaging at the 15-somite stage. Embryos for experiments

were dechorionated manually prior to imaging, then immersed in facility water with 0.02%

Tricaine (Sigma) for the rest of the experiment to avoid muscle twitching.

2. Microscope

We used a LightSheet Microscope LS1 (Viventis Microscopy Sárl, Switzerland) with the following configuration: Andor Zyla 4.2 sCOMS camera; 515 nm laser to image YFP; 561 nm laser to image mCherry; CFI75 Apochromat 25X, NA 1.1 detection objective (Nikon); scanned gaussian beam light sheet with thickness (FWHM) of 2.2 µm.

3. Imaging

3.1 Mounting

Whole embryos were mounted in an imaging chamber that reliably holds them in a lateral orientation, ideal for illuminating the segmenting trunk and tail. To make our molds, we first glue a thin membrane to the bottom of a 3D-printed chamber to make a trough (Viventis Microscopy Sárl, Switzerland). 2% LMP Agarose (Sigma, in E3 medium) is then added in stages to the trough along with a 3D-printed counter mold of 5 to 10 small protruding semi-circles (750 µm in diameter) such that depressions are created to hold the embryo's yolk while allowing unhindered extension of the tail and body (Herrgen L., Schröter C., Bajard L., Oates A.C., 2009) (Figure 2B). Embryos were added to the chamber after removing the mold and filling the trough with facility water plus 0.02% tricaine (Sigma). Our region of interest, the trunk and tail, lay flat in a lateral view along the thin agarose surface (Figure 2B)**.** Temperature was kept at 28.5°C using a recirculating air heating system (Cube 2, Life Imaging Services, Switzerland).

3.2 Imaging parameters

To track cells, we relied on a non-oscillating nuclear marker *Tg(Xla.Eef1a1:H2BmCherry)* (Recher et al., 2013). Cells in the segmenting region of the zebrafish embryo have a nucleus of 7-10 μm, requiring z-planes every 1.5 μm to produce spatial resolution suitable for tracking. We took stacks of 150 z-planes to span the depth of one entire side (right or left) of the bilaterally segmenting tissue at 15 somite stage and older. Younger embryos require more z-planes to compensate for greater depth of the segmenting tissue. To follow individual cells
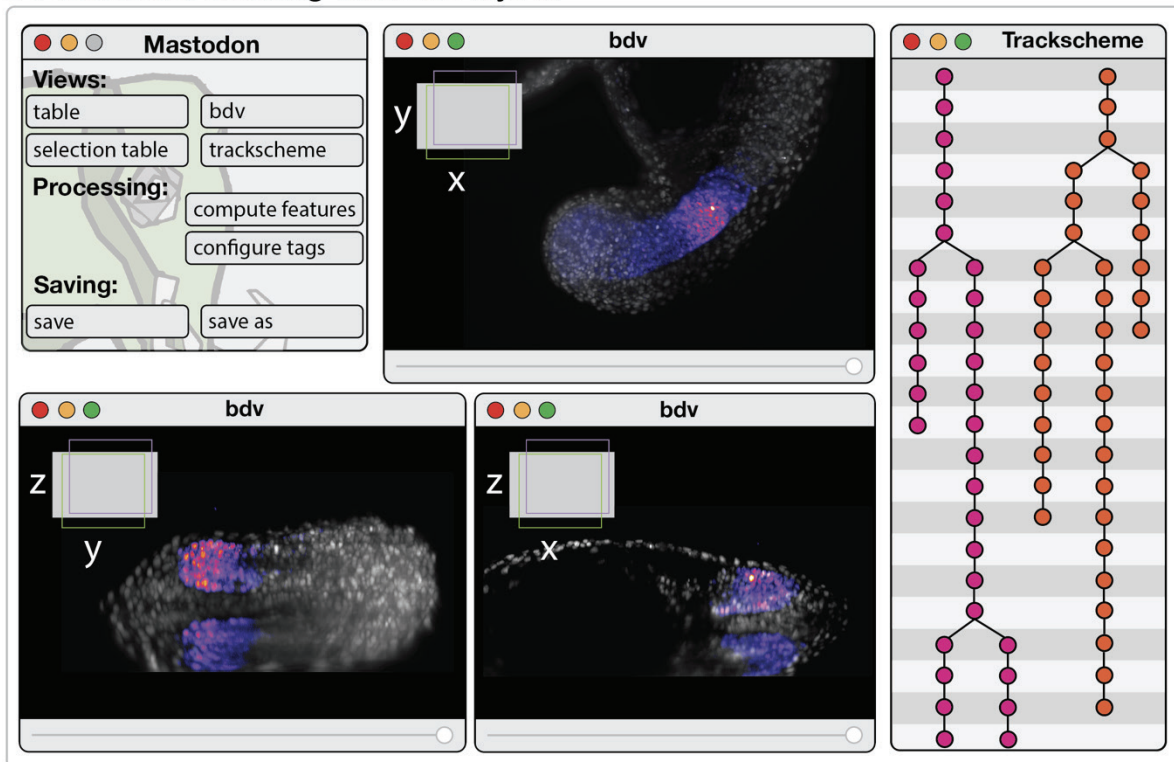
Figure 4. Cell tracking with Mastodon and analysis of tracks with Paleontologist. A) Layout we recommend for 3D tracking using Mastodon. Three BigDataViewer (BDV) windows are opened, each displaying a different view of the sample (XY, XZ and YZ). These views are also locked (using the lock symbol at the top left of the BDV window) so they all move synchronously through time while tracking. The track-scheme is also opened in one side and it is also locked so that the tracks can be easily and jointly inspected with the BDV windows. The Mastodon menu is also useful to have in hand since it is used to adjust tracking parameters, tags and sub-tags, to save, etc. **B)** Once tracking is done, we compute features (using the compute features button from Mastodon Menu, see A) and we obtain the comma-separated (csv) file with all the information needed for analysis. Paleontologist can then read this file and the XML file obtained when converting to HDF5 and use them to perform spatiotemporal analysis and cell track inspection with a user interface.

semi-automatically, we needed to acquire images every 90-120 seconds due to cell move-ment and mixing in the segmenting tissue.

Our time-lapse movies run for at least 6 hours (240 time points), with 90 sec intervals, a bit depth of 16, X-Y dimensions of 2048x2048 pixels, two channels, and 150 planes. A movie with these parameters has the following raw size:

Time Lapse movie size = [240 x 16 x 2048 x 2048 x 2 x 150] bits x 1 byte/8 bites = 6 x 10^{11} bytes = 600 GB

3.3 Center of mass tracking

To keep the segmenting tissue in the FOV, we automatically track the center of mass (COM) of the Her1-YFP signal while acquiring the time-lapse (Figure 2C). COM detection was per-formed using a python environment that directly communicates updated coordinates to the microscope control system. To find the COM in our channel of interest, YFP, we use a cropped region (Figure S1A) of a single timepoint that has been XYZ max-projected in the YFP channel (Figure S1B). These projections are processed using a median filter and a gaussian blur to smooth the signal, resulting in a filtered max projection that we binarized using an Otsu thresholding method (Figure S1C). COM is then calculated using this binary mask, and an offset value is produced corresponding to the XYZ distance that the FOV needs to shift when re-centering (Figure S1D). To prevent abrupt shifts, we set the move-ment to be maximum of 5µm per interval (Figure S1E). The following additional parameters can be adjusted: filter size applied (Gaussian and Median); use of the entire field of view or a cropped section (in XYZ); start of tracking while imaging; and COM as a binary mask, in which the center of pixels is used, or an intensity mask, in which the brightest area acts as the COM.

3.4 Data compression

The resulting four-dimensional (XYZT) for each channel is saved as an OME-TIFF (Leigh et al., 2017; Besson et al., 2019) (Figure 2C), a standardized format that is read by most open-source and commercial software. To make data easier to handle, during moving, processing and storage, we recommend compressing data during acquisition so that the output is a compressed ome.tiff file, which is easily read in Fiji. LZW (Lempel–Ziv–Welch) is an open-source universal lossless data compression algorithm that is easy to implement. In the case of our time-lapse movies, we obtain a reduction factor of 1:4, and can compress the data during acquisition if the imaging parameters permit this in terms of speed. If the compression speed is too low to run during acquisition or a better reduction factor is desired, a commercial solution, Jetraw (Dotphoton SA) allows for a 1:8 compression ratio at acquisition speed.

3.5 Quality Check

To avoid saving poor quality time-lapse data, e.g., a movie in which the sample degrades, we perform a quality check in parallel to acquisition by saving a maximum-intensity projection for each timepoint as a tiff file (Figure S2) (see Table 1). The max projections are viewed throughout acquisition (using Fiji) without the memory and speed problems that would otherwise be caused if trying to view the whole stack.

3.6 Time registration

In order to stabilize the time-lapse images in time to improve the cell tracking, we registered the 3D volumes from all timepoints using the first timepoint as the frame of reference. Parameters can be tuned according to the sample and imaging parameters. We show the steps and the parameters we use in Figure S3 which can be used as a starting point.

4. Computing Hardware

Image processing and data handling was done using a HIVE (Acquifer Imaging), a powerful centralized workstation for big-data storage and high performance computing. Our HIVE is equipped with a 24 GB Graphics Processing Unit (GPU), 500 GB of Random-access memory (RAM), 10 TB Solid-state drive (SSD) (RAID5) and 130 TB Hard Drive Disk (HDD) (RAID6). Data is stored in SSD while processing, then moved to the HDD for short-term storage. The microscope computer where the data is saved during acquisition is connected through a 10 Gbit cable to the HIVE to allow rapid transfer.

5. Software

Our main software platform was Fiji (Schindelin et al., 2012), which can be installed in Windows, Max OSX and Linux operating systems. Users requiring more than 2GB of RAM in Fiji should run on a 64-bit operating system due to limitations in Java memory management on 32-bit systems (Arganda-Carreras and Philippe, 2017). The core functionality of Fiji can be extended using plugins specified in the protocol. Fiji and its plugins used here can be found along with installation instructions at the imagej.net website.

Paleontologist runs on Python 3.6 or above and installation instructions are on the GitHub webpage (https://github.com/bercowskya/paleontologist). Install Anaconda Distribution (Anaconda Inc, 2020) to include interactivity and the user interface.

Procedure

Sample preparation and Image Acquisition

1. REQUIRED: Image your sample on a light-sheet or confocal microscope with resolution parameters that enable cell tracking (our parameters are shown in Figure 2C). Cell tracking works best in time-lapses acquired at high temporal and spatial resolution relative to cell movement/mixing. The rule of thumb we use is that if you cannot follow the cell by eye, the automatic tracking will not be able to track it either. TROUBLESHOOTING: Explore the range of spatiotemporal resolution in which tracking is feasible by acquiring short time-lapses using various parameters, then view as described in step 2 to see if you can visually follow individual nuclei. Balance this acquisition rate against potential photo-toxicity and the projected file size over the time interval of interest.

2. OPTIONAL: Use a COM tracker (or other method than enables automated detection of the ROI) to keep your ROI in the FOV (Figure 2C, S1).

3. OPTIONAL: We highly recommend data compression during or after acquisition (LZW, Jetraw).

Quality check of time-lapses and data transfer

4. REQUIRED: Download the free, open-source image processing software Fiji (https://imagej.net/software/fiji/#downloads)(Schindelin 2012). Note that there are commercial and other open-source solutions for big image data inspection including Imaris (Oxford Instruments), Arivis Vision 4D (Arivis AG), Vaa3D (Bria, et al., 2015)

and TDat (Li, et al., 2017). However, since we use Fiji for our pipeline, we will mainly describe the processing and tracking plugins using this software.

5. REQUIRED: Generate a maximum-intensity projection of the time-lapse (Table 1) using your image processing software of choice, then check the following to assess time-lapse quality:

    a. Visually check for photo-bleaching of the signal over time. A severe intensity decay could obscure the dynamics of interest, as well as interrupt cell tracking (Figure S2A).

    TROUBLESHOOTING: Either alter the imaging parameters when possible (reduce exposure time, laser intensity, the frame rate) or correct using a tool like for example: Correction for photo-bleaching from Miura, 2021.

    b. Using the re-slice tool from Fiji (Table 1), check whether the z-resolution is high enough so that the cells look like spot-like structures (Figure S2B). If the resolution is too low, the cells will appear almost like lines and the spot detection during cell tracking will not work.

    TROUBLESHOOTING: Alter imaging parameters by reducing the pixel size in the z-axis.

6. REQUIRED: Transfer the checked time-lapse to an image processing station. The specifications vary according to the size of the data and the desired waiting time between the processes. Because all of the tools we propose here can handle big data, the amount of RAM or the availability of a GPU will only improve the speed of the processing and the interactivity during the cell tracking. BigDataViewer (BDV)

adapts the size of the cache to the available memory (Pietzsch et al., 2015) and BigDataProcessor2 uses lazy loading and processing (Tischer, et al., 2021).

Data conversion

7. OPTIONAL: Crop the time-lapse in XYZT to reduce file size (Figure 3B) using Big-DataProcessor2 (BDP2, Tischer, et al., 2021), a Fiji plugin for processing n-dimensional big data images. Install by activating the *BigDataProcessor* Fiji update, then access using the graphical user interface or a Fiji macro. The time-lapse OME-TIFF is loaded and displayed using BigDataViewer (BDV, Pietzsch et al., 2015), which allows efficient lazy loading of raw data such that all processing steps are applied and then re-saved only once. When cropping, confirm that the sample remains inside the bounding cropping box by checking the initial, an intermediate and the last timepoint.

8. OPTIONAL: Detect chromatic shifts by looking for small XYZ shifts in normally overlapping signals (e.g., a nuclear marker and nuclear localized signal). Correction for shifts can be applied uniformly throughout the time-lapse in BDP2.

9. REQUIRED: Convert the time-lapse to HDF5 format (The HDF Group, 1997-2019) using BigDataViewer (Pietzsch, Tobias, et al., 2015). The HDF5 is associated with an XML file containing the metadata and all future registrations, etc. applied to the data. The XML-HDF5 should be stored in an SSD for fast reading and writing operations. When the conversion starts, the HDF5 and the XML are automatically created at the same time. All subsequent steps use HDF5/XML files.

TROUBLESHOOTING: The XML file and the HDF5 need to be in the same folder since the XML file has the path of the HDF5 which was used when it was created. Therefore, if the XML or the HDF5 are separated in different folders, a reading error will appear when trying to open the data.

Time registration

10. REQUIRED: During extended time-lapse imaging, the sample might drift due to growth or technical issues. This can make the cell tracking harder or sometimes not possible. To compensate for this drift, the nuclei are used as markers to register individual time-points to each other. We select a timepoint, usually the first, then use it as a reference. To perform time registration, we propose Fiji Plugins Multiview-Reconstruction (Preibisch et al., 2010) or BigStitcher (Hörl et al., 2019) as both are compatible with the XML-HDF5 file format. An alternative to Fiji would be Elastix (Klein et al., 2009; Shamonin et al., 2014), a toolbox for intensity-based medical image registration. If the imaging setup allows it, for instance when performing multi-view imaging, beads can be added and then used as registration markers (Preibisch et al., 2010).

TROUBLESHOOTING: The registrations are not actually applied to the data, but rather the matrices applied are saved for each timepoint in the XML (Figure 3D). This is useful since backup XML files (saved as ~.xml) are created in the process so that in case the registration fails, you can go back to the unregistered XML file and try various parameters without having to re-convert the data into XML-HDF5. However, this should be taken into account because the cell tracking coordinates will be outputted in the registered space.

a. Detect nuclei using the feature "Detect interest points". We recommend using the detection method "Difference of Gaussian (DoG)". Two parameters need to be defined for detection of interest points, an intensity threshold and a radius. These parameters can be tested on a single timepoint before running the detection for the whole time-lapse. If the nuclear signal varies over time (for example in the case of photobleaching), we recommend tuning the detection parameters using a timepoint where the signal is weak.

b. Perform a first round of registration using the method "Fast description based" (rotation invariant) registration in which timepoints are registered individually. Moreover, all the views are compared to each other and the first time-point is fixed so that the rest of the time-points can map-back to it using the translational invariant model. The transformation model we advice is a rigid affine one. Figure S3A shows the parameters we apply to our segmentation clock time-lapses, which can be used as a starting point to tune parameters for other systems.

c. Perform a second round of registration using the method. "Fast description based" translational invariant. In this case, because all timepoints are registered, we need to perform group-wise optimization by reasonable global optimization to "all-to-all" time-points with range. As before, the first view is fixed and the rest map-backed using a translational model. The parameters we used (Figure S3B) will require fine tuning for each independent dataset, but it is a good start.

d. Using the Fiji plugin "Multiview reconstruction", duplicate the transformation obtained using BigStitcher for the "nuclear marker" channel to the other channels. Multiview Reconstruction > Batch processing > Tools > Duplicate transformations.

e. Apply transformation of "One channel to other channels".

TROUBLESHOOTING: Registration usually fails due to the poor alignment of the registration markers (nuclei or beads) over time. This can be corrected by improving the temporal resolution. Bright objects in the FOV that are not within the sample, for example lint or debris, can also disrupt registration.

TROUBLESHOOTING: Automatic registration can sometimes fail because of the sample 'jumping' or rotating significantly in a few timepoints during the acquisition (the embryo might fall on the side and adopt a new equilibrium position). The resulting discontinuities may prevent automatic tracking. It is possible to correct big discontinuities manually with a set of tools from the BigDataViewer-Playground library (https://imagej.net/plugins/bdv/playground-manual-registration).

Spot detection and cell tracking

11. REQUIRED: The dataset is now ready for cell tracking using the Fiji plugin "Mastodon". Set up three BDV windows with orthogonal views. Synchronize the windows by locking each of them on view 1 by clicking on the first lock (Figure 4A). Select the channel corresponding to the nuclear marker, which will be used for tracking.

12. Set up the TrackScheme window and synchronize it with the BDV windows by locking each of them on view 1 by clicking on the first lock.

13. Familiarize yourself with the actions and their corresponding keyboard shortcuts. They can be found, and modified, in Mastodon > File > Preferences > Keymap.

14. Set up semi-automatic tracking (Mastodon > Plugins > Tracking > Configure semi-automatic tracker…) with the following parameters (information about the parameters is displayed by placing the cursor over a given parameter):

    a. Setup ID: Select the channel corresponding to the nuclear marker. This is the channel that will be used for tracking.

    b. Quality factor: This parameter depends on the dataset and needs to be empirically determined. A value of 0.5 is a reasonable starting point.

    c. Distance factor: This parameter depends on the dataset, especially on how much cells move between time frames, and needs to be empirically determined. A value of 1.5 is a reasonable starting point.

    d. N time-points: This parameter specifies how many time-points can be processed at most. It does not affect the quality of tracking itself and can therefore be set at a large number (e.g., 40).

    e. Tracking direction selection: Forward and back tracking in time can be performed.

    f. Untick "Allow linking to an existing spot" if performing semi-automatic tracking since if you already curated a track, it will stop the new track to start following previously tracked cells.

    g. Tick "Run detection if existing spot cannot be found"

15. Place the cursor on one cell of interest and hit "A" to add a new Spot.

16. Adjust the size of the Spot to make it fit the nucleus by making the Spot smaller ("Q") or bigger ("E").

17. Click on the cell of interest, place the cursor inside the Spot added in step 14 and start semi-automatic tracking (Mastodon > Plugins > Tracking > Semi-automatic tracking or Ctrl + T).

    TROUBLESHOOTING: If semi-automatic tracking fails, adjust tracking parameters. If it still does not work, try a different timelapse with improved registration and adjusted imaging settings.

18. Curate the track by visually inspection. Check that the cell of interest is followed through the entire track. Portions of a track can be deleted onwards from the timeframe where an error is made. OPTIONAL: tag the track with a label.

19. Save the Mastodon project regularly to avoid losing tracking data in case of software crash ("Save" button in the Mastodon window or Mastodon > File > Save project)

20. Repeat steps 17 to 19 until the cell of interest has been tracked for the desired duration.

21. Repeat steps 15 to 20 for each cell that needs to be tracked.

22. Compute the features of interest ("compute features" button in the Mastodon window).

23. Generate a results table ("table" button in the Mastodon window).

24. Export the table as a CSV file (Table window > File > Export to CSV).

25. To use Paleontologist, you need to load the CSV and the XML files. To see the details on how to use the documentation visit https://github.com/bercowskya/paleontologist.

Fiji Plugin Name	Usage	URL for Wiki	Procedure steps
Z-Functions	Max Intensity Projection	https://im-agej.net/imag-ing/z-functions	Image > Stacks > Z-Project Projection type: Max Intensity
Z-Functions	R-Slice	https://im-agej.net/imag-ing/z-functions	Image > Stacks > Reslice
BigDataViewer	Convert into XML-HDF5	https://im-agej.net/plugins/bdv/	1. Open time-lapse (as a virtual stack) 2. Export current image as XML/HDF5
BigStitcher	Time registra-tion	https://im-agej.net/plugins/bigstitcher/	See Figure S3 for steps
Multiview Recon-struction	Duplicate Transfor-mations to other channels	https://im-agej.net/plugins/multiview-recon-struction	

Mastodon	Cell tracking	https://github.com/mastodon-sc/mastodon	

Table 1. Fiji Plugins name, usage, link to wiki and procedure steps.

References

Amat, Fernando, et al. "Fast, accurate reconstruction of cell lineages from large-scale fluorescence microscopy data." *Nature methods* 11.9 (2014): 951-958.

Anaconda Software Distribution. "Anaconda Documentation." (2020).

Arganda-Carreras, Ignacio, and Philippe Andrey. "Designing image analysis pipelines in light microscopy: a rational approach." *Light Microscopy*. Humana Press, New York, NY, 2017. 185-207.

Attardi, Andrea, et al. "Neuromesodermal progenitors are a conserved source of spinal cord with divergent growth dynamics." *Development* 145.21 (2018): dev166728.

Besson, Sébastien, et al. "Bringing open data to whole slide imaging." *European Congress on Digital Pathology*. Springer, Cham, 2019.

Bria, Alessandro, Giulio Iannello, and Hanchuan Peng. "An open-source VAA3D plugin for real-time 3D visualization of terabyte-sized volumetric images." *2015 IEEE 12th International Symposium on Biomedical Imaging (ISBI)*. IEEE, 2015.

de Medeiros, Gustavo, et al. "Multiscale light-sheet organoid imaging framework." bioRxiv (2021).

Delaune, Emilie A., et al. "Single-cell-resolution imaging of the impact of Notch signaling and mitosis on segmentation clock dynamics." *Developmental cell* 23.5 (2012): 995-1005.

Erpf, Anna C., and Tamara Mikeladze-Dvali. "Tracking of centriole inheritance in C. elegans." *microPublication Biology*2020 (2020).

Garcia, Monica D., et al. "Live imaging of mouse embryos." *Cold Spring Harbor Protocols* 2011.4 (2011): pdb-top104.

Guo, Long, Shiro Ikegawa, and Chisa Shukunami. "Emergence of Zebrafish as a Model System for Understanding Human Scoliosis." *Zebrafish, Medaka, and Other Small Fishes*. Springer, Singapore, 2018. 217-234.

He, Zhisong, et al. "Lineage recording reveals dynamics of cerebral organoid regionalization." bioRxiv (2020).

Hirsinger, Estelle, and Ben Steventon. "A versatile mounting method for long term imaging of zebrafish development." *JoVE (Journal of Visualized Experiments)* 119 (2017): e55210.

Hörl, David, et al. "BigStitcher: reconstructing high-resolution image datasets of cleared and expanded samples." *Nature Methods* 16.9 (2019): 870-874.

Klein, Stefan, et al. "Elastix: a toolbox for intensity-based medical image registration." *IEEE transactions on medical imaging* 29.1 (2009): 196-205.
Kleinhans, David Simon, and Virginie Lecaudey. "Standardized mounting method of (zebrafish) embryos using a 3D-printed stamp for high-content, semi-automated confocal imaging." *BMC biotechnology* 19.1 (2019): 1-10.

Kluyver, Thomas, et al. *Jupyter Notebooks-a publishing format for reproducible computational workflows*. Vol. 2016. 2016.

Leigh, Roger, et al. "OME Files-An open source reference library for the OME-XML metadata model and the OME-TIFF file format." *BioRxiv* (2017): 088740.

Li, Yuxin, et al. "TDat: an efficient platform for processing petabyte-scale whole-brain volumetric images." *Frontiers in neural circuits* 11 (2017): 51.

Maroto, Miguel, Robert A. Bone, and J. Kim Dale. "Somitogenesis." *Development* 139.14 (2012): 2453-2456.

McConnell, Gail, et al. "A novel optical microscope for imaging large embryos and tissue volumes with sub-cellular resolution throughout." *Elife* 5 (2016): e18659.

McDole, Katie, et al. "In toto imaging and reconstruction of post-implantation mouse development at the single-cell level." *Cell* 175.3 (2018): 859-876.

Miura, Kota. "Bleach correction ImageJ plugin for compensating the photobleaching of time-lapse sequences." *F1000Research* 9 (2020).

Morelli, Luis G., et al. "Delayed coupling theory of vertebrate segmentation." *HFSP journal* 3.1 (2009): 55-66.

Oates, Andrew C., Luis G. Morelli, and Saúl Ares. "Patterning embryos with oscillations: structure, function and dynamics of the vertebrate segmentation clock." *Development* 139.4 (2012): 625-639.

Pietzsch, Tobias, et al. "BigDataViewer: visualization and processing for large image data sets." *Nature methods* 12.6 (2015): 481-483.
Preibisch, Stephan, et al. "Efficient Bayesian-based multiview deconvolution." *Nature methods* 11.6 (2014): 645-648.

Preibisch, Stephan, et al. "Software for bead-based registration of selective plane illumination microscopy data." *Nature methods* 7.6 (2010): 418-419.

Recher, Gaëlle, et al. "Zebrafish midbrain slow-amplifying progenitors exhibit high levels of transcripts for nucleotide and ribosome biogenesis." *Development* 140.24 (2013): 4860-4869.

Rohde, Laurel A., et al. "Cell-autonomous generation of the wave pattern within the vertebrate segmentation clock." *bioRxiv* (2021).

Royer, Loïc A., et al. "Adaptive light-sheet microscopy for long-term, high-resolution imaging in living organisms." *Nature biotechnology* 34.12 (2016): 1267-1278.

Sage, Daniel, et al. "DeconvolutionLab2: An open-source software for deconvolution microscopy." *Methods* 115 (2017): 28-41.

Sawada, Atsushi, et al. "Fgf/MAPK signalling is a crucial positional cue in somite boundary formation." (2001): 4873-4880.

Schindelin, Johannes, et al. "Fiji: an open-source platform for biological-image analysis." *Nature methods* 9.7 (2012): 676-682.

Schmidt, Uwe, et al. "Cell detection with star-convex polygons." *International Conference on Medical Image Computing and Computer-Assisted Intervention*. Springer, Cham, 2018.

Shah, Gopi, et al. "Multi-scale imaging and analysis identify pan-embryo cell dynamics of germlayer formation in zebrafish." *Nature communications* 10.1 (2019): 1-12.

Shamonin, Denis P., et al. "Fast parallel image registration on CPU and GPU for diagnostic classification of Alzheimer's disease." *Frontiers in neuroinformatics* 7 (2014): 50.

Shih, Nathan P., et al. "Dynamics of the slowing segmentation clock reveal alternating two-segment periodicity." *Development*142.10 (2015): 1785-1793.

Soroldoni, Daniele, et al. "A Doppler effect in embryonic pattern formation." *Science* 345.6193 (2014): 222-225.

Tinevez, Jean-Yves, et al. "TrackMate: An open and extensible platform for single-particle tracking." *Methods* 115 (2017): 80-90.

Tischer, Christian, et al. "BigDataProcessor2: A free and open-source Fiji plugin for inspection and processing of TB sized image data." *Bioinformatics* 37.18 (2021): 3079-3081.

Von Wangenheim, Daniel, et al. "Live tracking of moving samples in confocal microscopy for vertically grown roots." *Elife* 6 (2017): e26792.

Weigert, Martin, et al. "Star-convex polyhedra for 3d object detection and segmentation in microscopy." *Proceedings of the IEEE/CVF Winter Conference on Applications of Computer Vision*. 2020.

Wen, Chentao, et al. "3DeeCellTracker, a deep learning-based pipeline for segmenting and tracking cells in 3D time lapse images." *Elife* 10 (2021): e59187.

Wolff, Carsten, et al. "Multi-view light-sheet imaging and tracking with the MaMuT software reveals the cell lineage of a direct developing arthropod limb." *Elife* 7 (2018): e34410.

Yoshioka-Kobayashi, Kumiko, et al. "Coupling delay controls synchronized oscillation in the segmentation clock." *Nature* 580.7801 (2020): 119-123.

Chapter 5   Discussion

In my thesis, I investigated how cells are instructed to become part of somite boundaries by the zebrafish segmentation clock. This work relied heavily on imaging zebrafish embryos with lightsheet microscopy. My colleagues and I developed a pipeline for data acquisition and image processing with the primary aim of following the dynamics of the segmentation clock in individual cells during somitogenesis (Chapter 4). Thanks to its modularity and versatility, this pipeline can be adapted to image zebrafish embryos at various stages and also other organisms and organoids or other similar-sized samples. As I already discussed the results of Chapters 2 and 3, here I briefly summarize our main discoveries and provide ideas for future work.

We imaged, for the first time, the onset of the zebrafish segmentation clock in live embryos using the Her1-YFP, Mesp-ba-mKate2 and Tbx6-mNG transgenes. We observed that the 4th Her1-YFP wave prefigures the anterior boundary of the first somite. We did not observe any feature of the Her1-YFP signal prior to this stage that would predict which part of the mesoderm was about to become the first somite. speculate on the function of oscillations and waves prior to the fist somite.

To our surprise, we found that Tbx6-mNG oscillates in individual cells, and travels at the tissue level as waves of gene expression in the PSM during early somitogenesis. Tbx6 oscillations have not been previously reported in any species. By aligning the Her1-YFP and the Tbx6-mNG signals from different embryos using a temporal reference point, we showed that the signals oscillate in-phase. Tbx6 oscillations were abolished in most PSM cells in *her1$^{-/-}$;her7$^{-/-}$* embryos, which suggests that the Her1/Her7 loop is a key driver of Tbx6 oscillations, and consequently also of the waves of Tbx6 expression travelling in the PSM during early somitogenesis. We observed that the first and second travelling waves of Tbx6-mNG arrested at a position that prefigured the anterior boundaries of somite 1 and 2, respectively. Together, these results show how the Clock (Her1) and the Wavefront (Tbx6) interact to prefigure the position of the two anterior-most boundaries.

This work raised many questions about the onset of the segmentation clock, the interaction between Tbx6 and the Her1/Her7 loop, and the functional significance of Tbx6 waves during early somitogenesis. Future work is required to establish what genes drive the expression of *her1* during the onset of the segmentation clock and how is the wave pattern initially established. The molecular interactions between Tbx6 and the Her1/Her7 loop need to be further investigated. Tbx6 has been shown to bind to the *her1* promoter (Brend and Holley, 2009). The cell population located anteriorly to the first boundary did not express Tbx6-mNG but displayed several oscillations of Her1-YFP expression. This cell population can therefore be used to study the dynamics of Her1 oscillations in the absence of Tbx6. Another important question is whether Her1 and/or Her7 directly regulate the expression of *tbx6.* One possibility is that the Her1/Her7 loop could indirectly drive Tbx6 oscillations by interacting with *ripply1/2* or *groucho,* which are known to convert Tbx6 from transcriptional

activator to repressor (Kawamura et al., 2008, 2005) and to post-transcriptionally regulate Tbx6 (Wanglar et al., 2014). However, this seems unlikely since the expression pattern of *ripply1* and *her1* do not spatially overlap in the PSM at bud stage (Retnoaji et al., 2014).

We showed that the second and third waves of Tbx6 expression arrested at a location prefiguring the positions of the first and second somite boundaries. However, it is not yet clear whether the Tbx6 expression domain also exactly prefigures the position of other somite boundaries, and this question needs to be addressed in future work. Future experiments are also required to gain a deeper insight into the transition from the oscillatory dynamics of Tbx6 during early-somitogenesis to the supposedly non-oscillatory activity of Tbx6 during mid-somitogenesis. It is crucial to understand whether the spatial pre-pattern is established in the same manner over the course of somitogenesis or to what extent different mechanisms are involved in the formation of anterior versus posterior somite boundaries, as has been previously discussed (Holley, 2006).

Another approach to understand how cells are instructed to form a somite boundary by the segmentation clock is by perturbing the segmentation clock and looking at resulting defective somite boundaries. We desynchronized and resynchronized the segmentation clock by transiently blocking Notch signaling in zebrafish embryos. We noticed that some qualitative features of segment defects, such as the location and the shape of the defect, were already visible in somite boundaries. Although this was generally expected from the overlapping statistical distribution of somite and myotome boundaries previously reported (van Eeden et al., 1996), a direct mapping of a given somite defect and the corresponding permanent myotome segment boundary in the same embryo had not been achieved in any species.

Further, we were able to relate the integrity of sub-regions of a somite boundary to the local synchrony of the segmentation clock in the cells contributing to the boundary regions. We observed that the phase coherence of oscillating cells was spatially heterogeneous: it was higher in cells forming the correct part of a defective somite boundary than in cells forming the defective part of the boundary. We observed three kinds of phase patterns co-existing in the PSM during the resynchronization of the segmentation clock: normal waves travelling anteriorly in the PSM, phase vortices rotating along the A-P axis and disordered phase patterns. Cells where the phase pattern behaved as travelling waves tended to form the correct parts of defective boundaries while the phase pattern was generally either disordered or travelling as a vortex in cells forming the defective parts of boundaries.

As already mentioned, chapter 3 featured a preliminary investigation of the formation of defective boundaries during the resynchronization of the segmentation clock. Future work is needed, in particular to increase the number of samples. More specifically, back-tracking cells from additional normal boundaries located in the "intermingled region" will help to refine our understanding of what minimal level of synchrony is required for the correct formation of somite boundaries. Indeed, we propose that the quantitative level of synchrony can be used to predict whether a region of the PSM will form a normal boundary or not. Our data indicate that the minimum level lies between 0.45 and 0.6. Whether this level is developmental stage specific, and whether it maps to the case of slow desynchronization

remains to be tested. Future work is also required to make some results more quantitative. For example, a vorticity index can be computed to compare different phase vortices, and also to detect phase vortices with axes not aligned along the PSM. Somite boundary defects could also be quantified using the spatial arrangement of nuclei.

Most of the analysis that I developed to determine what level of synchrony is required for the correct formation of somite boundary during the resynchronization of the segmentation clock can also be applied to address the same question during the desynchronization of the segmentation clock. The desynchronization of the segmentation clock can be compared between several mutants of the Notch pathway such as *beamter (deltaC)*, *after eight (deltaD)* and *deadly seven* (*notcha1*), which are thought to desynchronize at different speeds, as suggested by the difference in their respective anterior limits of defect (van Eeden et al., 1996). Using the imaging protocol developed in Chapter 2, we can now follow the process of desynchronization, from the onset of the segmentation clock until the formation of defective somite boundaries.

Because the transgenes *Tg(mesp:mesp-ba-mkate2)* and Hoff (*Tg(her7:mkate2-nls;her1:her1-mneongreen)*)) share the same mKate2 fluorophore, we have not been able to image them simultaneously to link the Her1 dynamics with the spatial pre-pattern in individual cells during the resynchronization of the segmentation clock. This could be addressed by generating new transgenes with different fluorophores. We can also investigate the Tbx6 dynamics during both the desynchronization and the resynchronization of the segmentation clock. By integrating the dynamics of Her1 (core component of the Clock), Tbx6 (core component of the Wavefront) and Mesp-ba (component of the spatial pre-pattern), and using DAPT as a perturbation, we hope to better understand how the interaction between the Clock and the Wavefront establish the spatial pre-pattern during somitogenesis.

Chapter 6   Materials and methods

6.1   Fish care

Wildtype (Ab and TL), mutants (*her1$^{-/}$;her7$^{-/}$*) and transgenic zebrafish (*Tg(her1:her1-yfp)* (Soroldoni et al., 2014), *Tg(mesp-ba:mesp-ba-mkate2)* (Rohde et al., 2021), *Tg(her1:her1-mneongreen)* (Hoff) *Tg(Xla.Eef1a1:H2BmCherry)*(Recher et al., 2013), Tg(tbx6:tbx6-mneon-green) were maintained according to standard procedures. Embryos were produced by natural pairwise spawning and staged according to (Kimmel et al., 1995). Heterozygous transgenic embryos were used for experiments. Embryos were incubated at 28.5°C in E3 medium (5mM NaCl, 0.17mM KCl, 0.33mM CaCl2, 0.33mM MgSO4, pH adjusted to 7.3 with Tris-HCl pH 7.5 1M) . In some experiments, embryos were shifted to a 19.5°C incubator after shield stage. *Tg(her1-Venus;mesp-ba-mkate2)* and *Tg(tbx6-mneongreen;mesp-ba-mKate2)* embryos were injected at 1-cell stage with 0.1 ng of H2B-mCerulean mRNA.

6.2   DAPT treatments

Embryos in their chorions were incubated in 50μM DAPT (Sigma) or in 0.5% DMSO as control, in E3 medium from 4.5hpf to 9.5hpf. To prevent crystallization of DAPT, the E3 medium was pre-heated at 60°C before diluting the DAPT stock solution (50mM) and 0.4% DMSO was added to the mix to reach a final concentration of 0.5% DMSO.
 DAPT was washed out by 3 washes in 0.5% DMSO, for 5 minutes each, on an horizontal shaker and by 2 quick washes in E3 medium.

6.3   Imaging

6.3.1 Lighsheet imaging

The lightsheet setup and the mounting technique are detailed in Chapter 4 (Material). The mounting of embryos during epiboly is different and is described in section 2.2.1. Embryos imaged from epiboly (Chapter 2) were immersed in E3 medium while embryos imaged during somitogenesis (Chapter 3) were immersed in E3 with 0.02% tricaine (Sigma).

6.3.2 Widefield imaging

Hoff and WT embryos were imaged on a Zeiss Axio Observer 7 widefield microscope to measure their somitogenesis period. Embryos were mounted in 2% low-melting agarose (Sigma) and imaged every 5 minutes in E3 medium at 28.5°C using a Zeiss Fluar 10x/0.5NA objective and a Photometrics Prime95B back-illuminated sCMOS camera.

Single cells dissociated from multiple tailbuds and posterior PSM of Tbx6-mNeonGreen-positive embryos were imaged on a Zeiss Axio Observer 7 widefield microscope. After dissociation, single cells in suspension were added to an imaging chamber (Cellview cell culture dish 35/10mm, glass bottom) previously coated with protein A (Sigma). The culture medium was composed of Leibovitz's L-15 medium (Thermo Fisher), 50ng/μl protein A (Sigma) 0.01% methyl cellulose (Sigma). Single cells were imaged every 5 minutes with a

Zeiss Plan-Apochromat 40x/0.95 NA objective and a Photometrics Prime95B back-illuminated sCMOS camera using brightfield, 515nm and 555nm lasers.

6.3.3 Documentation of *in situ* hybridization staining

Embryos stained by *in situ* hybridization were photographed on a binocular microscope (Olympus SZ61) with a RGB camera (Olympus DP22).

6.4 Image processing and analysis

Every step of image processing was performed using Fiji (Schindelin et al., 2012). The basic processing steps (pre-processing, registration and cell tracking) of lightsheet timelapses are detailed in Chapter 4. The cell tracking Fiji plugin Mastodon returns a CSV file containing, among others, the positions of cells in 3D, a tagging system that we used to assign cells in different categories (e. g. « Somite 1 – Anterior ») and different measures of the signal intensity inside the ellipsoid for all channels. In our analysis, we always used the measure « Spot center intensity » to obtain the signals of interest.

6.4.1 Elliptic transform

To better visualize the dynamics of the segmentation clock during epiboly, timelapses were transformed using a method called elliptic transformation that that is similar to how the Earth is projected on a map. Using the Fiji plugin BigDataViewer-Playground (https://github.com/bigdataviewer/bigdataviewer-playground), an ellipsoid was fitted to the embryo and the dataset was transformed to be represented in spherical coordinates. Movie X shows the maximum-intensity projection of the transformed dataset. As for a Mercator projection, the poles are distorted but the equator is preserved. Therefore, the equator of the ellipsoid was set as an anteroposterior line located at an equidistance between the two sides of the PSM. During epiboly, this line is perpendicular to the margin, passing through the shield. During somitogenesis, the line aligns with the notochord. We then projected the transformed dataset using a maximum-intensity projection to generate kymographs.

6.4.2 Kymographs

Lines of interests (LOIs) were manually traced along the PSM in maximum-intensity projection of timelapses. Kymographs were obtained using the Fiji plugin "LOI interpolator" (Soroldoni et al., 2014). For timelapses of embryos during epiboly (Chapter 2), kymographs were obtained from maximum-intensity projections of elliptically transformed timelapses. LOIs were traces from the margin of the blastoderm to the animal pole.

6.4.3 Image processing of widefield timelapse of single cells

An elliptical selection was manually drawn around single cells in the brightfield channel to compute the mean Tbx6-mNeonGreen signal.

6.5 *In situ* hybridization and antibody staining

Chromogenic *in situ* hybridization staining for *xirp2a* (Deniziak et al., 2007) and *her1* (Müller, 1996) was performed according to (Narayanan and Oates, 2019). Combined whole-mount fluorescent *in situ* hybridization for *tbx6* (Nikaido et al., 2002) and antibody staining against Tbx6 was performed according to (He et al., 2020) with the following antibodies:
- Sheep anti-DIG POD (Roche, cat. no. 11207733910; RRID: AB_514500). Dilution 1 :1000
- Mouse IgG1 Anti-Tbx6 (home-made, clone A83). Dilution 1 :500
- Alexa-Fluor 488 goat anti-Mouse IgG1 (ThermoFisher A-21121). Dilution 1 :1000

6.6 Data analysis

6.6.1 Segment boundary defect scoring

Each side of embryos stained by *in situ* hybridization for *xirp2a* was visually assessed on a binocular microscope (Olympus SZ61). A segment boundary was scored as defective if the boundary did not span the full dorso-ventral axis, was significantly distorted or had a break (Riedel-Kruse et al., 2007). The anterior limit of defect (ALD) was determined as the number of the anterior-most defective segment boundaries on each side individually.

6.6.2 Somite boundary scoring

Somite boundaries were from lightsheet timelapses of DAPT-treated embryos using the nuclear marker (H2B-mCherry and mKate2-NLS). The somite boundary number n was scored at the time of formation of the somite boundary number $n+1$. In a normal boundary, the spatial arrangement of nuclei on both side of the boundary forms a characteristic cleft (Falk et al., 2022). A somite boundary was scored as defective if the cleft was interrupted. Somite boundaries that could not be confidently scored as normal or defective were judged « ambiguous ».

6.6.3 Computation of oscillators' phase with pyBoat

The phase of cellular oscillators was computed from Her1-mNG oscillatory traces by wavelet analysis with pyBOAT (Mönke et al., 2020) (https://github.com/tensionhead/pyBOAT). The signal was detrended using sinc detrending and normalized by its amplitude envelope. The following parameters were used:
- Cut-off period for sinc detrending: 70
- Window size for amplitude envelope calculation: 20
- Wavelet analysis :
  - Smallest period : 10
  - Highest period : 80
  - Number of periods : 400

6.6.4 Phase coherence

We calculated the global phase coherence of the different cell populations forming somite boundaries. For a given timepoint, the global phase coherence is given by:

$$r = \left| \frac{1}{N} \sum_{j=1}^{N} e^{i\theta_j} \right|$$

where r is the global phase coherence, N is the number of cells in the population and θ_j is the phase of the cellular oscillator *j* at that timepoint. We calculated the cellular phase coherence of a given cell using the same formulae with a cell population composed of this cell's 6 nearest neighbors.

6.6.5 Geometrical transformations

We obtained the view called "PSM transection" which virtually represents a transverse cut of the PSM, we projected cell positions along the A-P axis. The notochord in our timelapses was used to get a reference of the A-P axis. For each timelapse, we tracked two positions in the notochord. One position is anterior (yellow star, Fig. 32), and the other is posterior (magenta star, Fig. 32) to the position of cells back-tracked from somite boundaries. For each timepoint, the reference points on the notochord (yellow and magenta stars, upper left part of the 3D plot) were translated and rotated so that one of the reference point (yellow star) is placed at the origin (0, 0, 0) and the other reference point (magenta star) is aligned along the x-axis (lower right part of the 3D plot). The same transformation (translation and rotations) was applied to the positions of cells (Fig 32B). This transformation did not modify the relative position of cells, it only allowed to represent their positions in the D-V and M-L axes, making possible the visualization of defects in somite boundaries in two dimensions.

Mathematically, this geometrical transformation is the result of one translation and two rotations. The translation is performed by subtracting the position vectors of cells and notochord reference points by the vector position of one of the notochord reference point. To align both notochord reference points along the same axis (e. g. the x-axis), two rotations are required. In spherical coordinates (according to the ISO 80000-2:2019 convention), the vector joining the two notochord reference points is defined by the polar angle θ, the azimuthal angle φ and the radial distance *r.* Aligning this vector with the x-axis can be done by rotating the vector about the z-axis by the angle $-\theta$ and about the y-axis by the angle 90 - φ. These two rotations were applied by two rotation matrices with the position vectors of the notochord reference points and the position vectors of each cell. The rotation matrices are given by:

$$R_z(-\theta) = \begin{bmatrix} \cos -\theta & -\sin(-\theta) & 0 \\ \sin(-\theta) & \cos(-\theta) & 0 \\ 0 & 0 & 1 \end{bmatrix}$$

$$R_y(90 - \varphi) = \begin{bmatrix} \cos(90 - \varphi) & 0 & -\sin(90 - \varphi) \\ 0 & 1 & 0 \\ \sin(90 - \varphi) & 0 & \cos(90 - \varphi) \end{bmatrix}$$

References

Akiyama, R., Masuda, M., Tsuge, S., Bessho, Y., Matsui, T., 2014. An anterior limit of FGF/Erk signal activity marks the earliest future somite boundary in zebrafish. Development 141, 1104–1109. https://doi.org/10.1242/dev.098905

Bajard, L., Morelli, L.G., Ares, S., Pecreaux, J., Julicher, F., Oates, A.C., 2014. Wnt-regulated dynamics of positional information in zebrafish somitogenesis. Development 141, 1381–1391. https://doi.org/10.1242/dev.093435

Ban, H., Yokota, D., Otosaka, S., Kikuchi, M., Kinoshita, H., Fujino, Y., Yabe, T., Ovara, H., Izuka, A., Akama, K., Yamasu, K., Takada, S., Kawamura, A., 2019. Transcriptional autoregulation of zebrafish *tbx6* is required for somite segmentation. Development dev.177063. https://doi.org/10.1242/dev.177063

Brend, Holley, 2009. Expression of the oscillating gene *her1* is directly regulated by hairy/enhancer of split, T-box, and suppressor of hairless proteins in the zebrafish segmentation clock. Dev. Dyn. 238, 2745–2759. https://doi.org/10.1002/dvdy.22100

Bulman, M.P., Kusumi, K., Frayling, T.M., McKeown, C., Garrett, C., Lander, E.S., Krumlauf, R., Hattersley, A.T., Ellard, S., Turnpenny, P.D., 2000. Mutations in the human Delta homologue, DLL3, cause axial skeletal defects in spondylocostal dysostosis. Nat Genet 24, 438–441. https://doi.org/10.1038/74307

Dahmann, C., Oates, A.C., Brand, M., 2011. Boundary formation and maintenance in tissue development. Nat Rev Genet 12, 43–55. https://doi.org/10.1038/nrg2902

Delaune, E.A., François, P., Shih, N.P., Amacher, S.L., 2012. Single-Cell-Resolution Imaging of the Impact of Notch Signaling and Mitosis on Segmentation Clock Dynamics. Developmental Cell 23, 995–1005. https://doi.org/10.1016/j.devcel.2012.09.009

Deniziak, M., Thisse, C., Rederstorff, M., Hindelang, C., Thisse, B., Lescure, A., 2007. Loss of selenoprotein N function causes disruption of muscle architecture in the zebrafish embryo. Experimental Cell Research 313, 156–167. https://doi.org/10.1016/j.yexcr.2006.10.005

Duboule, 1994. Temporal colinearity and the phylotypic progression= a basis for the stability of avertebrate Bauplan and the evolution of morphologies through heterochrony.

Duboule, D., 2022. The (unusual) heuristic value of Hox gene clusters; a matter of time? Developmental Biology 484, 75–87. https://doi.org/10.1016/j.ydbio.2022.02.007

Dubrulle, J., McGrew, M.J., Pourquié, O., 2001. FGF Signaling Controls Somite Boundary Position and Regulates Segmentation Clock Control of Spatiotemporal Hox Gene Activation. Cell 106, 219–232. https://doi.org/10.1016/S0092-8674(01)00437-8

Falk, H.J., Tomita, T., Mönke, G., McDole, K., Aulehla, A., 2022. Imaging the onset of oscillatory signaling dynamics during mouse embryo gastrulation. Development 149, dev200083. https://doi.org/10.1242/dev.200083

Goodrich, 1913. Metameric Segmentation and Homology.

Goodwin, B.C., 1965. Oscillatory behavior in enzymatic control processes. Advances in Enzyme Regulation 3, 425–437. https://doi.org/10.1016/0065-2571(65)90067-1

He, J., Mo, D., Chen, J., Luo, L., 2020. Combined whole-mount fluorescence in situ hybridization and antibody staining in zebrafish embryos and larvae. Nat Protoc 15, 3361–3379. https://doi.org/10.1038/s41596-020-0376-7

Holley, S.A., 2006. Anterior–posterior differences in vertebrate segments: specification of trunk and tail somites in the zebrafish blastula. Genes Dev. 20, 1831–1837. https://doi.org/10.1101/gad.1453706

Horikawa, K., Ishimatsu, K., Yoshimoto, E., Kondo, S., Takeda, H., 2006. Noise-resistant and synchronized oscillation of the segmentation clock. Nature 441, 719–723. https://doi.org/10.1038/nature04861

Ishimatsu, K., Takamatsu, A., Takeda, H., 2010. Emergence of traveling waves in the zebrafish segmentation clock. Development 137, 1595–1599. https://doi.org/10.1242/dev.046888

Jiang, Y.-J., Aerne, B.L., Smithers, L., Haddon, C., Ish-Horowicz, D., Lewis, J., 2000. Notch signalling and the synchronization of the somite segmentation clock. Nature 408, 475. https://doi.org/10.1038/35044091

Jouve, C., Iimura, T., Pourquie, O., 2002. Onset of the segmentation clock in the chick embryo: evidence for oscillations in the somite precursors in the primitive streak. Development 1107–1117.

Kanki, J.P., Ho, R.K., 1997. The development of the posterior body in zebrafish 13.

Kawamura, A., Koshida, S., Hijikata, H., Ohbayashi, A., Kondoh, H., Takada, S., 2005. Groucho-Associated Transcriptional Repressor Ripply1 Is Required for Proper Transition from the Presomitic Mesoderm to Somites. Developmental Cell 9, 735–744. https://doi.org/10.1016/j.devcel.2005.09.021

Kawamura, A., Koshida, S., Takada, S., 2008. Activator-to-Repressor Conversion of T-Box Transcription Factors by the Ripply Family of Groucho/TLE-Associated Mediators. Molecular and Cellular Biology 28, 3236–3244. https://doi.org/10.1128/MCB.01754-07

Kimmel, C.B., Ballard, W.W., Kimmel, S.R., Ullmann, B., Schilling, T.F., 1995. Stages of embryonic development of the zebrafish. Developmental Dynamics 203, 253–310. https://doi.org/10.1002/aja.1002030302

Kuramoto, Y., Nishikawa, I., 1987. Statistical macrodynamics of large dynamical systems. Case of a phase transition in oscillator communities. Journal of Statistical Physics 49, 569–605. https://doi.org/10.1007/BF01009349

Lewis, J., 2003. Autoinhibition with transcriptional delay: a simple mechanism for the zebrafish somitogenesis oscillator. Current Biology 13, 1398–1408.

Mongera, A., Rowghanian, P., Gustafson, H.J., Shelton, E., Kealhofer, D.A., Carn, E.K., Serwane, F., Lucio, A.A., Giammona, J., Campàs, O., 2018. A fluid-to-solid jamming transition underlies vertebrate body axis elongation. Nature 561, 401–405. https://doi.org/10.1038/s41586-018-0479-2

Monk, N.A.M., 2003. Oscillatory Expression of Hes1, p53, and NF-⬛B Driven by Transcriptional Time Delays. Current Biology 5.

Mönke, G., Sorgenfrei, F.A., Schmal, C., Granada, A.E., 2020. Optimal time frequency analysis for biological data - pyBOAT (preprint). Systems Biology. https://doi.org/10.1101/2020.04.29.067744

Moreno, T.A., Jappelli, R., Belmonte, J.C.I., Kintner, C., 2008. Retinoic acid regulation of the Mesp–Ripply feedback loop during vertebrate segmental patterning. Developmental Biology 315, 317–330. https://doi.org/10.1016/j.ydbio.2007.12.038

Müller, M., 1996. Expression domains of a zebrafish homologue of the Drosophila pair-rule gene hairy correspond to primordia of alternating somites 8.

Nandagopal, N., Santat, L.A., Elowitz, M.B., 2019. Cis-activation in the Notch signaling pathway. eLife 8, e37880. https://doi.org/10.7554/eLife.37880

Narayanan, R., Oates, A., 2019. Detection of mRNA by Whole Mount in situ Hybridization and DNA Extraction for Genotyping of Zebrafish Embryos. BIO-PROTOCOL 9. https://doi.org/10.21769/BioProtoc.3193

Nikaido, M., Kawakami, A., Sawada, A., Furutani-Seiki, M., Takeda, H., Araki, K., 2002. *Tbx24*, encoding a T-box protein, is mutated in the zebrafish somite-segmentation

mutant *fused somites*. Nature Genetics 31, 195–199.
https://doi.org/10.1038/ng899

Oates, A.C., Ho, R.K., 2002. Her and Delta/Notch in zebrafish segmentation. Development 129, 2929–2946.

Oates, A.C., Rohde, L.A., Ho, R.K., 2005. Generation of segment polarity in the paraxial mesoderm of the zebrafish through a T-box-dependent inductive event. Developmental Biology 283, 204–214. https://doi.org/10.1016/j.ydbio.2005.04.012

Oginuma, M., Niwa, Y., Chapman, D.L., Saga, Y., 2008. Mesp2 and Tbx6 cooperatively create periodic patterns coupled with the clock machinery during mouse somitogenesis. Development 135, 2555–2562. https://doi.org/10.1242/dev.019877

Paroush, Z., 1994. Groucho is required for Drosophila neurogenesis, segmentation, and sex determination and interacts directly with hairy-related bHLH proteins. Cell 79, 805–815. https://doi.org/10.1016/0092-8674(94)90070-1

Petrungaro, G., Uriu, K., Morelli, L.G., 2017. Mobility-induced persistent chimera states. Physical Review E 96. https://doi.org/10.1103/PhysRevE.96.062210

Retnoaji, B., Akiyama, R., Matta, T., Bessho, Y., Matsui, T., 2014. Retinoic acid controls proper head-to-trunk linkage in zebrafish by regulating an anteroposterior somitogenetic rate difference. Development 141, 158–165. https://doi.org/10.1242/dev.097568

Riedel-Kruse, I.H., Muller, C., Oates, A.C., 2007. Synchrony Dynamics During Initiation, Failure, and Rescue of the Segmentation Clock. Science 317, 1911–1915. https://doi.org/10.1126/science.1142538

Rohde, L.A., Bercowsky-Rama, A., Negrete, J., Valentin, G., Naganathan, S.R., Desai, R.A., Strnad, P., Soroldoni, D., Jülicher, F., Oates, A.C., 2021. Cell-autonomous generation of the wave pattern within the vertebrate segmentation clock (preprint). Developmental Biology. https://doi.org/10.1101/2021.05.29.446196

Saga, Y., Hata, N., Koseki, H., Taketo, M.M., 1997. Mesp2: a novel mouse gene expressed in the presegmented mesoderm and essential for segmentation initiation. Genes Dev. 11, 1827–1839. https://doi.org/10.1101/gad.11.14.1827

Sari, D.W.K., Akiyama, R., Naoki, H., Ishijima, H., Bessho, Y., Matsui, T., 2018. Time-lapse observation of stepwise regression of Erk activity in zebrafish presomitic mesoderm. Sci Rep 8, 4335. https://doi.org/10.1038/s41598-018-22619-9

Sawada, A., 2001. Fgf signalling has a crucial role in zebrafish segmentation 8.

Sawada, A., Fritz, A., Jiang, Y., Yamamoto, A., Yamasu, K., Kuroiwa, A., Saga, Y., Takeda, H., 2000. Zebrafish Mesp family genes, mesp-a and mesp-b are segmentally expressed in the presomitic mesoderm, and Mesp-b confers the anterior identity to the developing somites. Development 127, 1691–1702. https://doi.org/10.1242/dev.127.8.1691

Schindelin, J., Arganda-Carreras, I., Frise, E., Kaynig, V., Longair, M., Pietzsch, T., Preibisch, S., Rueden, C., Saalfeld, S., Schmid, B., Tinevez, J.-Y., White, D.J., Hartenstein, V., Eliceiri, K., Tomancak, P., Cardona, A., 2012. Fiji: an open-source platform for biological-image analysis. FOCUS ON BIOIMAGE INFORMATICS 7.

Sieger, D., Tautz, D., Gajewski, M., 2003. The role of Suppressor of Hairless in Notch mediated signalling during zebrafish somitogenesis. Mechanisms of Development 120, 1083–1094. https://doi.org/10.1016/S0925-4773(03)00154-0

Sonnen, K.F., Lauschke, V.M., Uraji, J., Falk, H.J., Petersen, Y., Funk, M.C., Beaupeux, M., François, P., Merten, C.A., Aulehla, A., 2018. Modulation of Phase Shift between Wnt and Notch Signaling Oscillations Controls Mesoderm Segmentation. Cell 172, 1079-1090.e12. https://doi.org/10.1016/j.cell.2018.01.026

Soroldoni, D., Jorg, D.J., Morelli, L.G., Richmond, D.L., Schindelin, J., Julicher, F., Oates, A.C., 2014. A Doppler effect in embryonic pattern formation. Science 345, 222–225. https://doi.org/10.1126/science.1253089

Sparrow, D.B., Chapman, G., Wouters, M.A., Whittock, N.V., Ellard, S., Fatkin, D., Turnpenny, P.D., Kusumi, K., Sillence, D., Dunwoodie, S.L., 2006. Mutation of the LUNATIC FRINGE Gene in Humans Causes Spondylocostal Dysostosis with a Severe Vertebral Phenotype. The American Journal of Human Genetics 78, 28–37. https://doi.org/10.1086/498879

Sparrow, D.B., Guillen-Navarro, E., Fatkin, D., Dunwoodie, S.L., 2008. Mutation of HAIRY-AND-ENHANCER-OF-SPLIT-7 in humans causes spondylocostal dysostosis. Human Molecular Genetics 17, 3761–3766. https://doi.org/10.1093/hmg/ddn272

Sparrow, D.B., Sillence, D., Wouters, M.A., Turnpenny, P.D., Dunwoodie, S.L., 2010. Two novel missense mutations in HAIRY-AND-ENHANCER-OF-SPLIT-7 in a family with spondylocostal dysostosis. Eur J Hum Genet 18, 674–679. https://doi.org/10.1038/ejhg.2009.241

Steventon, B., Duarte, F., Lagadec, R., Mazan, S., Nicolas, J.-F., Hirsinger, E., 2016. Species-specific contribution of volumetric growth and tissue convergence to posterior body elongation in vertebrates. Development 143, 1732–1741. https://doi.org/10.1242/dev.126375

Strogatz, S.H., 2000. From Kuramoto to Crawford: exploring the onset of synchronization in populations of coupled oscillators. Physica D: Nonlinear Phenomena 143, 1–20. https://doi.org/10.1016/S0167-2789(00)00094-4

Takahashi, J., Ohbayashi, A., Oginuma, M., Saito, D., Mochizuki, A., Saga, Y., Takada, S., 2010. Analysis of Ripply1/2-deficient mouse embryos reveals a mechanism underlying the rostro-caudal patterning within a somite. Developmental Biology 342, 134–145. https://doi.org/10.1016/j.ydbio.2010.03.015

Takahashi, Y., Koizumi, K., Takagi, A., Kitajima, S., Inoue, T., Koseki, H., Saga, Y., 2000. Mesp2 initiates somite segmentation through the Notch signalling pathway. Nat Genet 25, 390–396. https://doi.org/10.1038/78062

Takke, C., Campos-Ortega, J.A., 1999. her1, a zebrafish pair-rule like gene, acts downstream of notch signalling to control somite development. Development 126, 3005–3014.

Thomson, L., Muresan, L., Steventon, B., 2021. The zebrafish presomitic mesoderm elongates through compression-extension (preprint). Developmental Biology. https://doi.org/10.1101/2021.03.11.434927

Tsiairis, C.D., Aulehla, A., 2016a. Self-Organization of Embryonic Genetic Oscillators into Spatiotemporal Wave Patterns. Cell 164, 656–667. https://doi.org/10.1016/j.cell.2016.01.028

Tsiairis, C.D., Aulehla, A., 2016b. Self-Organization of Embryonic Genetic Oscillators into Spatiotemporal Wave Patterns. Cell 164, 656–667. https://doi.org/10.1016/j.cell.2016.01.028

Uriu, K., Liao, B.-K., Oates, A.C., Morelli, L.G., 2021. From local resynchronization to global pattern recovery in the zebrafish segmentation clock. eLife 10, e61358. https://doi.org/10.7554/eLife.61358

Uriu, K., Morishita, Y., Iwasa, Y., 2009. Traveling wave formation in vertebrate segmentation. Journal of Theoretical Biology 257, 385–396. https://doi.org/10.1016/j.jtbi.2009.01.003

van Eeden, F.J.M., Fredericus J. M., Ursula Schach, Michael Brand, Makoto Furutani-Seiki, Pascal Haffter, Matthias Hammerschmidt, Carl-Philipp Heisenberg, Yun-Jin Jiang, Donald A. Kane, Robert N. Kelsh, Mary C. Mullins, Jörg Odenthal, Rachel M.

Warga, Miguel L. Allende, Eric S. Weinberg, Christiane Nüsslein-Volhard, 1996. Mutations affecting somite formation and patterning in the zebrafish, Danio rerio. Development 123, 153–164.

Venzin, O.F., Oates, A.C., 2020. What are you synching about? Emerging complexity of Notch signaling in the segmentation clock. Developmental Biology 460, 40–54. https://doi.org/10.1016/j.ydbio.2019.06.024

Vermot, J., Pourquié, O., 2005. Retinoic acid coordinates somitogenesis and left–right patterning in vertebrate embryos. Nature 435, 215–220. https://doi.org/10.1038/nature03488

Wanglar, C., Takahashi, J., Yabe, T., Takada, S., 2014. Tbx Protein Level Critical for Clock-Mediated Somite Positioning Is Regulated through Interaction between Tbx and Ripply. PLoS ONE 9, e107928. https://doi.org/10.1371/journal.pone.0107928

Webb, A.B., Lengyel, I.M., Jörg, D.J., Valentin, G., Jülicher, F., Morelli, L.G., Oates, A.C., 2016. Persistence, period and precision of autonomous cellular oscillators from the zebrafish segmentation clock. eLife Sciences 5, e08438. https://doi.org/10.7554/eLife.08438

Windner, S.E., Doris, R.A., Ferguson, C.M., Nelson, A.C., Valentin, G., Tan, H., Oates, A.C., Wardle, F.C., Devoto, S.H., 2015. Tbx6, Mesp-b and Ripply1 regulate the onset of skeletal myogenesis in zebrafish. Development 142, 1159–1168. https://doi.org/10.1242/dev.113431

Wülbeck, C., Campos-Ortega, J.A., 1997. Two zebrafish homologues of the Drosophila neurogenic gene groucho and their pattern of transcription during early embryogenesis. Development Genes and Evolution 207, 156–166. https://doi.org/10.1007/s004270050103

Yabe, T., Hoshijima, K., Yamamoto, T., Takada, S., 2016. *Mesp* quadruple zebrafish mutant reveals different roles of *mesp* genes in somite segmentation between mouse and zebrafish. Development dev.133173. https://doi.org/10.1242/dev.133173

Yabe, T., Takada, S., 2016. Molecular mechanism for cyclic generation of somites: Lessons from mice and zebrafish. Develop. Growth Differ. 58, 31–42. https://doi.org/10.1111/dgd.12249

Yasuhiko, Y., Haraguchi, S., Kitajima, S., Takahashi, Y., Kanno, J., Saga, Y., 2006. Tbx6-mediated Notch signaling controls somite-specific *Mesp2* expression. Proc. Natl. Acad. Sci. U.S.A. 103, 3651–3656. https://doi.org/10.1073/pnas.0508238103

Curriculum Vitae

CONTACT INFORMATION

OLIVIER VENZIN
AVENUE DE MORGES 70
1004 LAUSANNE
0041 79 579 94 59
OLIVIER.VENZIN@YAHOO.COM

EMPLOYMENT HISTORY

PHD STUDENT IN THE OATES LAB AT EPFL - 15.11.2017 – PRESENT
INTERN AT VOLUMINA MEDICAL, LAUSANNE - JUNE 2017 – OCTOBER 2017
INTERN AT LUNAPHORE TECHNOLOGIES SA, LAUSANNE – JULY 2015 – AUGUST 2015

EDUCATION

MASTER OF SCIENCE MSC IN BIOENGINEERING, EPFL, LAUSANNE – 2014 – 2016
BACHELOR IN LIFE SCIENCE – EPFL, LAUSANNE – 2011 – 2014
HIGH SCHOOL DIPLOMA – LYCÉE CANTONAL DE PORRENTRUY – 2007 – 2010

PROFESSIONAL QUALIFICATIONS

CODING: PYTHON

AWARDS

STILL WAITING

PUBLICATIONS

OLIVIER F. VENZIN, ANDREW C. OATES,
WHAT ARE YOU SYNCHING ABOUT? EMERGING COMPLEXITY OF NOTCH SIGNALING IN THE SEGMENTA-
TION CLOCK,
DEVELOPMENTAL BIOLOGY,
VOLUME 460, ISSUE 1,
2020,
PAGES 40-54,
ISSN 0012-1606,
HTTPS://DOI.ORG/10.1016/J.YDBIO.2019.06.024.
(HTTPS://WWW.SCIENCEDIRECT.COM/SCIENCE/ARTICLE/PII/S0012160618304445)

INTERESTS

HIKING, SKIING, DIVING